UC Irvine
UC Irvine Electronic Theses and Dissertations

Title

Ultra-Sensitive Carbon Interdigitated Electrode Arrays for Redox Amplification

Permalink

https://escholarship.org/uc/item/9184v50d

Author

Kamath, Rahul

Publication Date

2015

Peer reviewed|Thesis/dissertation

UNIVERSITY OF CALIFORNIA,

IRVINE

Ultra-Sensitive Carbon Interdigitated Electrode Arrays for Redox Amplification

DISSERTATION

Submitted in partial satisfaction of the requirements

for the degree of

DOCTOR OF PHILOSOPHY

in Biomedical Engineering

by

Rahul R. Kamath

Dissertation Committee:

Professor Marc J. Madou, Chair

Professor Jered Haun

Professor James Brody

2015

This thesis is dedicated to my beautiful wife Trishna whose unwavering belief, love and support kept me

motivated and my parents for encouraging me to push my limits.

Table of Contents

List of Figures

List of Tables

Acknowledgments

I would like to thank Prof. Marc Madou for his guidance in setting up my thesis and providing technical suggestions throughout the course of my PhD research. He has been instrumental in streamlining my thought process and provided valuable feedback during writing of research articles. He also encouraged me to work outside my comfort zone which has helped me grow as a research scientist.

I am also thankful to Dr. Horacio Kido for his help on immunoassay development as well as providing equipment support. I would also like to thank Dr. Lawrence Kulinsky for providing valuable inputs throughout my doctoral work. I also want to acknowledge Dr. Gobind Bisht and Sunshine Holmberg for training me to run electrochemical experiments and data analysis during first year in the lab as a graduate student.

I would like to thank my Dr. Andrea Mardegan and Dr. Swati Sharma with whom I collaborated and published several papers. I am also thankful to all members, past and present, who have attend group meetings to provide crucial feedback. I also acknowledge Jacob Moebius, Alexandra Perebikovsky, Alex Beed and Priyanka Jain for providing technical support. Special thanks to Dr. Jered Haun for attending and evaluating my student seminar presentation as well as all the help provided during my Teaching Assistant stint.

Last but not the least; I am grateful to my funding sources, namely UC Irvine BME Fellowship, Teaching Assistantship and Schick, Energizer that enabled me to focus on my research.

Curriculum Vitae

EDUCATION

PhD, Biomedical Engineering   University of California, Irvine   01/ 2015

MS, Biomedical Engineering   University of Florida, Gainesville   05/ 2010

BE, Biomedical Engineering   University of Mumbai, Mumbai   06/ 2008

EXPERIENCE

Graduate Researcher, BioMEMS Laboratory, UCI   09/2011- Present

V&V Engineer, Cardiac Science Corporation   10/2010-09/2011

Graduate Researcher, BioMEMS and Microfluidics Laboratory, UF   12/2008-10/2010

Research Intern, AIIPMR, Mumbai   01/2008-05/2008

PUBLICATIONS

- Selective Redox Signal Enhancement of Catecholamines using Carbon Interdigitated Electrode Arrays (in prep)

- Ultrasensitive Electrochemical Immunosensor based on HRP-OPD Redox System using C-MEMS Electrodes, **Biosensors and Bioelectronics** 2015 (Submitted)

- Pyrolyzed Photoresist Carbon Electrodes in an Aprotic Solvent: Bilirubin Electrochemistry and Interaction with Electrogenerated Superoxides, **Electrochimica Acta** 2014

- Speciation of Trace Chromium with Bismuth Modified Pyrolyzed Photoresist Carbon Electrodes, **Electroanalysis** 2014

- Selective Detection of Dopamine against Ascorbic Acid Interference using 3D Carbon Interdigitated Electrode Arrays, **ECS Transactions** 2014

- Three-Dimensional Carbon Interdigitated Electrode Arrays for Redox-Amplification, **Analytical Chemistry** 2014

- Porous Glassy Carbon Formed by Rapid Pyrolysis of Phenol-Formaldehyde Resins and its Performance as Electrode Material for Electrochemical Double Layer Capacitors, **Journal of Analytical and Applied Pyrolysis** 2014

- Optimization of Carbon Electrodes Derived from Epoxy-based **Photoresist Journal of Electrochemical Society** 2013

- Aptamer-enabled Efficient Isolation of Cancer Cells from Whole Blood Using a Microfluidic Device, **Analytical Chemistry**, 2012

CONFERENCES

- Merging Electrical and Centripetal Forces With An Enzyme Cascade On a Compact Disc for the Ultimate in Analytical Performance in Molecular Diagnostics" **2013 Annual Meeting of American Electrophoresis Engineers**

- Aptamer-facilitated High-efficiency Cancer Cell Sorting in a Micropost-based Microfluidic Device, **The 15th International Conference on Miniaturized Systems for Chemistry and Life Sciences**, 2011

Abstract of the Dissertation

Ultra-Sensitive Carbon Micro-Electrode Arrays for Redox Amplification

by

Rahul R. Kamath

Doctor of Philosophy in Biomedical Engineering

University of California, Irvine, 2015

Professor Marc J. Madou, Chair

Miniaturization of electrodes has played a key role in the advancement of electrochemical measurements. Ultramicroelectrodes (UME) have a critical dimension that is of the same order as the diffusion layer thickness at the electrode, thus reducing the time scale of an electrochemical measurement. In the case of macroelectrodes, the electroactive species diffuses linearly normal to the electrode surface; whereas in UMEs diffusion is radial thereby increasing the current density. This phenomenon makes UMEs extremely advantageous for the following reasons: 1) the steady state is reached much faster, 2) electrochemical kinetic measurements are possible and 3) highly accurate measurements can be done even in nonpolar solvents or in resistive solutions. One such arrangement is that of interdigitated electrode arrays (IDEAs). In IDEAs two working electrodes are held in close proximity such that their diffusion profiles overlap. When specific potential are applied to the two working electrodes the electroactive redox species will cycle (oxidize and reduce) multiple times before diffusing out into the bulk solution of the sample. This redox cycling effect has been exploited in last couple of decades for enhancing current signal and lowering the limit of detection. However, most of the work

involves use of noble metal IDEAs, which are expensive, require sophisticated instrumentation, and are difficult to fabricate. In this contribution, we report on simpler fabrication technique that involves patterning of SU-8, a negative photoresist, using conventional UV photolithography followed by pyrolysis in an inert environment to create conductive carbon IDEAs with sub-micron resolution. The sensor performance was electrochemically characterized under different geometries under stationary and flow conditions. The capability of the carbon IDEA sensor was demonstrated by applying them in selective detection of dopamine against ascorbic acid interference, selective amplification of neurotransmitters such as dopamine and epinephrine in their mixture, and finally as an electrochemical immunoassay.

1. Electrochemical Sensors

1.1 Introduction to Electrochemical Sensors

A chemical sensor gives continuous data about its surrounding conditions. The word continuous is important, especially during the latter part of the thesis where I will be talking about Assays which provides information in steps. Essentially, a chemical sensor provides quantitative information about a chemical species of interest. Accordingly, the chemical sensor group is classified as: electrical (or electrochemical), optical, mass or thermal depending on the medium of the output. Out of these, electrochemical sensors are the most dominant and oldest class constituting nearly 55% of all the chemical sensors commercially available in the market.[1] Some of the advantages of electrochemical sensors over the other types of chemical sensors are: better dynamic range, operability in turbid solutions, operability in highly resistive environments,[2] lower cost due to less sophisticated instrumentation, improved response times due to miniaturization, works better for smaller analytes due to faster diffusion, [3] and the fact that the convection can be incorporated to enhance signal in amperometric sensors (explained in Electrochemical Characterization Chapter).

Electrochemical sensors are applicable for analytes in solid, liquid or gaseous phase. The latter two are more common in terms of availability and usage whereas the sensors with solid analytes offer an important advantage that it can put up with high temperature environment. Electrochemical sensors are broadly classified as: potentiometric, conductometric and amperometric. In potentiometric sensor, a potential difference obtained at equilibrium (when no current is flowing) between working and reference

electrodes provides quantitative information about the chemical species of interest whereas in conductometric sensor, the conductance of the sample is measured either by applying DC or AC excitation signal. The last but not the least is an amperometric sensor that measures faradaic current at the working electrode on application of suitable potential between working and reference electrode. This current is in direct proportion to the concentration of the target analyte. This thesis will focus only on amperometric sensors out of the three categories as described above.

1.2 Amperometric Sensors

As explained in the previous section, in amperometric sensors the potential is applied between working and a reference electrode in a two electrode setup. A more usual setup i.e., a three electrode setup in Fig. 1 involves a counter electrode as the third electrode. The potential applied can be either a step in which case the measurements are chronoamperometric or the potential can be varied from one fixed value to another in which case the measurements are voltammetric. In any case, a working electrode, in a physical electrochemistry experiment, more often than not is made up of an inert material which will allow current to pass through without being affected. Examples of commonly used materials for the working electrode are gold, platinum or carbon.
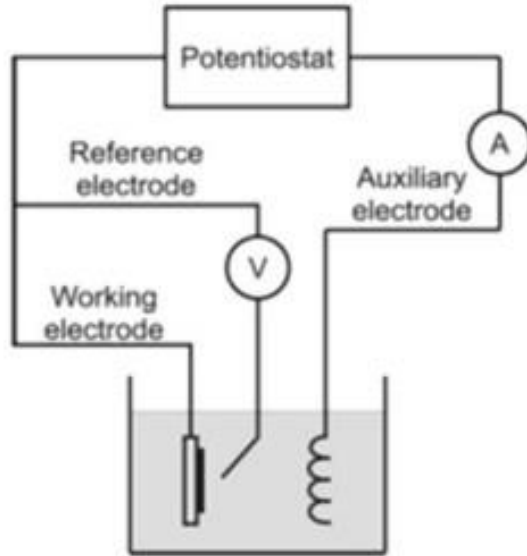
Figure 1: Illustration of the experimental setup in a three electrode system. Courtesy: http://people.ccmr.cornell.edu/

The potential of the working electrode is referenced against a stable electrode whose potential shouldn't, ideally, vary during the course of an electrochemical experiment. This stability can only be attained if little to no current is passed through during the experiment. In reality, any conductive material may be used as a reference electrode. However, any such measurement needs to be well calibrated before being reported in a data. Hence, researchers generally use one of the following: Saturated Calomel, Silver/Silver Chloride, Copper/Copper Sulfate, Normal Hydrogen Electrode etc. as standard references.

Counter electrodes, as the name suggests, are electrodes where reactions counter to the ones happening at the working electrode occur. If a reduction happens at the working electrode, oxidation will take place at the counter and vice-versa. In essence, counter

electrodes acts as a source/sink of electrons to complete the electrical circuit. This function allows the reference electrode to maintain a stable potential during an experiment. Hence, its electrochemical area is generally kept higher than working electrode so as to not limit the speed of reactions at the working electrode. Counter electrode is usually made up of one of the inert materials as mentioned above.

1.3 Amperometric Microelectrodes

Miniaturization of electrodes has greatly extended electrochemistry applications. A typical electrode or macroelectrode will have radius in the range of several millimeters. On the other hand microelectrodes are typically smaller than 25μm.[4] By definition, microelectrodes have characteristic surface dimension smaller than the thickness of the diffusion layer during the time scale of an electrochemical experiment.
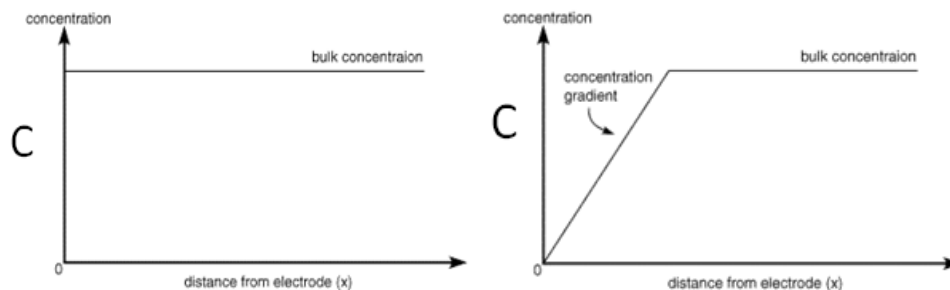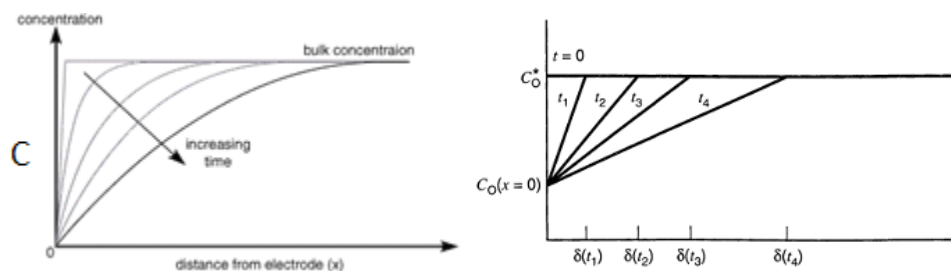
Figure 2: Illustration of diffusion layer growth upon application of step potential. Top left: No diffusion layer before the step potential is applied, Top Right: Diffusion layer development upon application of step potential, Bottom Left and Right: Diffusion layer thickness as a function of time. Courtesy: Teaching notes, Dept. of Chemical Engineering and Biotechnology, University of Cambridge

Consider an electrode immersed in an analyte solution with bulk concentration C. Initially there will be no diffusion layer at the electrode interface. Upon application of specific potential (reduction of oxidation depending on the analyte), the species will be depleted at the electrode interface and a concentration gradient results; leading to formation of a diffusion layer. This diffusion layer thickness is a function of time.[5] At short time size of the diffusion layer is smaller than that of the electrode, and planar diffusion dominates, even at microelectrodes. At very short time scale experiments (e.g., fast-scan cyclic voltammetry) a microelectrode will exhibit macroelectrode (planar diffusion) behavior. At longer times, the dimensions of the diffusion layer exceed those of the microelectrode, and the diffusion becomes hemispherical. The molecules diffusing to the electrode surface then come from the hemispherical volume (of the reactant-depleted region) that increases with time; this is not the case at macroelectrodes, where planar diffusion dominates.

The small size of microelectrodes allows radial diffusion (Fig. 3) of species towards itself which increases current density while the current itself remains small i.e., in pA to nA

range. The ohmic drop between the working and the reference electrode is negligible in this current range allowing microelectrodes to be used in highly resistive media such as non-polar solvents.[2]
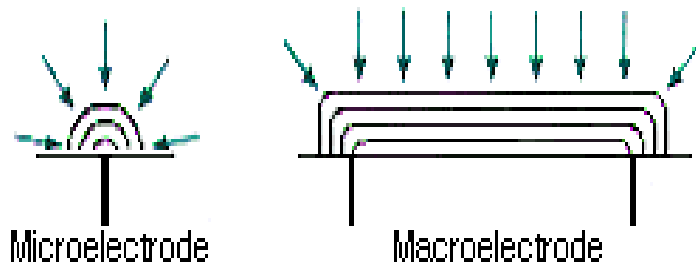
Figure 3: Illustration of diffusion profiles at microelectrode vs. macroelectrode.[5]

For sensing applications, it is important to have a stable current signal at a given concentration. However, for macroelectrodes, longer experimental time scales (in the order of seconds) are needed to achieve such a steady response, as seen from Fig. 2. To achieve a steady current signal different tactics have been employed; such as placing macroelectrodes under a steady sample flow[6] or use rotating disc electrodes[7]. Such tactics are not feasible in unmediated sensing applications. For such sensing applications, microelectrodes offer the solution. The steady state or the limiting current obtained using microelectrodes is given in the following equation[1]:

$$i = \frac{nFA\sqrt{DC}}{\sqrt{\pi t}} + \frac{nFADC}{r} \qquad\qquad \text{Equation 1}$$

where n= number of electrons transferred in a reaction, F= Faradays constant, D is diffusivity, C is bulk concentration of the species, t is the time, r is the radius of the hemispherical electrode, A = area of the hemispherical electrode

6

The equation 1 consists of a Cottrell term; first term on the right hand side and a geometrical correction term; the second term on the right hand side. It can be seen from equation 1 to get a steady state current in a diffusion controlled reaction, one would have to reduce the potential sweep rate substantially (Fig. 4) or one might use a microelectrode to observe the same effect. For equation 1 we see that as the radius of the electrode decreases, the second term starts to dominate and the limiting current is no longer dependent on the time scale (first term) of the experiment. If r is large enough, then one would have to increase the time scale of the experiment, either by chronoamperometry or cyclic voltammetry at reduce the potential sweep rate, to reach as steady state.
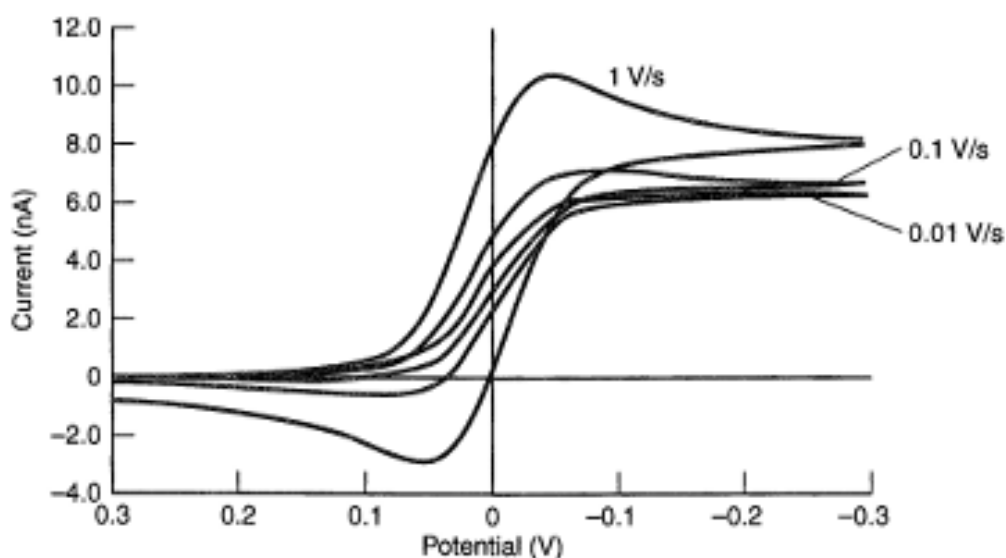
Figure 4: Effect of potential sweep rate on a cyclic voltammogram[5]

2. InterDigitated Electrode Arrays (IDEAs)

2.1 Background

InterDigitated Electrode Arrays (IDEAs), also referred by other names such as InterDigitated Arrays (IDA) or comb microelectrode arrays in the literature, are a special kind of microelectrodes where a set of two working electrodes (microelectrode arrays) are arranged in an interdigitated fashion as seen in Fig. 5. This specific kind of arrangement enables variety of applications such as conductometric sensors[8,9], electrically stimulating tissues[10], dielectrophoretic separation of particles,[11] etc. My thesis only concerns IDEAs that have extremely small gap spacing between digits such that the diffusion layers overlap upon application of specific (to the analyte of interest) potential. The theory of operation of IDEAs is that if two adjacent electrodes in an IDEA are closely spaced and potentially biased then redox species undergo oxidation at the electrode with the higher potential (generator) and the oxidized species undergo reduction at the electrode with the lower potential (collector) before diffusing out into the bulk of the solution. When the redox species cycle between the generator and collector multiple times, we observe a phenomenon known as redox cycling[12]. This behavior results in an amplified signal (also known as redox amplification) thereby lowering the lower limit of detection (LOD) significantly. One needs to operate with electrode gaps in the sub-micrometer range to get a sizable redox amplification factor.
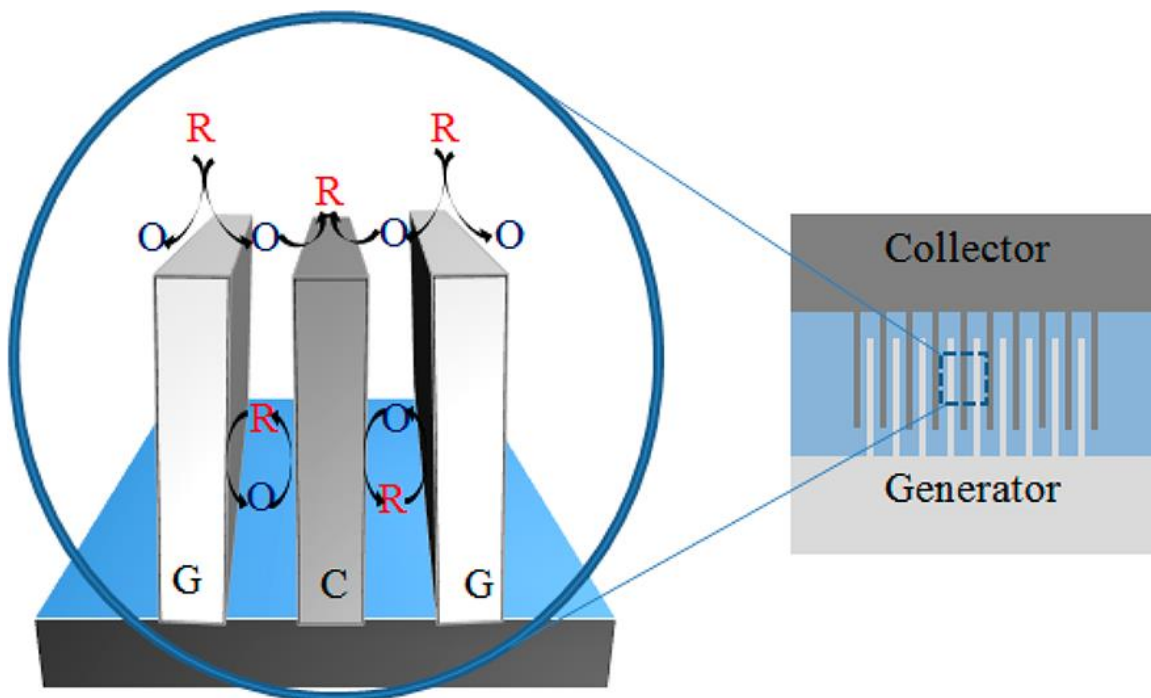
Figure 5: Schematic view of principle of redox cycling in a 3D IDEA. G: Generator; C: Collector. The redox species oxidize at the generator and reduce at the collector multiple times (one cycle is shown here) before diffusing out in the bulk solution.

Redox amplification dependence on geometry

The redox amplified signal using IDEAs is given by the equation 2 where i_r can be either generator or collector limiting current in redox mode. This equation was obtained by Aoki[13] by solving the two-dimensional diffusion equation on a planar IDEA electrode in a steady state.

$$i_r = mbnFCD[0.637 \ln \frac{2.55}{x} - 0.19x^2]$$

Equation 2

where m is the number of electrodes in the array, b is the length of each electrode, n is the number of electrons involved in the redox reaction, F, C and D mean the same as in equation 1. x in the equation 2 is given by

$$x = g / (w + g)$$

where w is the width of individual digits and g is the gap spacing between individual digits. The equation 2 was derived by Aoki using following assumptions: the length of the micro/nano bands is significantly higher than its width , edge effects at the either side of the array is negligible since array consists of large number of bands and both the oxidized and diffused species have same diffusivity. This equation has been verified experimentally by different groups[14,15] and clearly shows the dependence of the limiting current on electrode geometry. Experimental results from Niwa *et.al* [16]demonstrate that the electrode gap spacing and width in IDEAs affect collection efficiencies and number of redox cycles for various redox species. The redox amplification is defined[17] as:

$$RA = i_{g,r} / i_g \hspace{4cm} \text{Equation 3}$$

where $i_{g,r}$ represents the generator current with redox cycling and i_g represents the generator current without redox cycling i.e., in single mode. The redox amplification value can also be approximated from the collection efficiency [17]as:

$$RA = 1 / (1 - CE^2) \hspace{4cm} \text{Equation 4}$$

The collection efficiency, CE, is given by

$$CE = i_c / i_g \hspace{4cm} \text{Equation 5}$$

The collection efficiency is greatly influenced by the gap spacing between the digits. As the gap spacing decreases, the diffusion profiles overlap better thus increasing the chances of

collection of oxidized species and vice versa. Ideally, to get the maximum benefit out of IDEAs one would want the collector electrode to reduce all the species oxidized by the generator electrode. If that happens then the collection efficiency is equal to 1. This has been empirically proven by Niwa *et.al* where multiple redox probes were as function of the gap spacing on planar metal IDEAs.

One starts observing amplification when the gap spacing is less than 10µm. Simulations have suggested that the amplification will continue to increase till the gap spacing reduces to 100nm. Thereafter, no further amplification can be expected.[18] However, achieving such low gap spacing is not an easy task.

2.2 Limitations of traditional noble metal IDEAs

The IDEAs described in the background is made up noble metals using multistep, complex lithographic techniques. To make IDEAs really effective, the gap spacing should be minimized. A traditional process for fabricating noble metal 3D IDEA electrodes with critical dimensions in the sub-micrometer range is shown in Fig. 6

The process starts with patterning the positive photoresist using expensive and sophisticated exposure tools such as deep-UV projection lithography or electron beam lithography. However, these methods have drawbacks—deep UV lithography suffers limitations in resolution due to light diffraction and requires the use of excimer laser to produce 193nm wavelength. Although electron beam lithography provides much higher resolution, it is a serial process that requires high vacuum conditions for its operation. Hence it's laborious, a more expensive proposition thus not amenable for mass

production. The photoresist patterning process is followed by metal deposition step using yet again expensive MEMS technique such as physical or chemical vapor deposition. Noble metals such as Au[19] and Pt[20] are popular choices for fabricating IDEAs. However, Au and Pt exhibit weak adhesion with glass substrates hence they require the use of an adhesion layer (e.g., Cr or Ti) followed by a lift-off step. The lift-off step can have its own problems such as retention, redeposition and earlike structure formation. Moreover, when Au/Cr or Au/Ti bi-layers come in contact with an electrolyte, they may create a galvanic couple that may lead to corrosion, limiting their long-term application in electrochemical cells. While metal electrodes exhibit a lower electrical resistance than carbon, they come with unwanted electrochemical side reactions, even at low potentials. Yet another drawback with metal IDEA fabrication is that they are only be made planar i.e., height of the electrodes will be in nanometer range and cannot be increased significantly to achieve substantial redox amplification. To increase the height of these IDEAs, one needs to do yet another photolithography step using negative photoresist (step 4 and 5) in Fig. 6 followed by deposition of Ni to achieve the height. Finally the residual resist needs to strip off using wet etching followed by electroless deposition of gold. As one can clearly see, fabricating 3D metal IDEAs can get quite labor-intensive.

1. Pattering of positive resist on Pyrex glass

2. Deposition of Cr and Au

3. Liftoff of Cr and Au

4. Spin coating of negative resist and exposure from backside using Cr and Au layer as photomask

5. Development

6. Electrodeposition of Ni using mold of photoresist

7. Removing of photoresist

8. Au electroless deposition on Ni surface
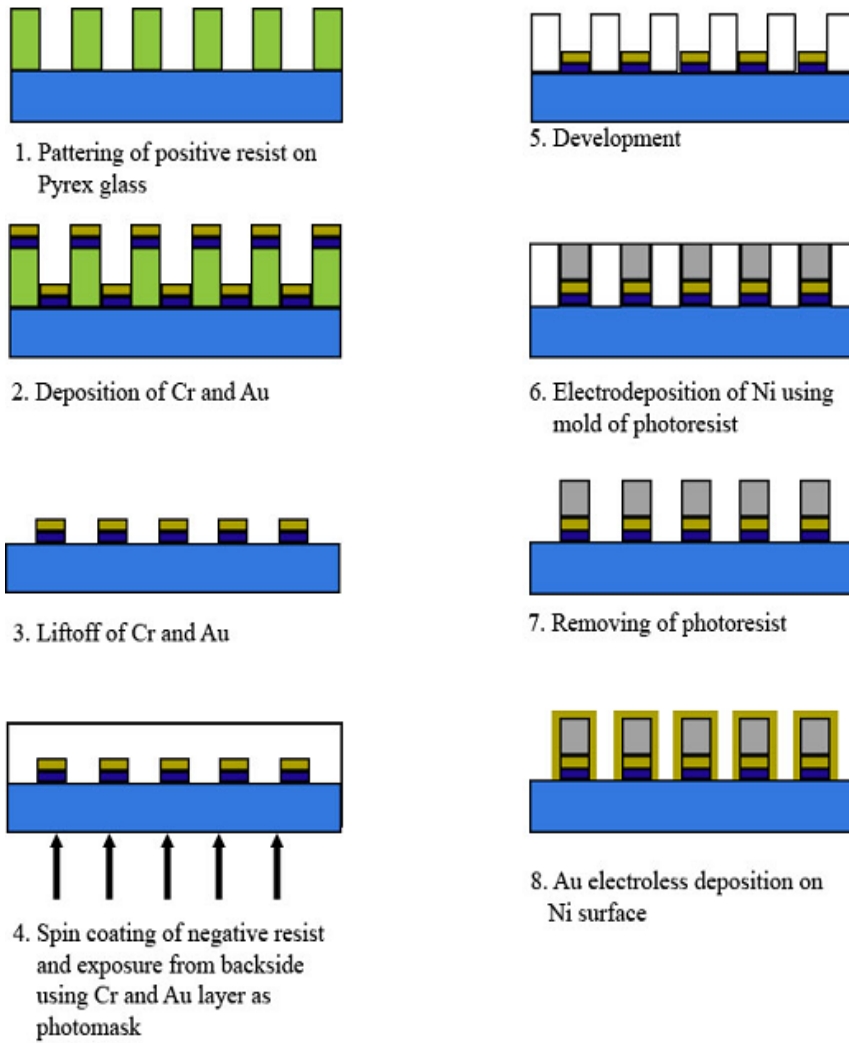
Figure 6: Process schematic of a 3D metal IDA electrode fabrication

2.3 Fabrication of 3D IDEAs using Carbon MicroElectroMechanical Systems (Carbon MEMS)

As explained in the previous section, noble metal IDEAs come with a lot of disadvantages. On the other hand, fabrication using C-MEMS technology solves a lot of these problems. There are many techniques that can yield carbon (similar to glassy carbon) from patterned organic polymers. These techniques are collectively called Carbon MEMS as pioneered by Madou group in the last decade. The patterning of organic polymers can be done by photolithography, micro/nano imprinting, electrospinning or other kinds of machining. Depending on the machining and derivation technique the final dimension of the carbon structures can range from centimeters to nanometers.[21]

The main advantage of using Carbon MEMS for fabrication of IDEAs is possibility to increase the height of the patterns by, say, photolithography which will eventually lead to high aspect ratio carbon IDEAs. Taller IDEAs with narrow gaps significantly improves the probability of confining redox species in the trench between the electrodes thereby amplifying the signal by redox cycling. Moreover, as the IDEAs get taller, the surface area available for the redox cycling also increases. Also, the fabrication process itself is much simpler i.e., involves primary machining technique such as UV photolithography followed by pyrolysis (explained in the next section) in an inert atmosphere as opposed to laborious multi-step process described in Fig. 6.

The electrode so obtained after the pyrolysis process is very similar to glassy carbon.[21] Glassy carbon is chemically very stable and comes with a wider stability window than any noble metal. The stability window is dictated by pH and decomposition of water upon

application of potentials (refer Fig. 7). Glassy carbon shows amazing resistance against corrosive agents and strong acids. It is also thermally inert and has low coefficient of expansion[21]. It also exhibits good biocompatibility and low non-specific adsorption of biomolecules. The oxygen to carbon ratio of the glassy carbon is extremely low and hence it's resistant to bio-fouling. Those are some of the reasons why carbon electrodes, especially glassy carbon electrodes, are the gold standard for studying electrochemical reactions and why glassy carbon makes for an attractive material for fabricating IDEA electrodes.
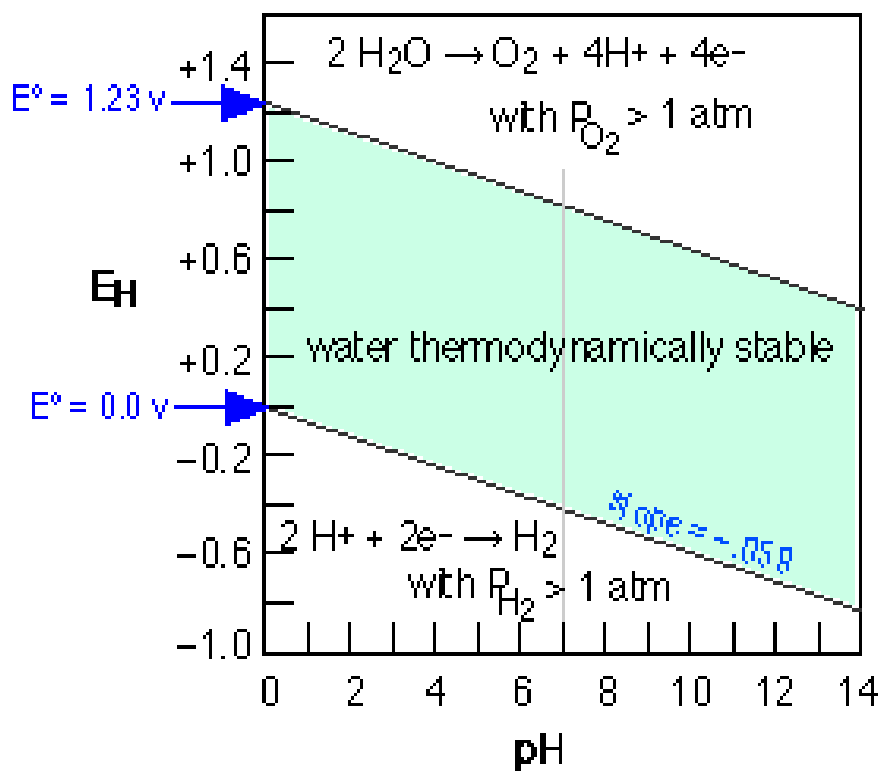
Figure 7: Stability (Pourbaix) diagram for water. Courtesy UC Davis Chemwiki

In our Carbon MEMS process, the patterning is done using conventional i-line UV (365nm) photolithography followed by pyrolysis (heating the patterns in an inert atmosphere at high temperatures i.e., upto 900°C. A schematic of Carbon MEMS technique based on photolithography is shown in Figure 8. The first step involves application of SU-8 layer on a substrate that can withstand high pyrolysis temperatures. Since a single layer of thin SU-8 film, thinner than 5µm is needed, spin coating was chosen as a technique to apply the SU-8 photoresist. The substrate of choice is Silicon with a thin layer (500nm) of thermally grown oxide on top. Si is used as the substrate of choice as it has a melting point over 1400°C and easily withstands high temperatures typically used in furnace during pyrolysis process. The oxide layer (at least 500nm thick) is important as it provides insulation between electrolytes and Si for electrochemical applications. The IDEAs will function only if there is no leakage current between the adjacent bands in the array. Using a bare Si wafer can give leakage currents depending on the resistivity of the wafer and hence will compromise the quality and reproducibility of the IDEAs.

The desired patterns are then transferred onto the resist by exposing the resist to UV light through the patterned stencil or photomask. The transparent regions on the photomask will allow the light to go through and only those regions on the resist will be crosslinked during the post exposure bake (PEB) step. The PEB allows speeding up the polymer crosslinking. PEB is followed by development process where the unexposed regions of the SU-8 dissolve away giving the final desired SU-8 pattern. The height of these structures can be controlled by using appropriate viscosity of the SU-8 and the spin coating parameters.

The SU-8 patterns can then be pyrolyzed in order to carbonize and yield carbon IDEAs. During pyrolysis the nitrogen flow provides an inert environment to avoid combustion. The process yields high quality carbon which is similar to glassy carbon.
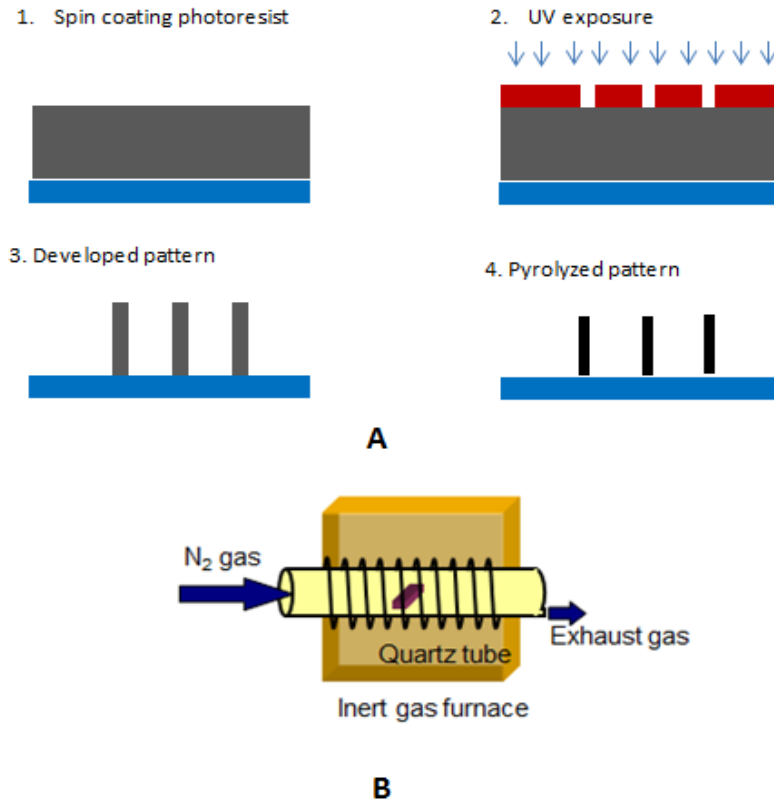
Figure 8: Process Schematic to make Carbon IDEAs. a) SU-8 Photolithography (1-3) and pyrolyzed pattern (4) b) Pyrolysis of the patterned resists in a tube furnace.

2.3.1   SU-8 Photolithography

Substrate and Photomask Preparation

Silicon wafers with 500nm thick oxide layer were purchased from Noel Technologies (Campbell,CA). The wafers were p type, <100> crystal oreientation with resistivity of 1-20

Ohms-cm, 4 inch in diameter and thicknesss of 500-550μm without the oxide. The wafer package was opened and stored in the cleanroom to avoid any contamination. Before any application of photoresist they were dehydrated in dehydration bake oven for atleast 30 mins at 120°C. The dehydration step facilitates better adhesion of SU-8.

Sometimes recyled wafers were used as well. The recycling is done by removing carbon patterns in a piranha bath (3 parts of concentrated sulfuric acid to one part of 30% Hydrogen peroxide heated to 120°C). The wafers are then rinsed with de-ionized water and isopropyl alcohol followed by drying in a jet of compressed notrogen. The wafers are then ready for dehydration in the dehydration bake oven.

The design for the photomask was created in AutoCAD and data file was sent to Photsciences Inc (Torrance, CA) for fabrication. The final product is a fused quartz substrate with chromium patterns. The patterns were created using electron beam lithography and a lift off step by Photosciences Inc.
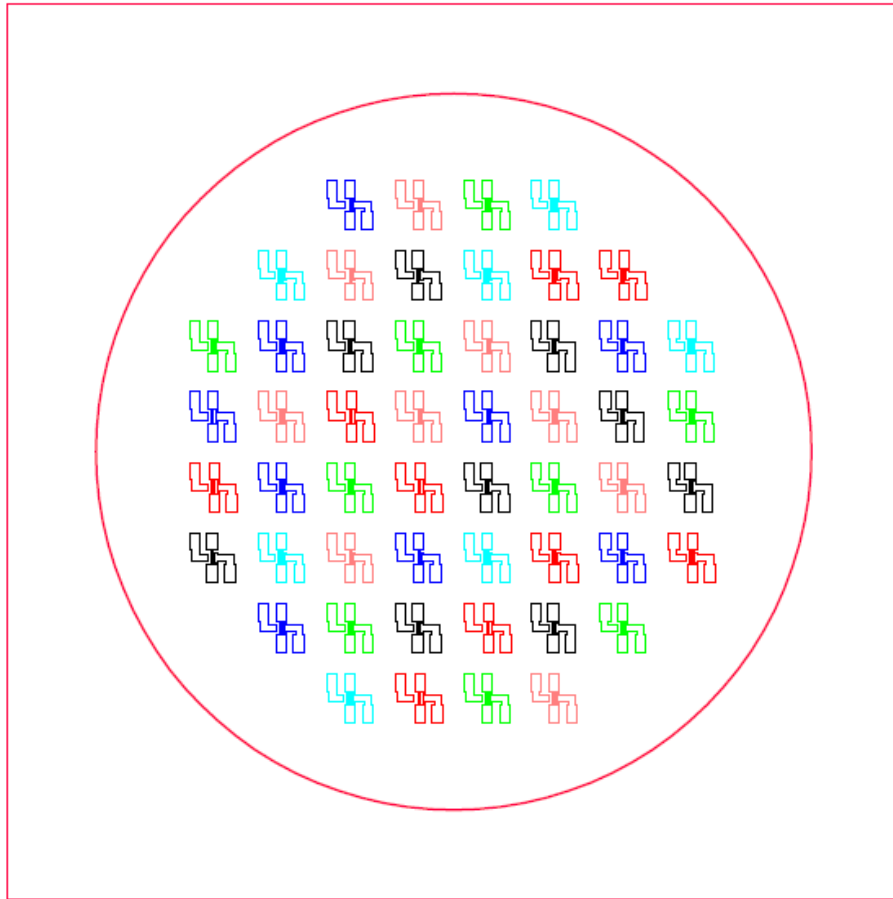
Figure 9: AutoCAD design of the photomask. Different colors represents different pattern configurations i.e., different widths and gaps. The patterns are arranged randomly so as to avoid any bias during the UV exposure step.

Since the exposure step involves hard contact, the mask may get some SU-8 residues which needs to be cleaned off before next exposure step. The residual SU-8 or other contaminants can be cleaned by rinsing the mask with 10% sodium hydroxide followed by rinsing with 1% soap solution. The mask is visually insepcted under 200X optical microscpe to observe any residues. If the contamination still exists, then its recommeded to clean the mask in a piranha bath (for mask, used 5 parts of concentrated sulfuric acid to one part of 30% Hydrogen peroxide heated to 120°C).

SU-8 Spincoating

SU-8 is an acid-catalyzed negative tone photoresist distributed by Microchem Corp (Westborough, MA). The SU-8 (2000 series) consists of bisphenol resin, cyclopentanone as solvent and 10% of triarylsulfonium hexafluoroantimonate, a photoinitiator (Microchem datasheets for SU-8). Spincoating of SU-8 is mostly done on flat substrates. The exact thickness of the spincoat depends on the type of SU-8, based on viscosity, the duration of the spin and the speed of spinner. The spinner holds down the wafer in its place by a vacuum chuck. Care must be taken to ensure the the wafer is cooled down to room temp before positioning it the center of the chuck. Datasheets from Microchem provides guidelines to optimize SU-8 spincoat.

Low viscosity SU-8 was used to produce thin films by spin coating. This was essential to achieve submicrometer gap dimensions during patterning. SU-8 2000.5 (2.49 cSt), SU-8 2002 (7.5 cSt), and SU-8 2005 (45 cSt) were spin-coated according to the manufacturer's recommendationsto produce films of different thicknesses as listed in Table 3. SU-8 2000.5 was used to achieve a 0.6μm height; SU-8 2002 was used to achieve 2.1 and 3.6μm heights (two layers of SU-8 spin-coat) whereas a 5.1μm height was obtained using SU-8 2005. In all of the above cases, the dispensed SU-8 was allowed to completely coat the wafer manually. Then the spinner was switched on to get desired thickness. Manually coating the entire wafer area is extrmely important for low viscosity SU-8 such as 2000.5 or 2002 as otherwise the spincoat will not be uniform and one will typically observe barren areas on the wafer even after the spincoat. This is not the case with higher viscosity SU-8 such as

2025 where the SU-8 (upto 3mL) dispensed at the center will spread evenly upon spincoating. An exmaple of the Laurell spincoater I used is displayed below

Figure 10: Programmable Laurell photoresist spinner Courtesy: UCI Bio-Organic Nanofabrication facility

Soft Bake

SU-8 spincoated wafers are then soft baked at 95°C on a hot plate for a minute before they are cooled down to 50°C while on the hot plate. This process causes a lot of solvent in the resist to evaporate and to promote film adhesion to the substrate. While cooling down slowly on a hot plate is recommended to reduce the film stress it reduces the film thickness as well. In order to maintain the thickness one can keep the baking for 1 min only but this eventually reduces the yield of IDEAs per wafer.

Soft bake is an important step as it ensures that the film is perfectly level to avoid any gaps between the film and the mask during hard contact exposure. Care must be taken that the hot plate is perfectly level. A hot plate works better than oven for soft baking as it causes the film to heat bottom up, eliminating build up of crust on top thus avoiding solvent trapping. This is an issue mostly with thicker films, not so much with the films used for making IDEAs.
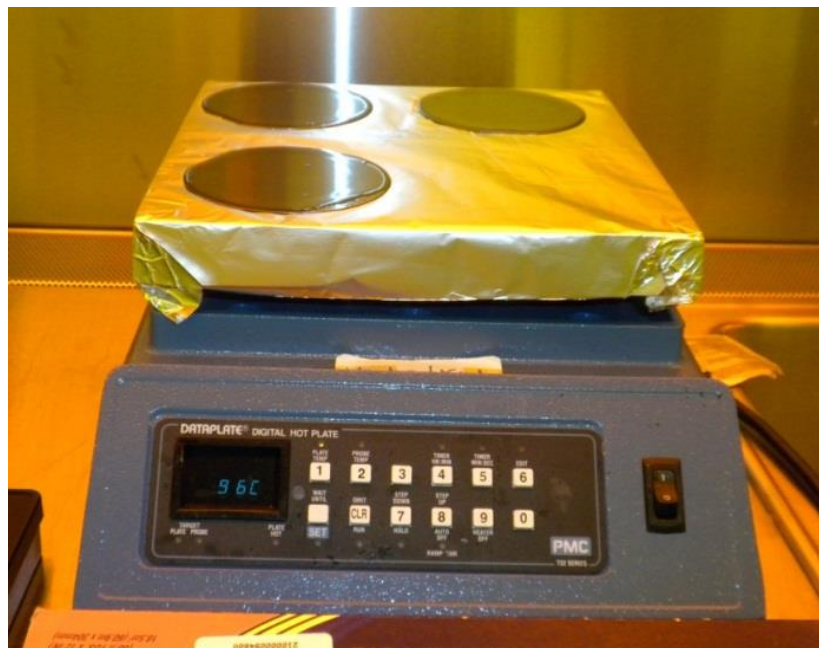
Figure 11: A programmable hot plate for soft bake and postbake.

UV Exposure

The exposure is done using i-line UV (365 nm) using a mask aligner (Karl Suss, Germany). Mask aligner is used primarily for providing a hard contact between the photomask and SU-8 coated wafer. The hard contact ensures little to no diffraction of light between the mask and the wafer, thus ensuring the high level of fidelity provided by the photomask. The

hard contact does occasionally cause the SU-8 particles to stick onto the mask. Therefore its extremely crucial to keep the photomask clean before every exposure step.
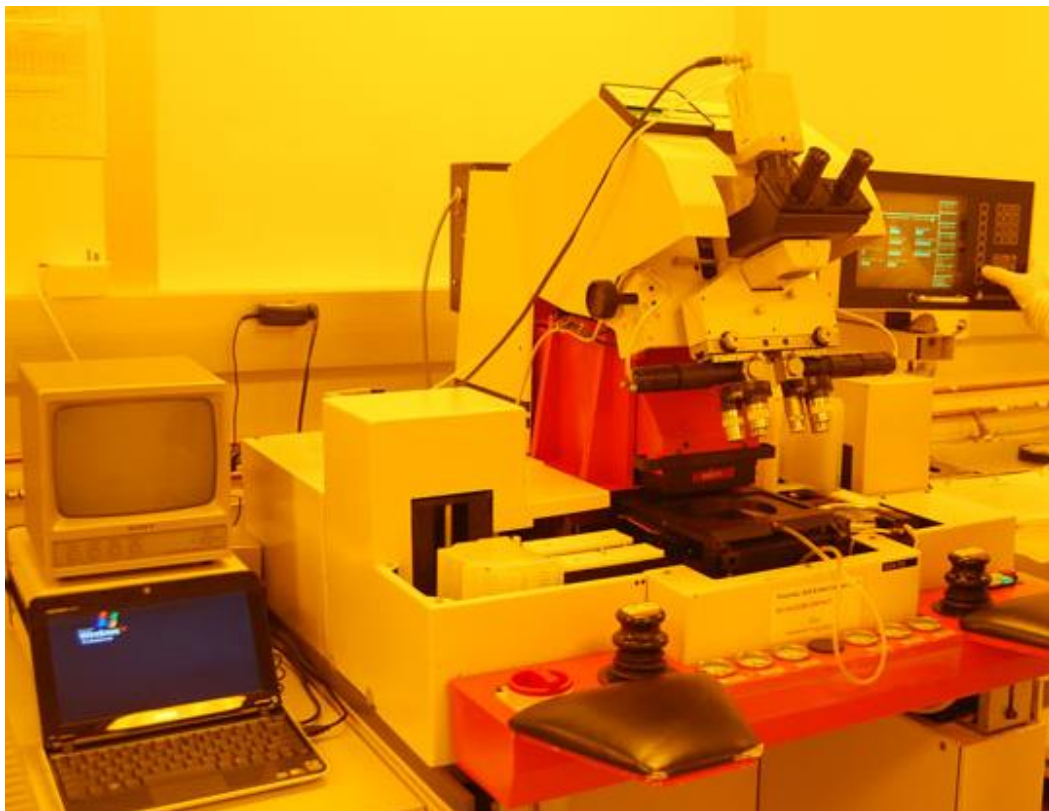
Figure 12: MA56 Karl Suss mask aligner Courtesy: UCI Bio-Organic Nanofabrication facility

The UV dosage for different SU-8 film thicknesses is provided in the Microchem datasheets. It was difficult to achieve complete separation of the generator and collector electrodes using the exposure and post exposure bake (PEB) settings recommended in the Microchem datasheets. Using the recommended exposure dosage and PEB settings (time and temperature) caused IDEAs to merge because, we speculate, the acid generated during exposure diffuses into the unexposed extremely narrow gap spacing. To avoid this, the exposure dosage was lowered to 30 mJ/sq·cm to reduce the amount of acid generated and thus to minimize its diffusion across the generator/collector gaps. Infact, the dosage can be

reduced as low as 10 mJ/sq.cm for all the heights (as described in the Table 3) however, PEB settings need to be compensated as accordingly.

Post Exposure Bake

PEB step catalyzes crosslinking of SU-8 polymer chains in the exposed region. The cross linking depends on both the temperature and the time of the bake. One can either use extended PEB times at lower temperatures or shorter times at higher temperatures depending on final pattern dimensions. The optimization process was started with recommended settings from Microchem datasheets. Keeping the recommended PEB time and temperature caused the SU-8 film to peel off during development due to insufficient adhesion with the substrate. Hence, PEB time was modified from 1 to 2 min at 95°C to 90 min at 55°C to maintain a higher fidelity of the IDEA patterns during development. The lower PEB temperature also helped in reducing the acid diffusion generated in the UV exposure. Similar observations were reported for high resolution fabrication of thin SU-8 film patterns[22]. However, the yield was lower than desired in this case with only 5-10 fully resolved patterns per wafer. On further optimization, it was found that keeping the PEB at 95°C for 1-2 min, followed by baking at 70°C for 1-2 min, followed by baking at 50°C for 3-4 minutes gave a much better yield (up to 30 IDEAs per wafer). The logic behind following this method was to allow the wafer to cool down with a gradient so as to avoid thermal shock. The 3-4 min baking at 50°C, we speculate, is to provide better adhesion whereas the baking at higher temp (95°C for 1-2 min, followed by baking at 70°C for 1-2 min) is for catalyzing cross linking. The PEB is done in conventional oven instead of hot plate. One

might use hot plate as well but may have to increase the time of baking as hot plate can only heat from the bottom whereas oven can provide heat from all around.

However the above settings will vary from equipment to equipment. For example the UV source that we used has 10% variation in dosage across 4 inch wafer space. This might be one of the reasons for poor yield.

Development

After PEB step, the wafer is allowed to cool down to room temperature for a few minutes before they are immersed in developer solution provided by Microchem. The developer, Propylene glycol monomethyl ether acetate (PGMEA), dissolved unexposed, thus uncrosslinked regions of SU-8. For film thickness <5μm development for 1-2 minutes is sufficient. Since aspect ratio is not very high compared to those typically observed in MEMS, one need not use any orbital shaker for the process. The patterns are then rinsed with fresh developer for 10 seconds followed by rinsing with IPA for 10 seconds. At this point, you may observe white residue which indicates that the patterns are underdeveloped. In such case, rinse again with the developer for half a minute followed by IPA rinses. Finally, the patterns are dried under compressed nitrogen and are ready for pyrolysis,

2.3.2 Pyrolysis

The fully resolved SU-8 patterns are non-conductive and therefore cannot be utilized for electrochemical applications. In order to do that, the patterns need to be carbonized by pyrolysis process. The final product of SU-8 pyrolysis contains high carbon content (>70%).

Pyrolysis can be done either in vacuum ($<10^{-6}$ mbar) or under flow of nitrogen (2000sccm) to create inert environment. Nitrogen used should be of ultrahigh purity grade (Airgas, USA) only; industrial grade nitrogen will not work as the presence of any traces of oxygen will cause combustion of SU-8, the end product will be just the wafer with no patterns on top. The process parameters are displayed in the table below.

Table 3: Process parameters for converting SU-8 patterns into Carbon IDEAs

Initial Temp (°C)	Final Temp (°C)	Ramp Rate/Duration
25	300	4.5°C/ min
300	300	60 min
300	900	10°C /min
900	900	60 min
900	25	4.5hrs

Figure 13: RD Webb Mini Furnace with alumina tube for pyrolysis

The pyrolysis process can be divided into two major steps that are: pre-carbonization, and carbonization. Pre-carbonization is typically limited to 300°C and is accompanied by minor loss of mass[23]. It is the carbonization step that the resist experiences significant loss of mass due to removal of oxygen and nitrogen from the SU-8; leading to shrinkage in patterns[24]. During carbonization step, there is significant improvement in conductivity due to carbon catenation process leading to sp2 hybridized carbon with the sp3 matrix. At 900°C we get a high quality glassy carbon like material which shows excellent electrochemical properties. Beyond 900°C, we observe only marginal improvement in electrochemical properties[25]. Also increasing temperature and/or dwell time will only

cause reduction in film thickness which defeats the purpose of fabricating taller IDEAs for redox amplification.

The final carbon IDEAs on SiO_2 chip is shown in Fig. 14. The SU-8 patterns and the corresponding pyrolyzed patterns are also shown. The pyrolysis results in shrinkage which is discussed in greater detail in the next chapter.
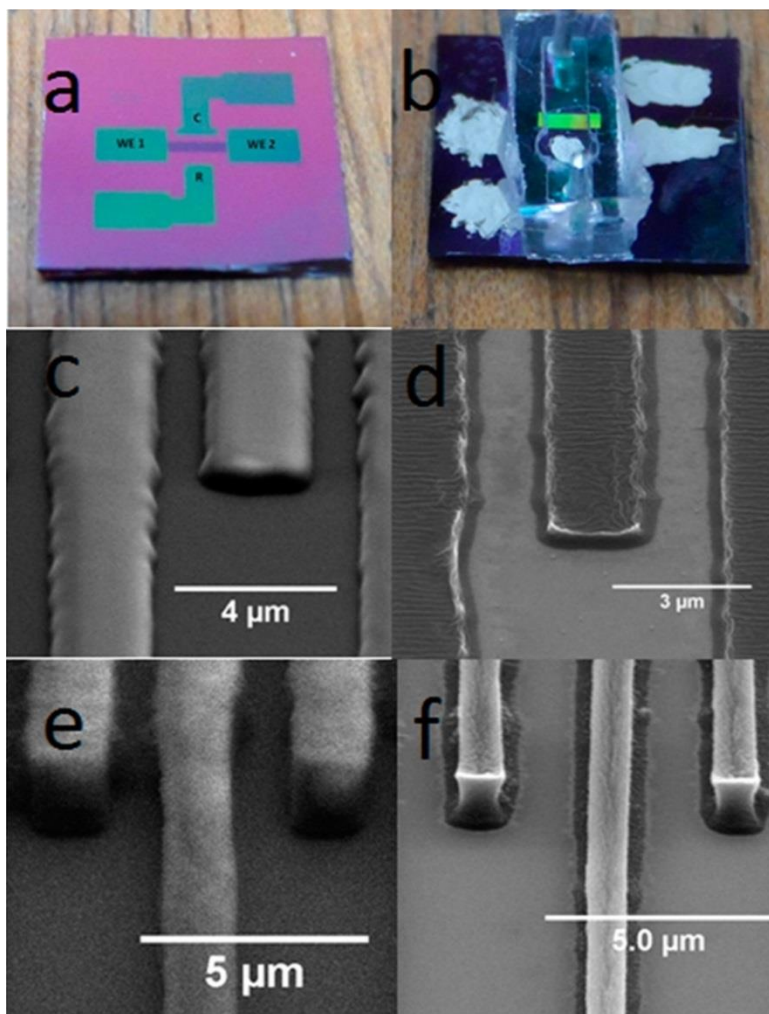
Figure 14: (a) Shows the actual 3D carbon IDEA sensor. WE1 and WE2 are contact pads for the generator and the collector, respectively. C and R are counter and reference electrodes, respectively. (b) Shows the final device with PDMS channels. The reference electrode is coated with Ag/AgCl ink, and contact pads are coated with silver paste for better electrical connection. (c and e) Scanning electron microscopy (SEM) images (tilted view 60°) under 10 000X magnification of SU-8 IDEA patterning before pyrolysis; height = 0.6 and 2.1µm,

respectively. (d and f) Carbon IDEA after pyrolysis; height = 0.22 and 0.59μm, respectively. Exact width and gap specifications are listed in Tables 2 and 3.

3 Electrochemical Characterization of 3D Carbon IDEAs

3.1 Materials and Experimental Methods

Materials

Potassium Chloride and potassium ferrocyanide ($K_4Fe(CN)_6$) were purchased from Sigma Aldrich. All the SU-8 with different viscosities, as stated above, were purchased from Microchem, MA, USA. As discussed earlier, Silicon wafers with 500nm thermally grown oxide were purchased from Noel Technologies, CA, USA. My IDEA design was produced in AutoCAD (student version) and data file was given to Photosciences Inc., CA, USA to print a high resolution chromium patterns on fused quartz glass substrate. All the reagents purchased were of analytical grade.

Experimental Methods

Electrochemical characterization of the carbon IDEAs was carried out by performing cyclic voltammetry and chronoamperometry using 1mM of ($K_4Fe(CN)_6$) for different electrode geometries i.e., width, gaps and heights. Height can be adjusted by spinning photoresist with different viscosities, adjusting spin rate and time and finally by controlling soft bake parameters. For getting different widths and heights, the photomask data file was designed accordingly. For this study, we used four different electrode designs. The two sets of working electrodes, the generator and the collector comprised of 70 digits, each of them 2 mm in length. Each design had a different digit width and two different gap spacings as listed in the Table 2. The counter and reference electrodes, also made from carbon, were fabricated at a distance of 500μm on either side of the array. The carbon electrode intended for reference was coated with a droplet of Ag/AgCl ink and allowed to dry before

experiments. These designs were photolithographically patterned as described before, employing SU-8 on a Si wafer passivated by a silicon dioxide layer. The patterning was followed by pyrolysis under nitrogen flow. Low viscosity SU-8 was used to produce thin films by spin coating. This was essential to achieve submicrometer gap dimensions during patterning. SU-8 2000.5, SU-8 2002, and SU-8 2005 (viscosities as mentioned above) were spin-coated according to the manufacturer's recommendations to produce films of different thicknesses, as listed in Table 2. SU-8 2000.5 was used to achieve a 0.6μm height; SU- 8 2002 was used to achieve 2.1 and 3.6μm heights (two layers of SU-8 spin-coat) whereas a 5.1μm height was obtained using SU-8 2005. The UV exposure was carried out with hard contact between the photomask and the SU-8 coated wafer in a mask aligner (MA56 Karl Suss). The PEB and development was carried out as per the description provided in Chapter 2. Table 2 and 3 summarizes the final carbon IDEA configuration.

Table 4: Digits widths, gap spacings, and height before and after pyrolysis for the shortest 3D IDEAs. H_{bp}= Height before pyrolysis, H_{ap}=Height after pyrolysis. W_b = Width at the base, W_t = Width at the top, G_b = Gap at the base, G_t = Gap at the top. All units are in μm expect Width/Gap ratio.

Height	Width	Gap	Width/Gap (Avg.)
H_{bp}= 0.6, H_{ap}= 0.22	W_b= 0.75 W_t= 0.27	G_b= 0.85 G_t= 1.33	0.47
	W_b= 0.86 W_t= 0.4	G_b= 0.94 G_t= 1.4	0.54
	W_b= 1.75 W_t= 1.0	G_b= 1.05 G_t= 1.8	0.96
	W_b= 2.72 W_t= 2.02	G_b= 1.08 G_t= 1.78	1.66
	W_b= 1.75 W_t= 1.0	G_b= 1.25 G_t= 2.0	0.85

Table 3: Digit widths and gap spacing for different heights before and after pyrolysis. All units are in μm expect Width/Gap ratio.

Height	Width	Gap	Width/Gap (Avg.)
H_{bp}= 0.6, H_{ap}= 0.22	W_b= 2.72 W_t= 2.02	G_b= 1.08 G_t= 1.78	1.66
H_{bp}= 2.1, H_{ap}= 0.59	W_b= 2.72 W_t= 1.99	G_b= 1.08 G_t= 1.81	1.63
H_{bp}= 3.6, H_{ap}= 0.86	W_b= 2.7 W_t= 1.96	G_b= 1.1 G_t= 1.84	1.59
H_{bp}= 5.1, H_{ap}= 1.1	W_b= 2.7 W_t= 1.95	G_b= 1.1 G_t= 1.85	1.58

During the pyrolysis process, the temperature ramp up rate, 10°C/min in this study, is maintained in such a way that the furnace temperature always remains lower than the glass transition temperature of the SU-8. The details of the pyrolysis process were reported elsewhere[25]. Pyrolysis for thicker SU-8 structures (around 10µm) results in a vertical shrinkage of approximately 85%[26]. However, as the SU-8 structure height decreases, the vertical shrinkage decreases from 79% at 5.1µm to 64% at 0.6µm. The digit width at the base where SU-8 is anchored to the substrate remains the same before and after pyrolysis, irrespective of the original width and height. There is definite lateral shrinkage at the top of the SU-8 structures, but the shrinkage is consistent for all the heights studied: from 64% at a 0.8µm digit width to 26% at a 2.7µm digit width. The calculations for the width of electrodes, gaps, and their ratios was done by averaging the measurements at the base and top of the digits[27]. Carbon IDEA samples were characterized by scanning electron microscopy (SEM) and profilometry to determine the feature dimensions. SEM imaging was carried out on a FEI Quanta 3D FEG system, and profilometry was carried out using a Dektak Profilometer. To obtain SEM images before pyrolysis, SU-8 patterns were sputtered with carbon (up to 5nm) using an ion beam sputtering system (model: IBS/e from South Bay Technology, USA). The sputtered SU-8 patterns were not pyrolyzed and not used further in this study. Cyclic voltammograms (CVs) and chronoamperograms (CAs) were studied to determine the electrochemical properties of the IDEAs. CV and CA experiments were carried out on an EDAQ Quadstat 164 setup, Chart software v5, and a Waveform Generator ER175. CVs were carried out in a 0.5M KCl solution containing 1mM $(K_4Fe(CN)_6)$ at two different sweep rates of 50 and 5mV/s. The reference electrode was a pseudoreference of an Ag/AgCl ink droplet (Bio-Logics, USA) coated on the reference

carbon electrode and then dried in an oven at 60°C for 1h. CV experiments were carried out in single and dual mode. For single mode runs, the collector circuit was kept open and the generator potential was swept between −200 and 600mV. In dual mode, the generator potential was swept the same as in single mode but the collector was held constant at −250 mV vs. the reference electrode. For the CA experiments, the generator was kept at an oxidation potential of 400mV and the collector was kept at −250mV, in the case of dual mode. After approximately half a minute of dual mode operation, the collector was disconnected to measure generator current in single mode

For steady state experiments, experiments were conducted in a stationary solution. To ensure very little evaporation of the solution during the duration of the experiment, the IDEA was enclosed in a PDMS channel. The PDMS channel ensured that there is little to no evaporation of the solution during the course of the experiments. PDMS channels were crafted using plastic molds carved out on a cutter plotter. The channels were sealed onto the IDEA sensor substrate using a 2:1 mixture of base to curing agent (PDMS precursors, Sylgard, USA). The mixture, used as an adhesive, was allowed to cure at 70°C overnight. PDMS channels that were 1.5mm wide and 100μm high were used for all experiments. The inlet and outlets of the PDMS channels placed over the IDEAs were connected to PTFE tubing for supplying the electrolyte solution to be tested. ($K_4Fe(CN)_6$) solution was introduced into the inlet using a syringe pump (World Precision Instruments, USA). For flow experiments, the infusion rate was kept at 500nL/s. The flow rate corresponds to a linear velocity of approximately 3mm/s for the channel dimensions with the flow orthogonal to the IDEAs. To get rid of any trapped air in the channel, the solution was

allowed to flow over the IDEAs for a few seconds before the CA and CV readings were taken.

3.2 Signal Enhancement as a function of width/gap ratio (no flow)

The dependence of redox amplification on the electrode width and electrode gap is known.[17,28] Aoki *et al*[29] and is given in the equation 2. The electrode height as well as the potential sweep rate was not factored in this equation.

To evaluate the performance of carbon IDEAs in a stationary solution (no flow), redox amplification factors and collection efficiencies were evaluated for different gaps as well as for different width/gap ratios and different electrode heights. It has been observed by different groups[17,28] that if the electrode width is kept constant, then the amplification factor increases as the gap between the electrodes is reduced. This is because the diffusion path for redox species cycling between IDEA digits is reduced. Fig. 15 shows the redox amplification and collection efficiencies for different width/gap ratios at a fixed electrode height of 0.22μm. This height was achieved by pyrolyzing the thinnest SU-8 film (0.6μm) pattern that we could reliably pattern. We also wanted to test for the maximum amplification that can be reached for the thinnest attainable carbon film. So far the maximum amplification attained for such carbon IDEAs is 13 (see Fig. 15). Table 2 lists the dimensions of the digits before and after pyrolysis used in Fig. 15. It can be noted from Table 2 that as the width/gap ratios increase, the gaps increase only slightly, whereas the widths increase significantly. The significance of increasing the width for improving redox amplification in IDEAs hasn't been reported yet. The amplification factor as a function of

width/gap ratio in Fig. 15 shows a steep increase at the higher width/gap ratios. It can also be observed from Fig. 15 that the collector efficiency is getting closer to unity for higher width/gap ratios. Our observation for an increase in amplification via an increase in the digit width is explained as follows: The diffusion layer thickness is proportional to the timescale of the experiment as well as the width of the individual digits.[30] As the width of a digit increases, the diffusion layers of individual digits overlap more and hence, the signal becomes proportional to the surface area of the whole array (keeping number of digits constant) instead of being dependent on the sum of areas of the individual digits. In such a case, the greater the overlap, the smaller the current signal.[31] In single mode, the potential is only applied to alternate digits; hence the diffusion layers will show less overlap (say at 5mV/s) or even none at all (say at 50mV/s). By widening the digits we improve the overlap, thereby reducing the signal and improving the amplification as the redox amplification factor is calculated as the ratio of the generator current in dual mode to the generator current in single mode. In dual mode, diffusion layers for consecutive digits more readily overlap. As opposed to single mode where greater overlap causes reduction in signal due to linear diffusion, the greater overlap in dual mode increases current due to redox cycling. Hence dual mode current is significantly higher for wider electrodes. In summary, increasing the digit width optimizes redox amplification by decreasing the denominator (single mode generator current) and increasing the numerator (dual mode generator current). Even though reducing the gap between electrodes is an important factor in improving redox cycling, it is obvious from these results that one can also focus on increasing the width/gap ratio by increasing width to improve redox cycling. This is especially true in case of conventional UV photolithography where achieving gaps in the

36

submicron range is challenging. For gap spacings where the diffusion profiles already overlap, one expects the amplification factor to increase until an electrode width is reached corresponding to the redox species diffusion length.
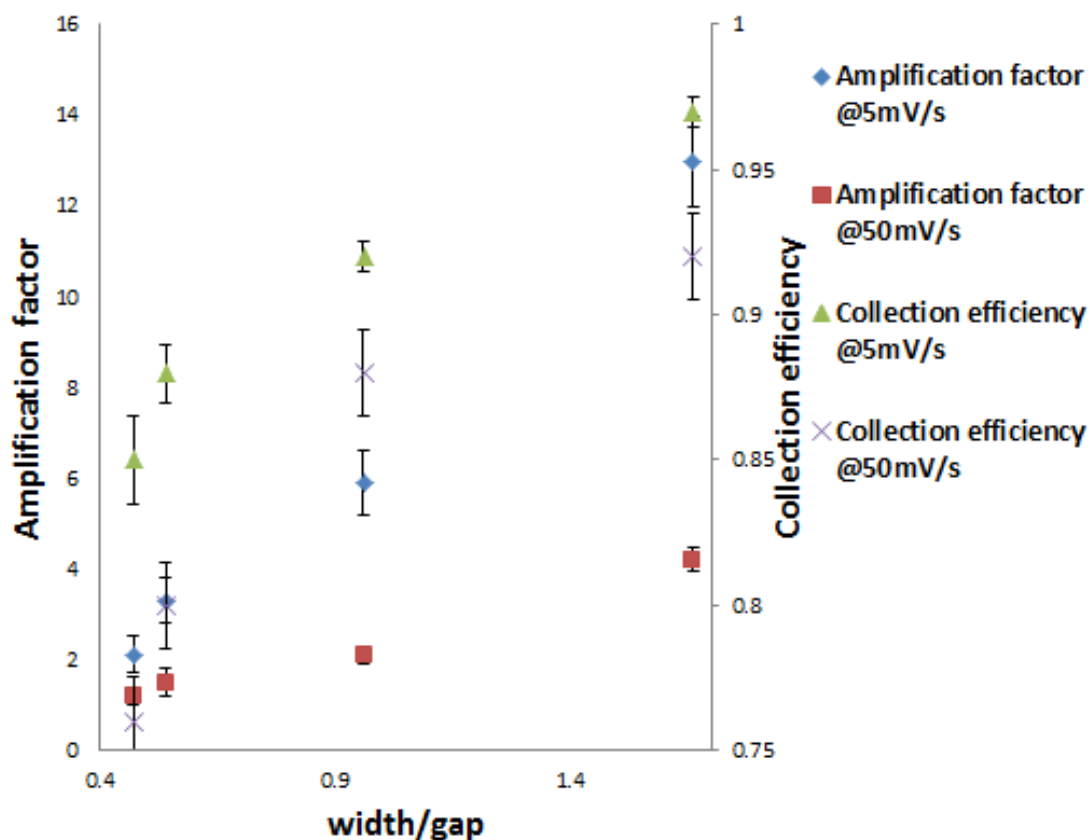
Figure 15: Amplification factor and collection efficiency vs. width/gap ratio at 0.22 µm height under no flow condition. Width/Gap ratios are derived from Table 2.

3.3 Effect of voltage sweep rate on sensor performance

In Fig. 16 we show CVs at two different potential sweep rates: 5mV/s and 50mV/s for both single and dual mode operation. At 50mV/s in single mode, one can see a typical CV curve for a 1mM $K_4Fe(CN)_6$ solution with both oxidation and reduction peaks visible. A similar

CV curve is obtained at 5mV/s, although with lower current. For CV's that feature peaks, the Randles Sevcik equation holds[32]

$$i = 0.4463nFAC\left(\frac{nFvD}{RT}\right)^{0.5}$$ Equation 6

where n is the number of electrons transferred in the redox event, v is the sweep rate in V/s, R is the ideal gas constant, and T is temperature in K. The rest of the symbols have the same meanings as described for equation 1. It can be seen that the peak current is proportional to the square root of the sweep rate. At higher sweep rates, the rate of consumption of the redox species at the electrode surface is very high, and diffusion from the bulk cannot provide enough mass transport to reach a steady state. Insufficient mass transport causes the current to peak (equation 6). At lower sweep rates, the rate of consumption of the redox species is lower and the diffusion from the bulk is fast enough to achieve steady state; hence instead of a redox peak, a diffusion plateau results. Once this steady state regime is reached, the magnitude of the limiting current becomes independent of the sweep rate and relies on the geometry of electrode.[5] The magnitude of this limiting current is much lower compared to the peak current obtained from equation 6, but is still in direct proportion to the concentration of the redox species at the electrode surface. In Fig. 16, the peak shaped CVs in single mode at 50mV/s may be either due to the partial overlap of the diffusion layers or simply because the diffusion layers haven't grown wider than the characteristic (smallest) dimension of the individual digits.

In dual mode, the efficient cycling of the redox species between the IDEAs enhances the mass transport to such an extent that the limiting current becomes independent of the sweep rate. The hysteresis between the anodic and the cathodic current in the CV curves is

reduced significantly, indicating that steady state is being approached. The CV for both the generator and collector electrodes generally displays a typical sigmoidal shape, although with significantly larger limiting current than in single mode due to redox cycling. This enhanced mass transport by cycling the redox species between IDEAs has an equivalent effect to that of the non-linear, diffusion contribution in the case of micro electrodes where a sigmoid behavior can be seen even at relatively large sweep rates due to the enhanced mass transport. The current rise to the plateau, in the case of carbon electrodes, is less steep than the case of highly conductive IDEAs. The conductivity of carbon IDEAs is not quite as high as that of noble metals (100S/cm for glassy carbon vs. 4×10^5S/cm for Au) and hence the CV shows an iR drop resulting in a current that gradually increases towards the plateau instead of a sharp rise towards the limiting current. Adding iR drop effects to the simulations results in a similar CV as observed experimentally with carbon IDEAs.[33]

The generator current in single mode at 50mV/s is much higher than that at 5mV/s due to sweep rate dependence. At lower sweep rates, the time available for redox cycling is longer and hence the redox species cycle a greater number of times. Hence, the collection efficiency is higher at lower sweep rates, i.e. 0.97 at 5mV/s compared to 0.92 at 50mV/s. As seen from Fig. 16, the difference in generator current at 50mV/s and 5mV/s in single mode is significant, while in dual mode the difference is minimal. In single mode the current is lower at lower sweep rates, as discussed earlier (refer equation 6)
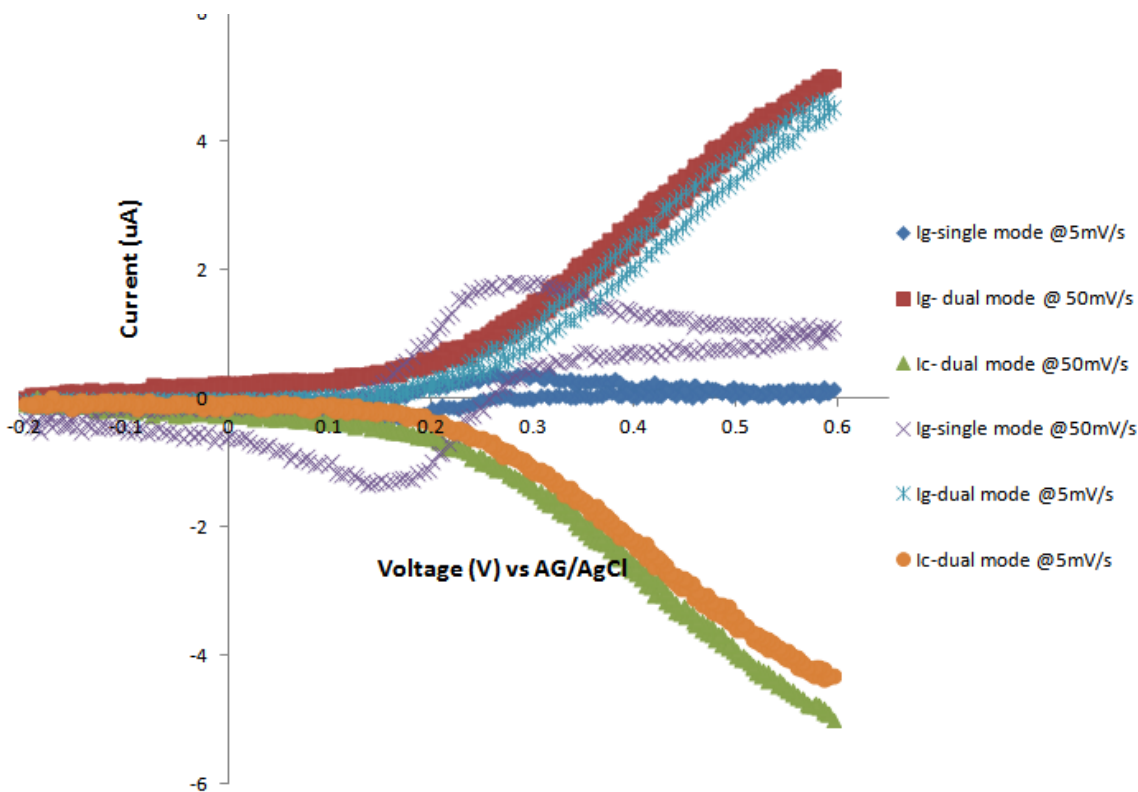
Figure 16: Cyclic Voltammograms of 3D carbon IDEAs in 0.5M KCl and 1mM K$_4$Fe(CN)$_6$ solution. IDEA parameter; width/gap 1.58 height; 1.1μm. Refer Table 3 for exact specifications.

3.4 Signal Enhancement as a function of electrode height (no flow)

One of the biggest advantages of using SU-8 UV photolithography is that it allows for simpler implementation of high aspect ratio IDEAs. As the height of the electrode increases, the surface area available for redox species to interact with electrodes increases. More importantly, this greater height confines redox species in the trench between the electrodes, allowing for more efficient redox cycling. This phenomenon was experimentally demonstrated by Dam et al[20] using platinum IDEAs with a height of 7μm and a gap spacing of 1μm. The design allowed these authors to reach amplification factors of up to 70. Their experimental results were validated through simulations by Odijk et.al.[27] Through

simulations, Kim et.al[34] demonstrated that the diffusion pathways between the vertical walls of the electrodes are linear whereas the diffusion pathways between the horizontal edges are elliptical. Hence, the practical distance for diffusion is shorter for 3D high aspect ratio electrodes. In Fig. 17, we see that at a sweep rate of 5mV/s, the collection efficiency increases steadily from 0.97 to 0.985 while, with increasing electrode height, the amplification factor increases dramatically from 9 to 37. Our experimental results showed that the difference between the generator and collector current in dual mode was more or less constant at all electrode heights. However, it was observed that the current increased with height which is why an increase in the collection efficiency is observed. This goes to show that one needs to exploit the height of the IDEAs at low sweep rates to get sizeable signal enhancement.
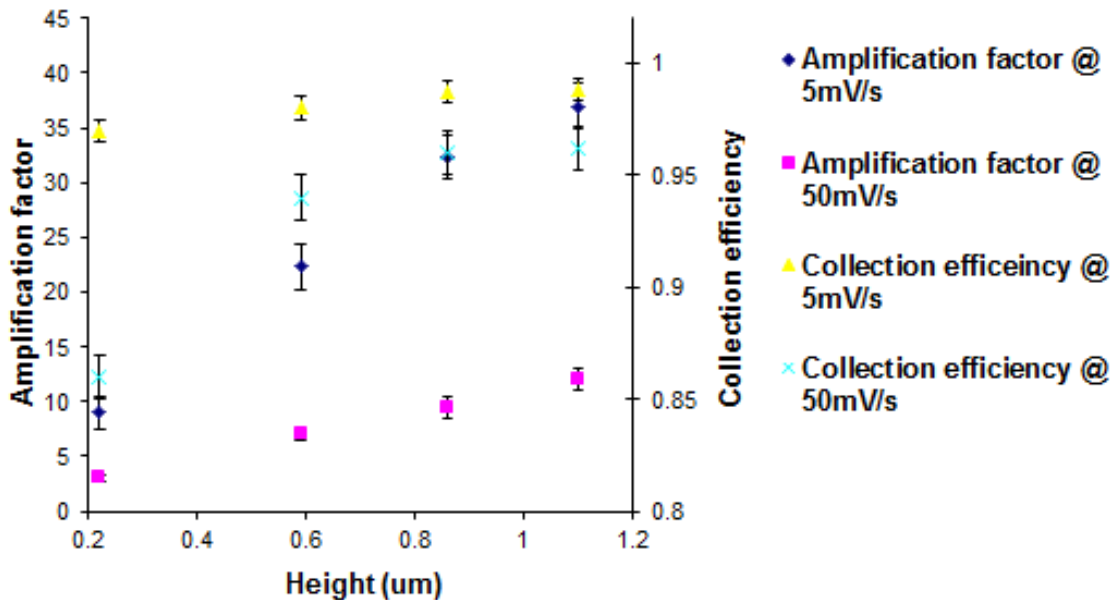
Figure 17: Amplification factor and collection efficiency vs. height at a width/gap ratio of 1.6. Refer to Table 3 for dimension details.

3.5 Effect of flow on redox cycling for different heights and width/gap ratios

It is expected that a solution containing electro-active species flown over an electrode will increase the amperometric signal[5] and IDEAs have also been shown to be extremely efficient in improving the sensitivity of electrochemical detection. It was only natural to combine the two to investigate redox cycling at IDEAs in flow injection analysis[16] and high-performance liquid chromatography.[35,36] The effect of flow on collection efficiency and redox cycling has been studied for planar IDEAs.[37,38] but the effect of flow on 3D IDEAs has not yet been investigated.

In single mode, the current under flow conditions is linearly proportional to the cube root of flow rate as shown in Eq. 7[5] :

$$I = 1.47 nFC(\frac{DA}{B})^{\frac{2}{3}} v^{\frac{1}{3}}$$

Equation 7

where B is channel height and the other variables have the same meaning as defined equation 1. Hence, when the IDEA is operated in single mode, we get approximately 7 times higher current under flow (500nL/s) as compared to the stationary situation demonstrated in Fig. 18. The influence of flow in dual mode is somewhat more complicated. It was observed that the generator current in dual mode under flow conditions was smaller than the current under stagnant conditions (refer Fig. 18). The underlying reason is that in stagnant solutions, and especially for flat IDEAs, elliptical diffusion plays a dominant role in redox cycling. Indeed, under high lateral flow conditions, mass transport is mainly due to lateral convective flow (replacing diffusion from the top in the case of a stagnant solution), elliptical diffusion at the electrode edges, and linear diffusion between the vertical walls of

the electrodes. Elliptical diffusion is impeded by the flow as half of the redox species that contribute to redox cycling by elliptical diffusion at the horizontal edges move in the direction of the flow (downstream) and the other half move in the opposite direction (upstream). The redox species that go upstream are impeded by convective flow, reducing the collection efficiency, whereas the species that go downstream are assisted by the flow[39]. This elliptical diffusion effect can be seen from Fig. 18, where with an increase in IDEA height, the difference in dual mode generator current between flow and no flow conditions decreases. The difference is 1.5% in taller IDEAs (0.59μm) vs. 12% in shorter IDEAs (0.22μm). The flow mainly affects elliptical diffusion, which is a dominant factor in redox cycling for shorter IDEAs. With an increase in IDEA height, the linear diffusion in redox cycling dominates and the difference in generator current decreases. It can be concluded that the generator current in dual mode under no flow conditions is always higher (refer Fig. 18), whereas the generator current in single mode under flow conditions is higher. Thus, redox amplification decreases under flow.
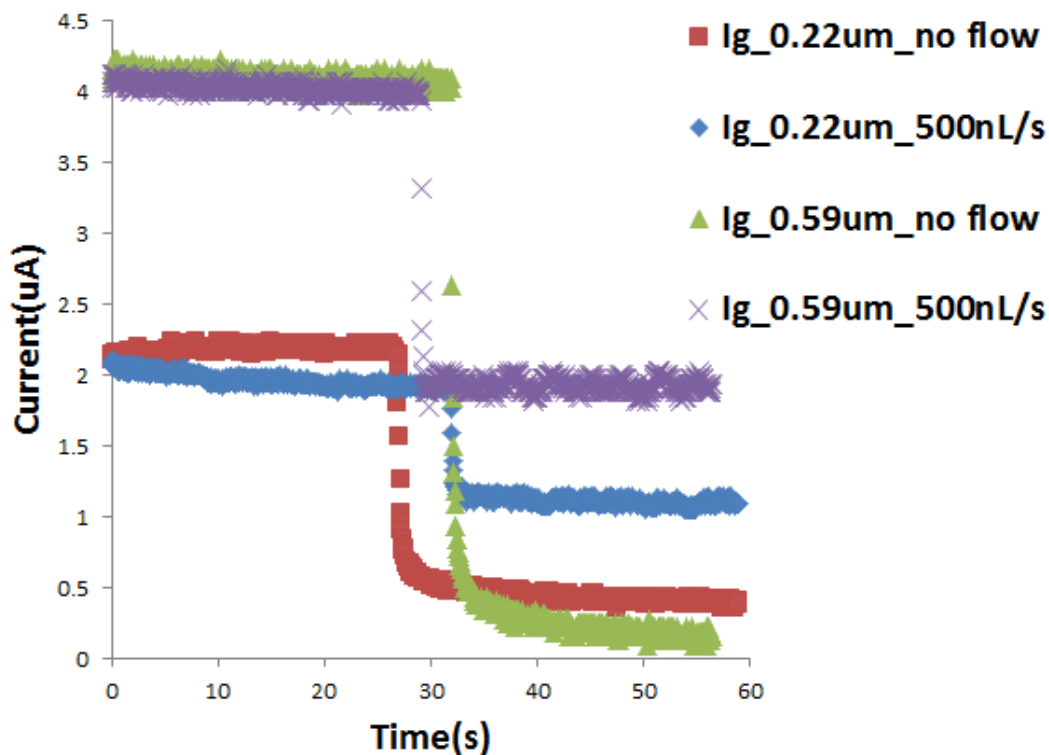
Figure 18: Chromoamperogram of 3D carbon IDEAs under flow and no flow condition for different IDEA heights: 0.22 and 0.59μm. Generator current was measured in dual mode for approximately 30 seconds, followed by single mode.

In Fig. 19, we demonstrate the sensor performance under flow at different electrode heights and observe that there is a steeper increase in amplification for taller IDEAs (slope of 2 from 0.59μm to 1.1μm) compared to shorter ones (slope of less than 1 from 0.22μm to 0.59μm). This data suggests that with a further increase in IDEA height, the detrimental effect of flow on redox cycling will continue to diminish. The result falls in line with our explanation about how flow mostly affects elliptical diffusion. The effect of flow wears off with the increase in IDEA height, where linear diffusion starts to dominate.

44
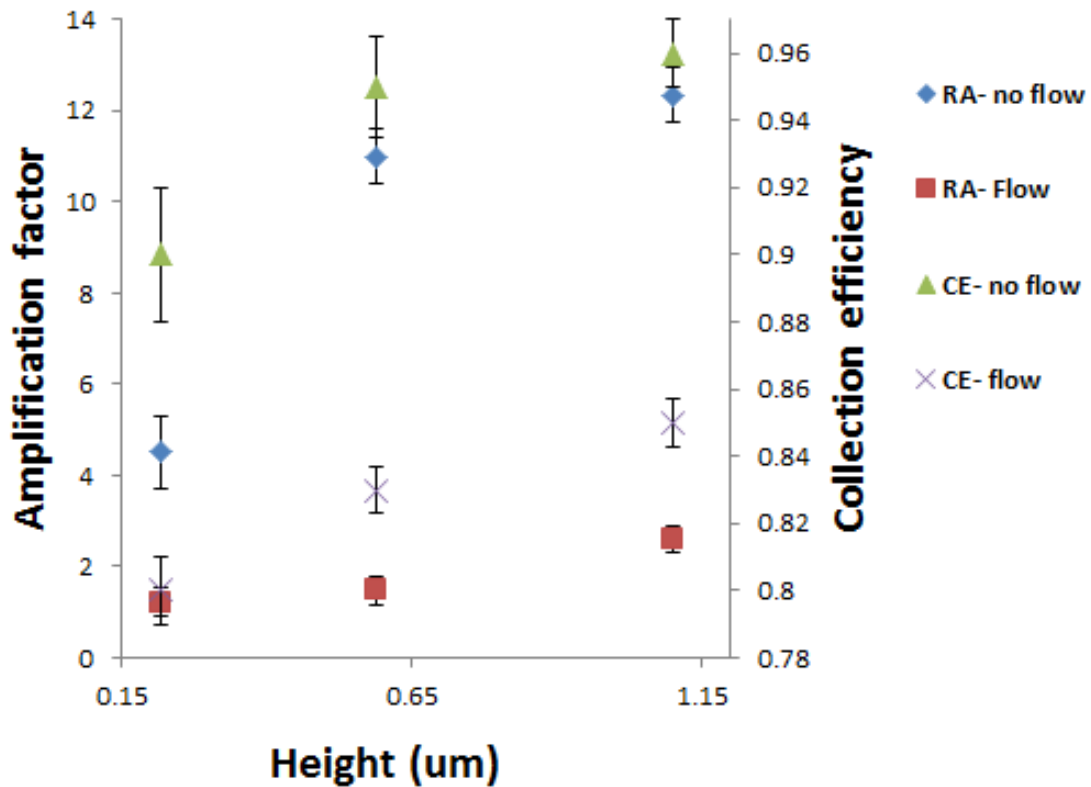
Figure 19: Redox Amplification and collection efficiency as a function of height under flow (500nL/s) and no flow conditions. IDEA width/gap ratio: 1.21

As evident from Fig. 20, the width/gap ratio has very little impact on redox amplification under a high flow rate of 500nL/s. As width/gap ratio increases only elliptical diffusion increases which is hampered by the flow. Under flow conditions, the amplification factor increases marginally as the width/gap ratio is increased. For the lowest width/gap, the amplification factor is only 1.8, whereas it is 3.4 for the highest ratio. As explained above, these low values of redox amplification are due to the poor collection efficiency at a flow rate of 500nL/s. We also learned that to achieve better collection efficiencies, the mass transport due to convection needs to be reduced.[37]
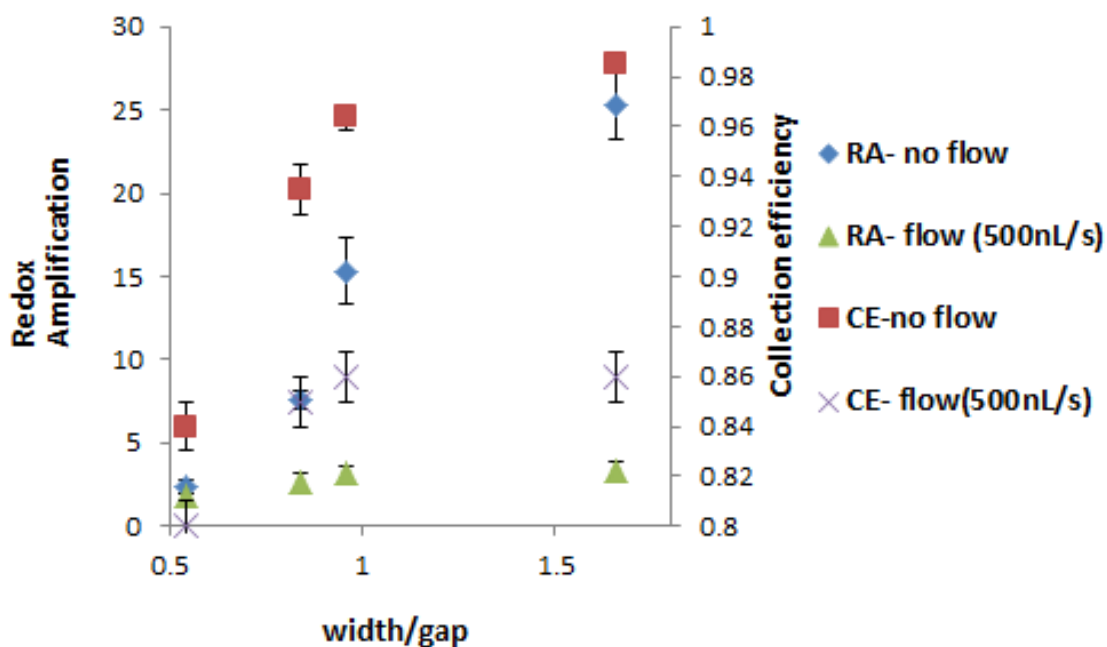
Figure 20: Redox Amplification and collection efficiency at flow and no flow conditions vs. width/gap ratio. Height = 0.59μm

Detection Limit

Since the dependence of redox amplification and collection efficiency on IDEA geometry, sweep rate, and flow conditions has been established, the next step is to find out the detection limit for our 3D IDEAs. The detection limit was found for our best IDEAs under no flow conditions. It can be seen that current exhibits linearity with respect to an analyte concentration between 1μM and 10mM. The slope corresponds to a sensitivity of 5.8nA/μM. The average noise signal in single and dual mode corresponds to 1nA. The detection limit calculated using $3\sigma/m$ criteria corresponds to 0.5μM. This detection limit is impressive considering the fact that the electrode surfaces were not activated electrochemically or by mechanical polishing.
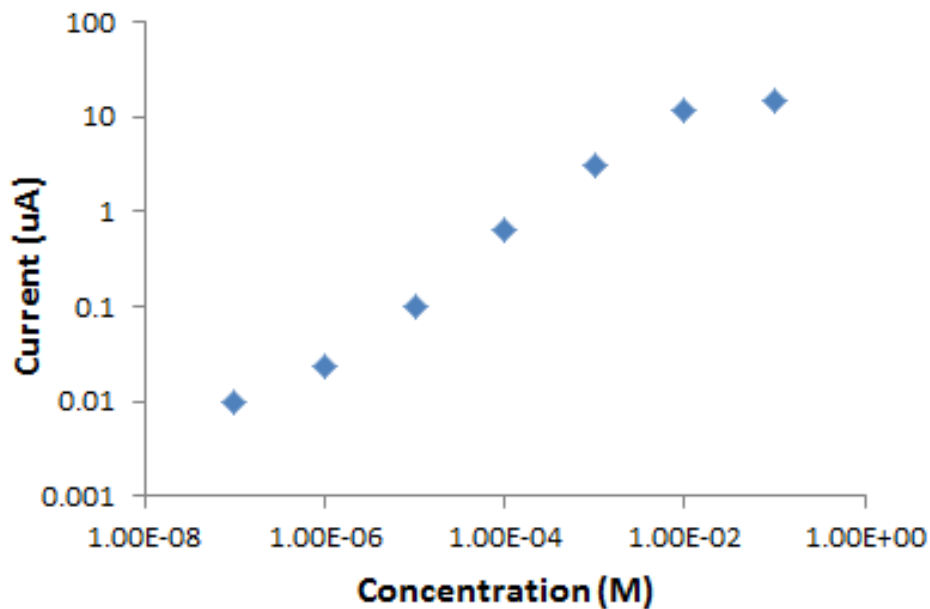
Figure 21: Redox cycling current as a function of the concentration of the $K_4Fe(CN)_6$ in 0.5M KCl at the IDEA with a width/gap ratio of 1.58 and height of 1.1µm.

Currently our best electrodes are the ones with the width/gap ratio of 1.58 (see table 3) and height of 1.1µm that provides amplification factor of 37. This factor is half of the maximum amplification factor recorded for the 3D platinum IDEAs i.e., 74 by Dam *et al*. The group used platinum electrodes which had height of 7µm and width of 2µm, gap of 1µm at the top. To achieve amplification similar to the one achieved by Dam *et al,* the height of 3D carbon IDEAs needs to be increased. Predicting the exact height required to achieve a factor of 70 is not intuitive as the amplification does not linearly increase with height for 3D carbon IDEAs. This is mainly because the digit side wall profile varies with different heights. Also, it will require further optimization of photolithography parameters to completely resolve the same gap spacings at higher SU-8 heights, which may be extremely difficult using conventional UV lithography. The fabrication of 3D platinum electrodes by

Dam *et al* requires steps such as reactive ion etching, metal evaporation and lift-off, whereas we have demonstrated a much simpler method to fabricate 3D IDEAs.

4. Carbon IDEAs for Selective Amplification of Neurotransmitters

4.1 Selective Amplification of Dopamine against Excess Ascorbic Acid Interference

4.1.1 Background and Motivation

Dopamine is a water soluble catecholamine derived from amino acid tyrosine. Its produced in the midbrain in the dopaminergic neurons of the ventral tegmental area, the substantia nigra pars compacta, and the arcuate nucleus of the hypothalamus. Dopamine, a neurotransmitter, is crucial in a variety of biological and chemical processes in the mammalian central nervous system.[40,41] Amongst others this neurotransmitter plays a significant role in motor control, neuro-recognition and reward-motivated behavior.[42,43] Imbalance of dopamine in the basal ganglia region of the brain has been associated with neurological disorders such as Parkinson's disease, Huntington's disease and Tourette's syndrome.[44–46] An abnormality in dopamine production may even lead to schizophrenia[47] and other psychiatric disorders of neuro developmental type such as attention deficit–hyperactivity disorder.[48] Some studies have shown that dopamine may also play a direct role in damaging cellular macromolecules.[49] The importance of detecting dopamine accurately for pathological research as well as a diagnostic tool is well documented.

There are several challenges associated with dopamine detection. First of all, dopamine has short plasma half-life. It undergoes oxidation easily in slightly alkalike pH to form dopaminequinone.[50] Dopaminequinone undergoes intramolecular cyclization to form a substituted indole species that is not electrochemically active.[51] However, this reaction has slower kinetics and it can be stopped using closely positioned microelectrode arrays such

as IDEAs. The collector in the IDEA can reduce the dopaminequinone back to dopamine, thus preventing its degradation.

Dopamine coexists along with electrochemical interferents such as ascorbic acid in the extracellular fluid. The major challenge in detecting dopamine is to separate its electrochemical response from that of ascorbic acid as their redox potentials overlap significantly.[52,53] In addition, dopamine is present in much lower concentration (1-10μM) compared to ascorbic acid (100-500μM) making its accurate detection even more challenging.[4452,53] While dopamine detection in an excess of ascorbic acid has been achieved using chemically modified electrodes[54], a drawback of the latter is that they require laborious multistep process including the use of expensive materials such as nanoparticles.[55,56] Besides, various electrochemical methods have been employed for determining dopamine. These include differential pulse voltammetry[57], fast scan cyclic voltammetry[53] and Chronoamperometry[58] amongst others. Differential pulse voltammetry offers excellent sensitivity but suffers from poor temporal resolution i.e. time taken to complete molecular aggregation of dopamine can be in the order of minutes. Chronoamperometry offers excellent temporal resolution but suffers from poor selectivity whereas large background currents are inherent with fast scan cyclic voltammetry affecting the lower limit of detection.

Since dopamine is electrochemically reversible, redox cycling of dopamine between closely spaced working electrodes, to increase detection limit, represents an attractive alternative detection method. During redox cycling, the dopamine undergoes oxidation to form

dopaminequinone at the generator while the dopaminequinone will be reduced back to dopamine at the collector.

<div style="text-align:center">

dopamine   dopaminequinone

</div>
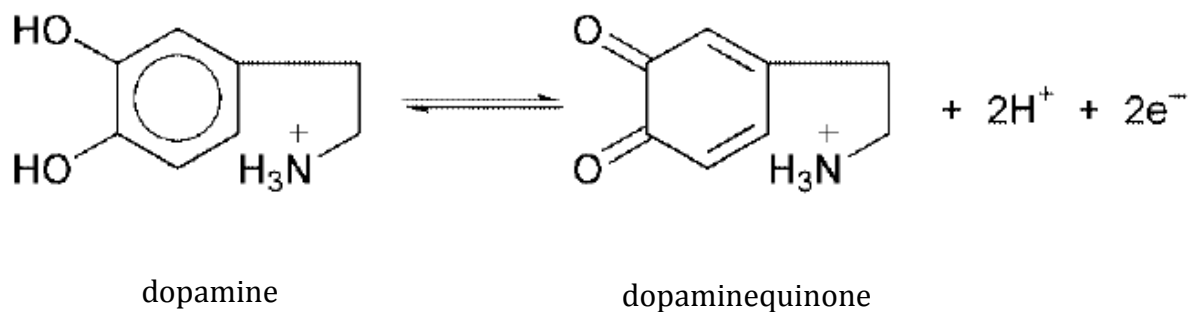
This amplification can significantly reduce the limit of detection for dopamine. However, the excess ascorbic acid present in physiological samples may reduce dopamine-quinone before it reaches the collector thereby interfering in the redox cycling process.

Although several groups[59–61] have used redox cycling to determine dopamine at low concentrations, almost none have detected dopamine in the presence of excess ascorbic acid as under physiological conditions (concentrations and pH). Niwa *et.al*[15] used gold interdigitated electrode arrays for dopamine detection in excess ascorbic acid but his measurements suffered from poor selectivity. Thereafter, Niwa et. al[59] used a complex process to modify the gold electrodes with a Nafion/ Polyester layer in order to improve the selectivity but the Nafion membrane suppressed the diffusion coefficient for dopamine making the measurements sluggish. Vandaveer et. al[61] used a sophisticated technique to fabricate an array of gold recessed microdisk (generator) adjacent to the elevated gold tubular nanoband (collector) electrodes for redox cycling of dopamine. Although the

authors claimed that their design could have a physiological relevance, it didn't provide sufficient redox cycling at low dopamine to ascorbic acid concentration ratios (<1:2) due to the ascorbic acid consuming dopamine-quinone before it could reach the collector. Aggarwal *et.al*[60] used a unique design of gold microelectrode arrays to induce redox cycling to detect dopamine in physiologically relevant concentrations without the need to modify the electrodes. However, fabrication of the gold electrodes itself is fraught with complications (discussed below).

To the best of our knowledge our technique involving the use of three-dimensional (3D) carbon interdigitated electrode arrays (IDEAs) for selective and sensitive determination of dopamine in excess ascorbic acid under physiological concentrations and pH without chemically modifying the electrodes is the first such attempt.

4.1.2 Materials and Experimental Methods

Materials

All chemicals were used as received. Dopamine Hydrochloride, L-Ascorbic Acid, and Sodium Dodecyl Sulfate (SDS), all analytical reagent grade, were purchased from Sigma Aldrich. 1x Phosphate Buffered Saline (PBS) at pH 7.4 was prepared in the lab using NaCl, KCl, Na_2HPO_4 and KH_2PO_4, all obtained from Sigma-Aldrich. The negative photoresist SU-8 2002 was purchased from Microchem. Inc. MA, USA. Silicon wafers passivated with 500nm oxide layer were obtained from Noel Technologies, CA, USA. These wafers were used as received for the Carbon MEMS (C-MEMS) fabrication process. Our IDEA design was printed on a high resolution chrome photo-mask obtained from Photosciences Inc, CA, USA.

Sensor Fabrication

The carbon IDEAs were fabricated as per the description provided in Chapter 2. For this particular application the focus was on achieving selective amplification rather than going for the highest redox amplification. Hence carbon IDEAs that gave high yield fabrication i.e., with heights below 2µm were used.

The resulting carbon IDEA patters, with 70 pairs of digits, have a digit width of approximately 1µm at the top and 1.7µm at the base, a gap of 1.1µm at the base and 1.8µm at the top, a length of 2mm and a height of 0.6µm. Along with each IDEA, two more carbon electrodes were patterned per chip and served as reference and counter electrodes. For the reference electrode, the carbon electrode was spotted with a droplet of Ag/AgCl ink (BioLogic, USA) to establish a pseudo reference electrode. To ensure minimal evaporation of the solution during the course of experiments, we constructed.
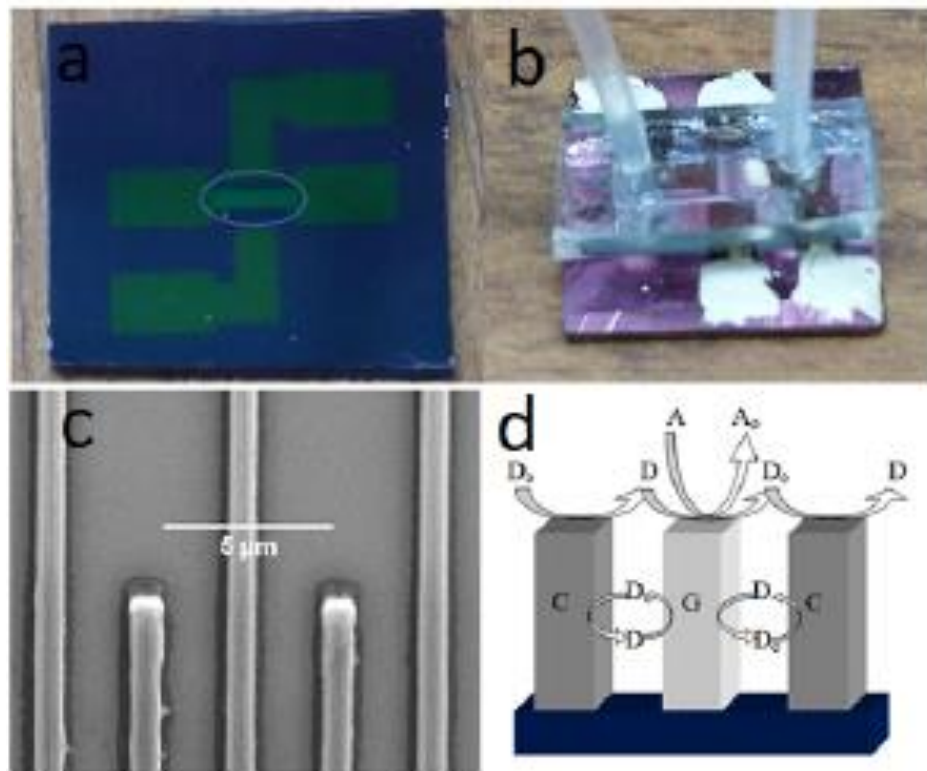
Figure 22: a) Carbon IDEA sensor chip after pyrolysis. The IDEA sensing region is marked as shown; the sensor is connected to contact pads to the left and right. The IDEA is also flanked by a counter electrode at the top and a reference electrode at the bottom. b) Final device with PDMS channel with inlet and outlets. The four white patches at the edges are silver paste contacts. c) Scanning electron microscopy (SEM) image of the IDEA at 8000X magnification, top view. d) Schematic of redox cycling at the 3D IDEAs. D: Dopamine, Do: Dopamine-quinone, A: Ascorbic Acid, Ao: Dehydroascorbic acid

Sensor Characterization and Electrochemical Measurements

The dimensions of the carbon IDEAs were characterized using SEM imaging (FEI Quanta 3D FEG system) and a Dektak profilometer. Cyclic Voltammograms (CVs), Linear Sweep Voltammograms (LSVs) and Chronoamperograms (CAs) were studied to determine the electrochemical behavior of dopamine and ascorbic acid in the presence and absence of 4mM SDS. All the electrochemical experiments were carried out on a EDAQ Quadstat 164

set-up, Chart software v5 and a Waveform Generator ER175. CV and CA experiments were carried out both in single and dual mode. All the experiments were carried out with a stationary solution above the electrodes. The solutions were introduced into a Polydimethylsiloxane (PDMS) flow channel via Teflon tubing using a syringe pump. The PDMS channels were 1.5mm wide and 100µm tall.

4.1.3 Results and Discussion

Determining the potential scanning window for the dopamine redox cycling experiments

The biggest challenge for selective determination of dopamine in an excess of ascorbic acid is to separate the redox peak potentials of dopamine and ascorbic acid. Our work was inspired by the work of Alarcón-Angeles *et.al.*[62] This group used SDS in the sample to mask interference by ascorbic acid and to determine dopamine levels with differential pulse voltammetry using carbon paste electrodes and obtained a lower limit of detection of 5µM.

Sodium Dodecyl Sulfate

SDS is an anionic surfactant. When it is present in as solution above its critical micellar concentration (CMC) it adsorbs on the electrode forming micellar aggregates. This causes solubilization of electroactive compounds such as dopamine and ascorbic acid near its vicinity. This induces changes in redox properties of dopamine as well as ascorbic acid, also changing the energy transfer and diffusion coefficients.[62] It was observed that the peak oxidation potential of dopamine and ascorbic acid differed by as much as 240mV in the

presence of 3mM SDS. This referenced work is promising for the quantification of dopamine as the test does not rely on expensive materials or laborious processes and no electrode modification steps were involved. However, all the experiments were conducted at pH 3.0 which is much different than the physiological pH. The authors also observed that as the pH of the solution increased, the peak oxidation potential for dopamine decreased significantly which deteriorates the limit of detection.

The most important advantage of using SDS as the masking agent is that it ensures that the peak oxidation potential difference between ascorbic acid and dopamine is greater than 240mV. We took advantage of this observation by Alarcón-Angeles *et.al* and combined it with our 3D carbon IDEAs. The first experiment we carried out was to check if the oxidation peak potential separation (>240mV at pH 3.0) is still valid at physiological pH. We carried out LSVs of 1mM dopamine and ascorbic acid separately with and without 4 mM SDS. At 4mM the concentration is greater than its critical micellar concentration. As can be observed in Fig. 23 (left), the peak oxidation potential for dopamine before the introduction of SDS was around 240mV with respect to the pseudo-reference electrode. In the presence of 4mM SDS, the oxidation peak shifted to the right by only 10mV. We did observe a decrease in the peak current by 12% in the presence of SDS but this loss can be recovered by redox amplification in dual mode.

The LSVs obtained for ascorbic acid show similar results as observed by Alarcón-Angeles *et.al*. The peak oxidation potential for ascorbic acid in the absence of SDS is around 250mV which overlaps significantly with the oxidation potential of dopamine under similar conditions. In the presence of 4mM SDS, the oxidation peak for ascorbic acid is around

56

530mV, a positive shift of 280mV. Since the onset of oxidation is around 450mV vs. the pseudo-reference it makes sense to reduce the potential scanning window, for redox cycling, up to 450mV to eliminate interference from ascorbic acid. By reducing the potential window of operation, we selectively redox cycled dopamine in the presence of excess ascorbic acid.
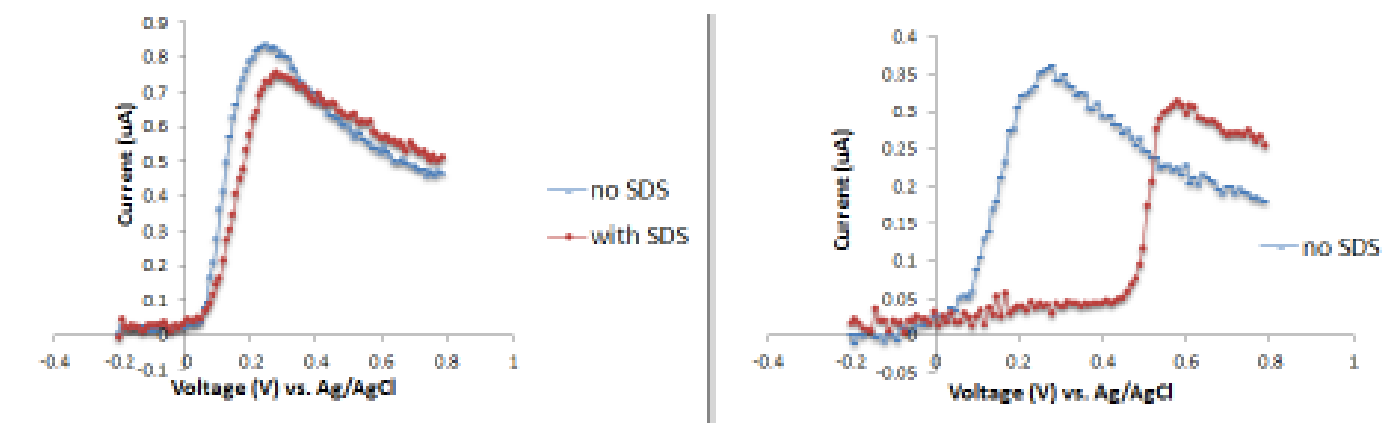
Figure 23: Left: LSVs of 1 mM dopamine in 1xPBS (7.4 pH) in the presence and absence of 4mM SDS. Right: LSVs of 1 mM ascorbic acid in 1xPBS (7.4 pH) in the presence and absence of 4 mM SDS

Redox cycling in the presence and absence of SDS

Redox cycling was carried out in dual mode with the generator potential either scanned in the potential windows shown in Figs 24 and 25 or held constant above the dopamine oxidation potential (CA) with the collector held at -250mV in either case. Fig. 24 illustrates CVs (at 50mV/s) both in redox cycling mode and non-redox cycling mode. The CVs were carried out in the absence of SDS to study the effect of ascorbic acid on the redox amplification. In single mode, the contribution of ascorbic acid to the generator current is

significant since the peak potentials of dopamine and ascorbic acid overlap (see Fig. 23). Indeed in the absence of ascorbic acid a considerable drop in the generator current is observed. In dual mode, the redox cycling of dopamine takes place just as any standard redox probe would. We observed low single mode generator current and significantly higher the generator current in dual mode due to redox amplification. Upon introduction of ascorbic acid, the amplification decreases to 4. This is for two reasons: 1) the single mode generator current is higher due to additional oxidation of the ascorbic acid at the generator and, 2) the dual mode generator current is lower as dopaminequinone undergoes a spontaneous reduction in the presence of ascorbic acid to form dopamine while ascorbic acid is oxidized to form dehydroascorbic acid.[63]

The cycling of dopamine by ascorbic acid interferes with the cycling by the IDEAs and hence there is a drop in collection current. The resultant drop in the collection efficiency due to scavenging nature of the ascorbic acid on dopaminequinone deteriorates the redox cycling by the IDEAs. The dehyroascorbic acid undergoes spontaneous hydrolysis to form products that are not detected at the electrodes. As the number of CV cycles increases, more and more ascorbic acid is eliminated in the process and the signal to noise ratio improves although it will take many redox cycles to eliminate 0.1mM ascorbic acid completely. Another way of eliminating ascorbic acid is by pre-oxidizing it by holding the IDEAs at constant oxidation potential but this could take time in the order of minutes.
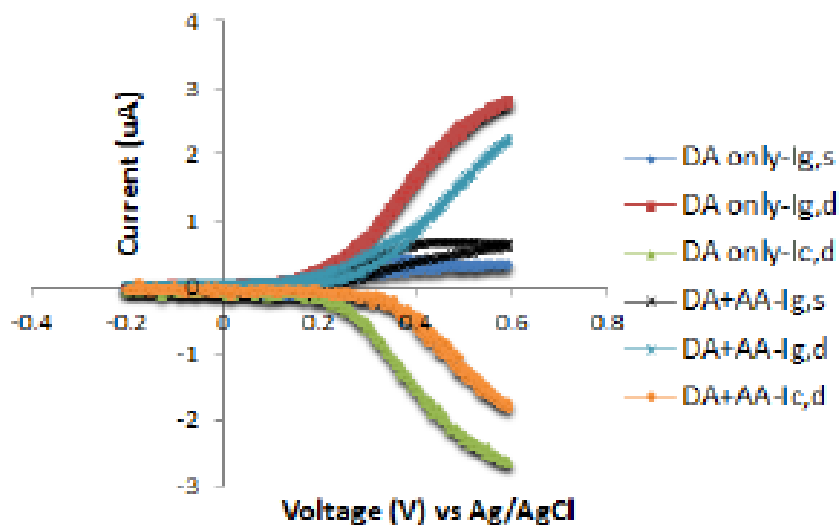
Figure 24: CVs of 0.02 mM dopamine in the presence and absence of 0.1 mM ascorbic acid in 1xPBS (7.4pH). The solution contained no SDS

In the presence of 4mM SDS, the redox potential for ascorbic acid shifts 280mV positively whereas the redox potential of dopamine is almost unaffected. Hence the generator potential in this case was swept at a reduced potential window from -200mV to 450mV to avoid the ascorbic acid interference. It can be observed from Fig. 24 that the single mode currents for dopamine in the presence and absence of ascorbic acid remain almost the same. This shows that the ascorbic acid hardly affects the single mode current at 450mV in the presence of 4mM SDS while dopamine dominates the generator current. In dual mode, the generator current for dopamine shows a 10-fold enhancement as compared to the single mode. The amplification factor is similar in the presence of ascorbic acid. The generator current in dual mode for dopamine in the presence and absence of ascorbic acid is almost identical demonstrating negligible background current at 450mV in the presence of 4mM SDS.
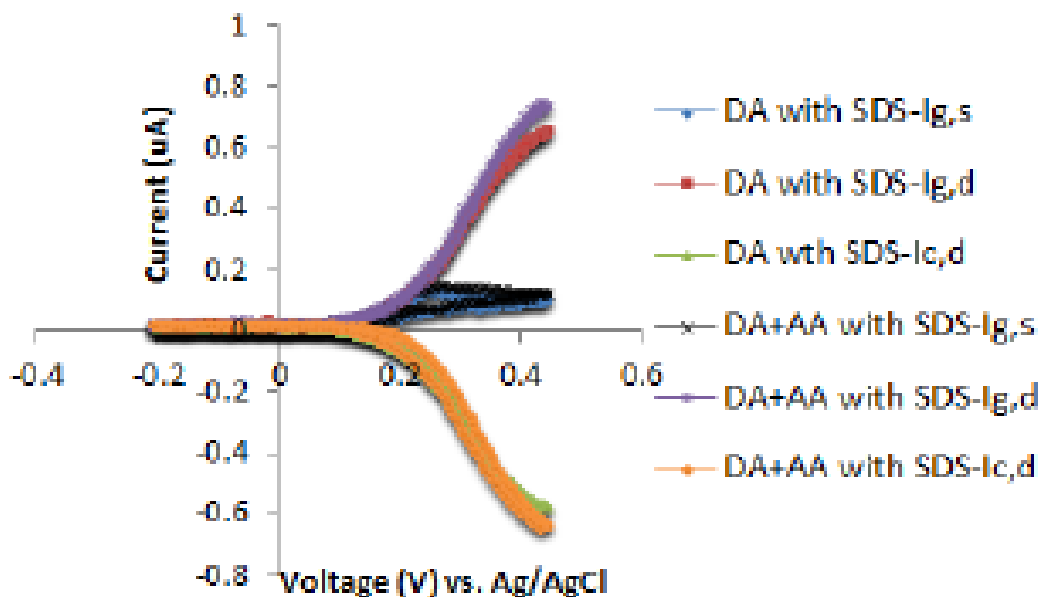
Figure 25: CVs of 0.02mM dopamine in the presence and absence of 0.1 mM ascorbic acid in 1xPBS (7.4 pH). The solution contained 4mM SDS

When the concentration of dopamine is lowered to less than 0.01mM in the presence of 0.1mM ascorbic acid a significant drop in the redox cycling was observed. A similar effect was observed by Niwa *et.al*[15] and Vandaveer *et al*[61] at a low ratio of dopamine to ascorbic acid. In our setup the ascorbic acid does interfere with redox cycling at extremely low dopamine concentrations, however, the low background current at 450mV in the presence of 4 mM SDS allows us to reach a low limit of detection.

The background current associated with ascorbic acid with and without SDS is displayed in Fig. 26. The generator here was held constant at 450mV and the collector was held at -250

mV. The significant drop in the background current in the presence of SDS allows for a low limit of detection of 1.5µM and a linearity range of 5µM to 500µM.

For determining detection limits, dual mode currents obtained for different dopamine concentrations in 0.1 mM ascorbic acid in SDS using Chronoamperometry.
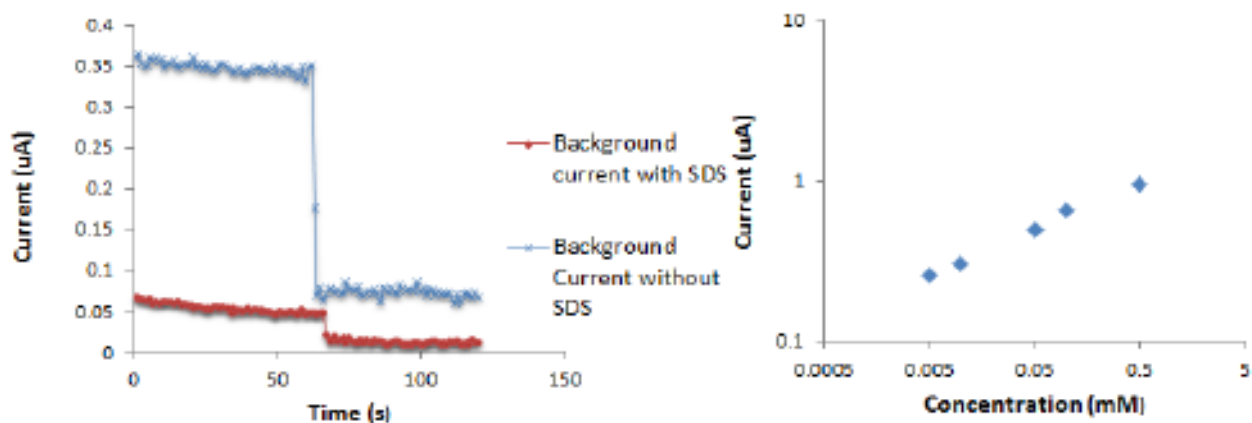
Figure 26: Left: CA of 0.1 mM ascorbic acid in 1xPBS (7.4pH). Right: Dual mode generator current vs. dopamine concentration in 1xPBS at 7.4pH, 4 mM SDS

Conclusion

A method to selectively determine dopamine in the presence of ascorbic acid at physiological concentrations and pH was demonstrated. The method employed redox cycling of dopamine using 3D carbon IDEAs which were fabricated using traditional 365 nm UV photolithography followed by pyrolysis in an inert environment. The electrodes were used without any modification using only SDS at a concentration greater than its critical micellar concentration to achieve a detection limit of 1.5µM.

4.2 Selective Amplification of Dopamine and Epinephrine in their Mixture

4.2.1 Background and Motivation

Epinephrine is commonly known as adrenaline. As a neurotransmitter and a hormone, it acts on nearly all types of body tissues and it is secreted by the medulla of the adrenal glands. Epinephrine plays role in regulating systemic vascular resistance and arterial pressure. Emotions such as anger and fear trigger the release of epinephrine into the bloodstream. This causes an increase in blood pressure, heart rate, and sugar metabolism which prepares the body for highly strenuous activities[64]. Increasing levels of epinephrine also has effects on airways; such as smooth muscle relaxation.[65]
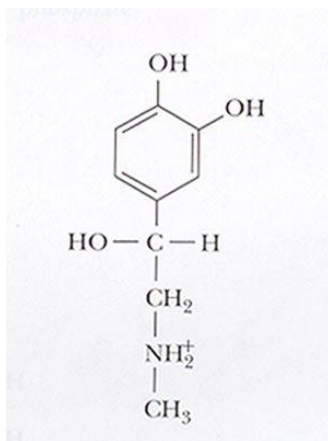
Epinephrine

As evident from the roles played by epinephrine in the human body, any dysfunction in uptake or release mechanism of epinephrine may lead to physiological disorders.

Dopamine (DA) and epinephrine (EP) belong to class of catecholamines that have short duration of action. When administered orally they are ineffective as they are rapidly

inactivated in the intestinal mucosa and the linear before they reach the systemic circulation. Dopamine is the precursor of epinephrine and structurally they are similar and often coexist in biological samples. Both of them have undergo electro-oxidation around same potential and therefore interfere with each other during their electrochemical detection. Hence there is a crucial need to detect and quantify them separately in real samples[66,67].

Electrochemical methods offer advantages such as miniaturization which enables rapid and in-situ detection of these neurotransmitters. This is extremely difficult to achieve using current methods to such as capillary electrophoresis,[68] high performance liquid chromatography-mass spectrometry,[69] and flow injection analysis with spectrophotometric detection.[70]

The purpose of this work is to demonstrate application of carbon IDEAs in selectively amplifying dopamine and epinephrine, coexisting in a solution under physiological pH, upon employing specific potentials. The method does not involve significant chemical pretreatment of electrodes other than electrochemical activating the electrodes through anodization in PBS pH 6.0 for less than a minute.

4.2.2 Materials and Experimental Methods

Materials

Analytical reagent grade dopamine hydrochloride and epinephrine(-) were purchased from Sigma Aldrich (MO, USA). Analytic grade oxalic acid dihydrate was purchased from Fisher (PA, USA). The materials for IDEA fabrication were purchased as described in Chapter 2.

Methods

Carbon IDEAs were fabricated as describe in Chapter2. The focus of this work is more on selectivity and hence shorter IDEAs with height of 0.3μm with width/gap ratio of 0.96 were used for this study (please refer Table 2 and 3 for exact dimensions).

CVs) and CAs were studied to determine the electrochemical separability of the neurotransmitters. CV (at 50mV/s) and CA experiments were carried out on an EDAQ system as described in Chapter 3, in a 1xPBS at neutral pH. The reference electrode was a pseudoreference of an Ag/AgCl ink droplet as described in Chapter 3. CV experiments were carried out in single and dual mode. For single mode runs, the collector circuit was kept open and the generator potential was swept between −300 and 600 mV. In dual mode, the generator potential was swept the same as in single mode but the collector was held constant at −300 mV vs. the reference electrode. During the CA experiments, the generator was kept at an oxidation potential of 600 mV and the collector was kept at −100mV for dopamine amplification. During epinephrine amplification, the generator was held at -50mV whereas the collector was kept at -300mV. After approximately half a minute of dual mode operation, the collector was disconnected to measure generator current in single mode.

All the experiments were conducted in stationary solution. To ensure very little evaporation of the solution during the duration of the experiment, the IDEA was enclosed in a PDMS channel as describe in Chapter 3. Oxalic acid was added to PBS solution prior to the addition of neurotransmitters to provide better stability during electrochemical measurements. Dopamine and epinephrine undergo spontaneous oxidative degradation at

non acidic pH. In the previous example of selectively amplifying dopamine, ascorbic acid acted as a stabilizer by acidifying the solution. However, adding ascorbic acid in this study will necessitate the use of SDS which will cause the reductive peaks dopamine and epinephrine to overlap; thus preventing selective dopamine amplification.[71] It has been observed[72] that oxalic acid prevents degradation of dopamine (upto 90%) in 24 hour incubation at room temperature. Moreover, oxalic acid doesn't interfere with electrochemical measurements as it is not electroactive, unlike ascorbic acid, at the potential range used in the study.

4.2.3 Results and Discussion

The cyclic voltammogram of 50μM dopamine is shown in Fig 27. The presence of oxalic acid has little effect on electroactivity of dopamine. The CV shows good electrochemical reversibility and presence of sharp oxidation peak at 300mV and reduction peak at 100mV. Successive cycles show negligible decrease in peak oxidation and reduction currents. The signal is amplified by operation in dual mode where the peak shaped CV gives way to steady state voltammogram with limited hysteresis as seen from Fig 28. The amplification is more than three times as typically observed in single mode and the collection efficiency is greater than90%. The amplification is lower as observed in Chapter 3 for similar carbon IDEA geometry. This is because the amplification also depends on the concentration of the analyte (50μM) which is much lower than the one used in the study in Chapter 3 (1mM). The dependency of amplification of the concentration will be discussed in more detail while discussing the limit of detection for this study.
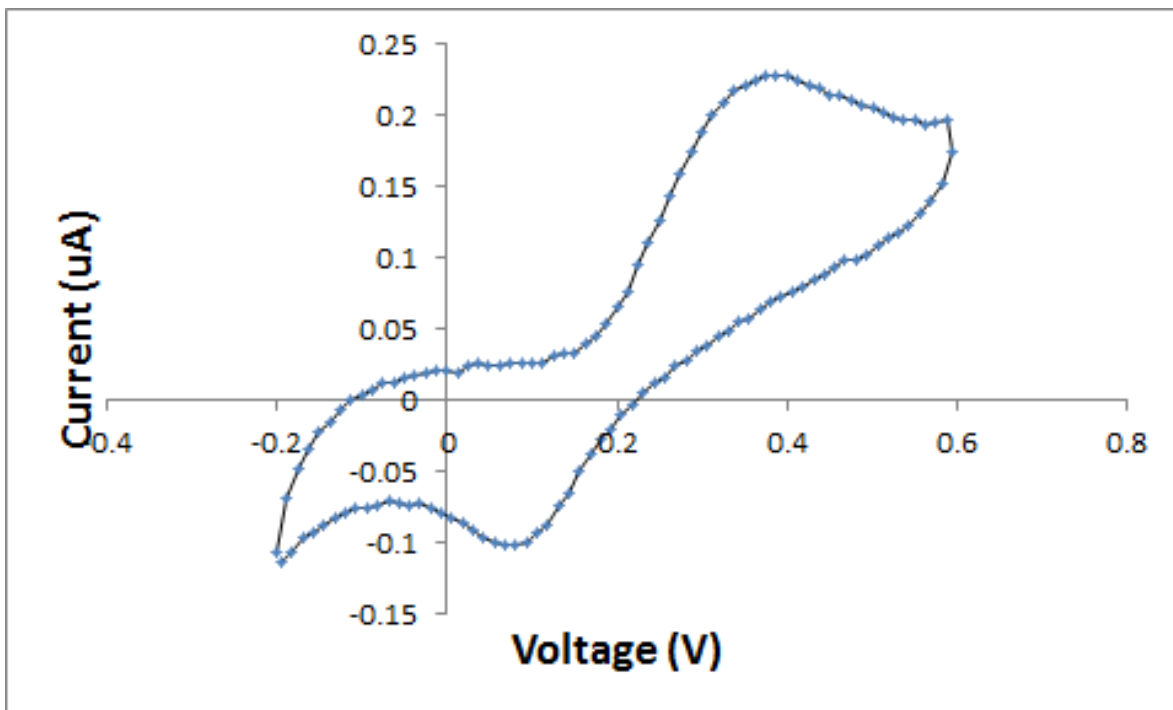
Figure 27: Single mode CV of 50μM Dopamine in 1X PBS containing 100μM Oxalic acid
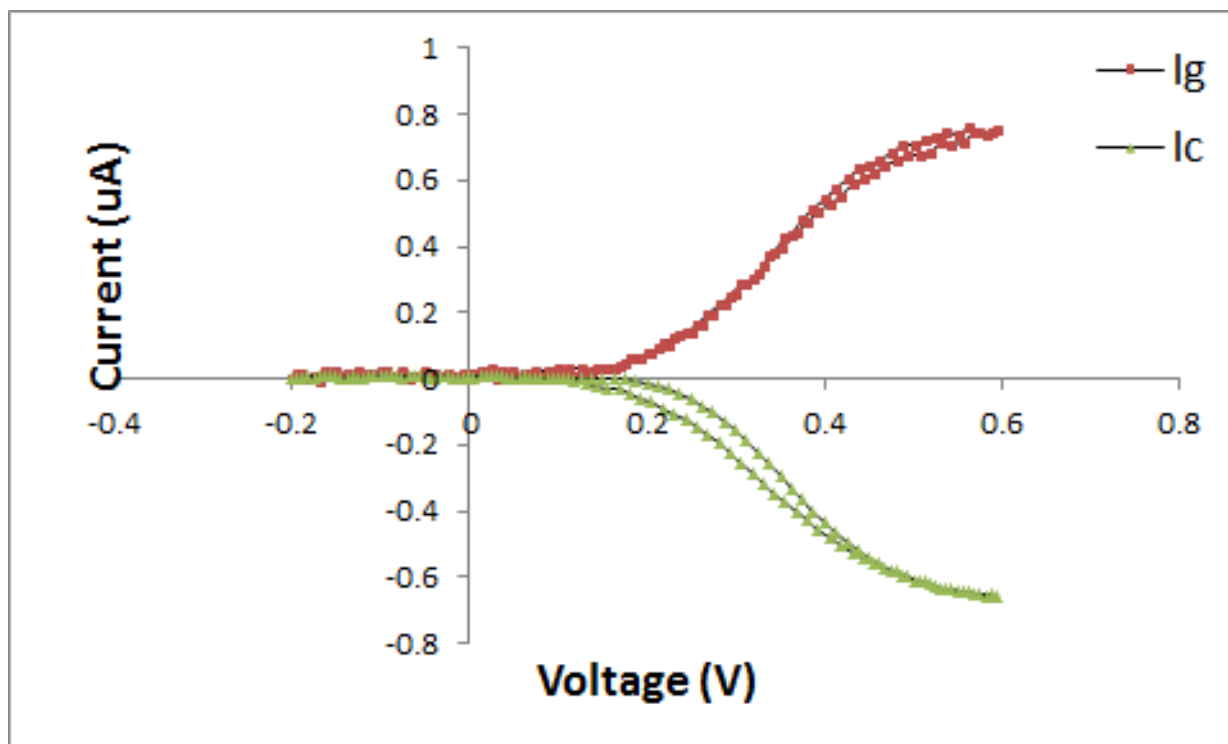
Figure28: Dual mode CV of 50μM Dopamine in 1X PBS containing 100μM Oxalic acid.

The redox behavior of epinephrine is not as straightforward as dopamine in neutral pH. The single mode CV of epinephrine at neutral pH shows an oxidation peak at 200mV, epinephrinequinone being the oxidation product of epinephrine, during the first anodic sweep. During the reverse scan, a reduction peak at −220mV is observed. If the cycling continues the one can observe another two oxidation peaks at −0.200 and 200mV on the second anodic sweep. As the number of cycle increases, the second oxidation peak continues to decrease whereas the first oxidation and reduction peaks continue to increase. As pH increases, the reduction of epinephrinequinone becomes increasingly difficult.
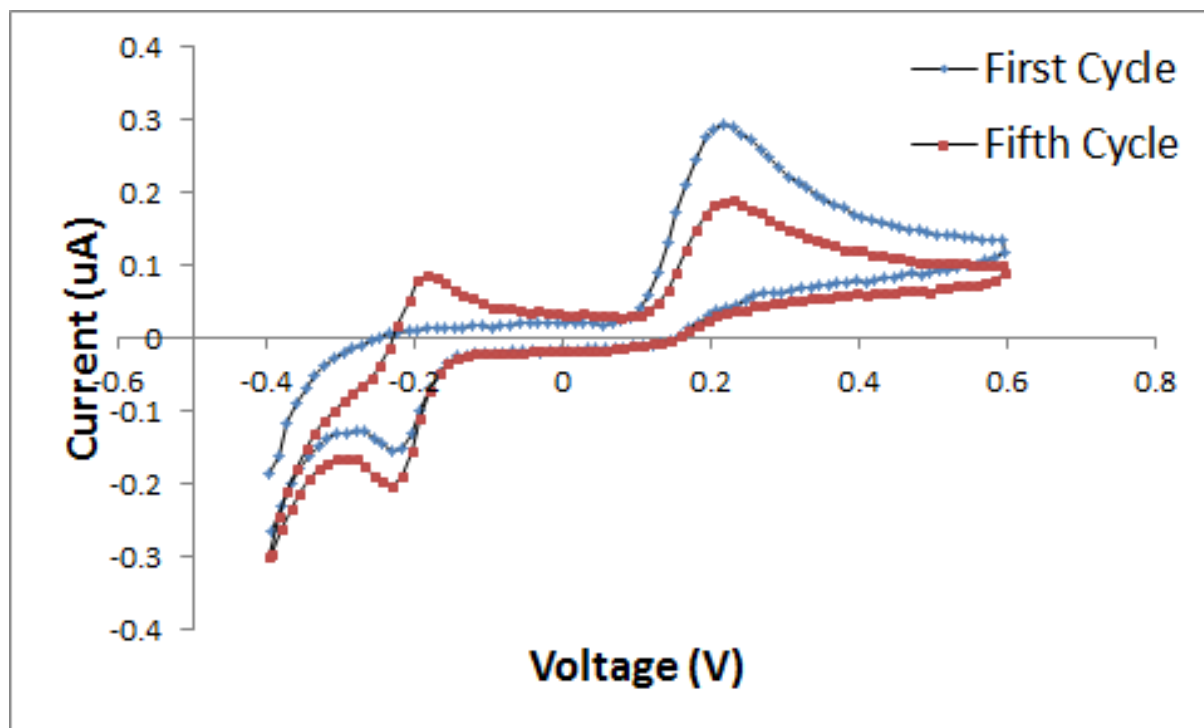
Figure 29: Single mode CV of 50µm Epinephrine showing multiple cycles in 1xPBS containing 100µM oxalic acid.

Epinephrine → **Epinephrinequinone**
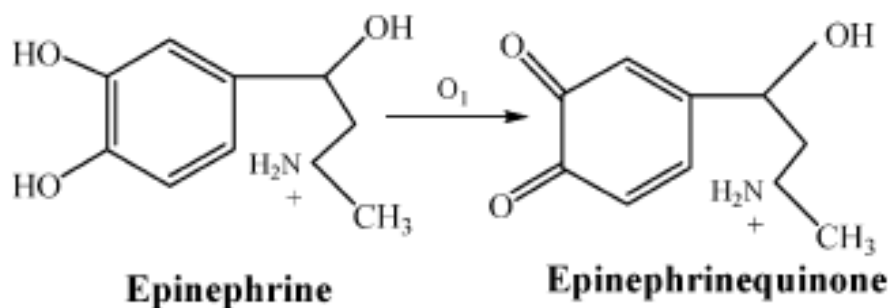
At neutral or higher pH, epinephrinequinone loses proton easily to reduce to adrenochrome. It is this adrenochrome which is further reduced, this time electrochemically, at -220mV to form leucoadrenochrome. During the second anodic sweep, the leucoadrenochrome is oxidized to adrenochrome at -200mV. Hence the adrenochrome and the leucoadrenochrome form a redox intermediate species which will be the basis of epinephrine quantification via carbon IDEAs. A potential applied specifically beyond -200mV at the generator and below -220mV at the collector will selectively amplify the redox intermediates. However, a full scan along the entire potential window between 600mV and -300mV needs to be applied first in order to generate the redox intermediate species for epinephrine detection.[73]

The dual mode CV shows the presence of the intermediate couple at lower potential range. The first scan of the CV shows similar behavior as the dopamine but one can observe a distinct hysteresis at the first scan during reduction sweep due to the formation of leucoadrenochrome. With increasing time/increasing number of cycles one can observe increasing concentration of the reaction intermediate species (evident during the fifth cycle).

Adrenochrome ⇌ Leucoadrenochrome
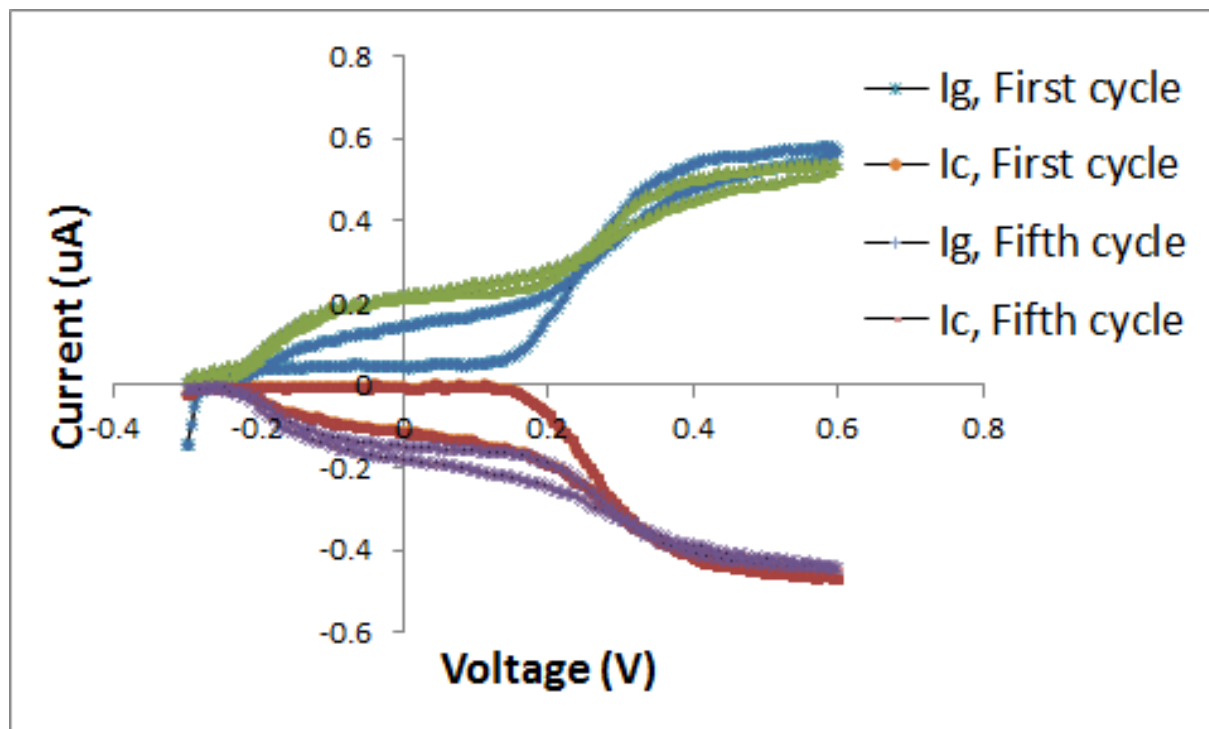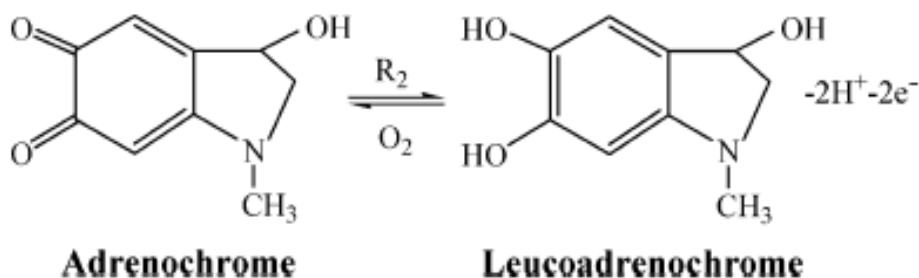
Figure 30: Dual mode CV of 50μM Epinephrine showing multiple cycles in 1X PBS containing 100μM oxalic acid

The dual mode CV of mixture containing 50μM dopamine and 50μM epinephrine is shown in Fig 31. The CV shows similar double sigmoid profile as the one seen in dual mode CV for epinephrine. However, the currents roughly look like the summation of currents as seen in Fig 28 and Fig 30. This goes to show that at wider potential window between 600mV and -30mV one can observe redox cycling of both redox couples i.e., dopamine and dopaminequinone as well as adrenochrome and leucoadrenochrome for epinephrine. To

selectively amplify either dopamine or epinephrine, appropriate potential range must be applied.
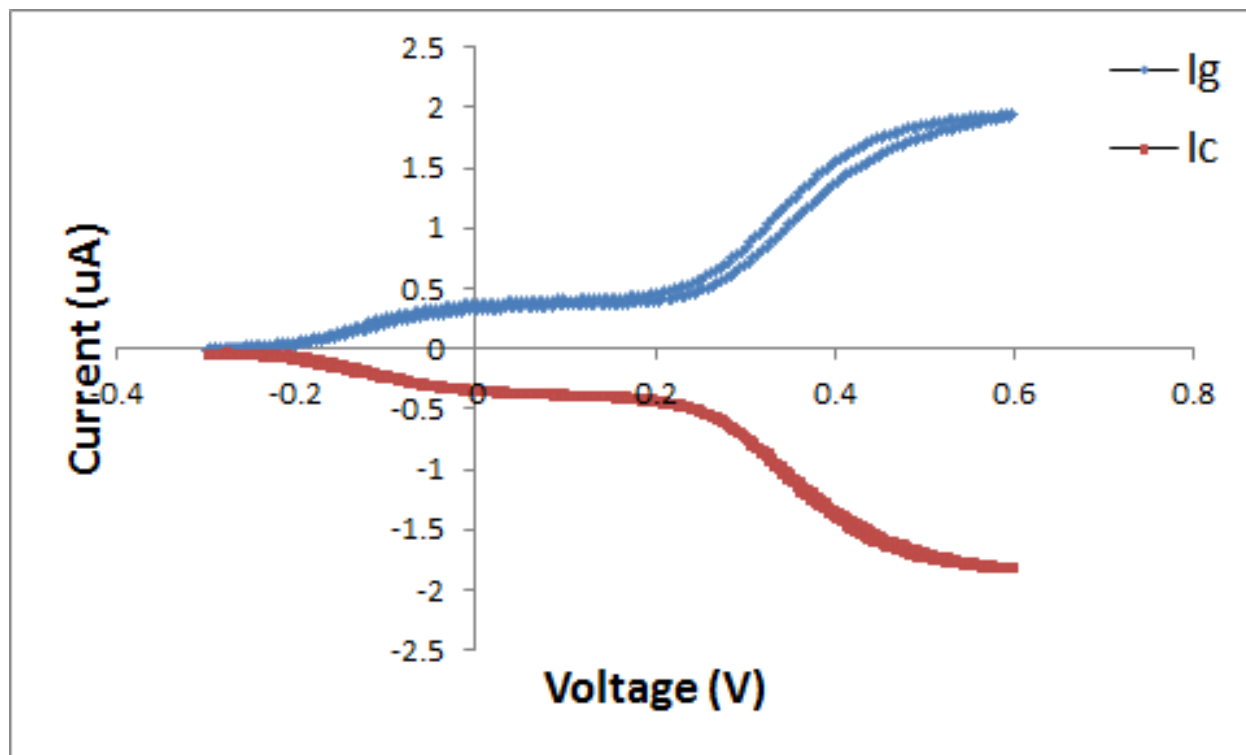
Figure 31: Dual mode CV of 50μM Dopamine and Epinephrine mixture in 1X PBS containing 100μM oxalic acid

Selective Amplification Strategy

As seen in Figure 32, if a full potential range between 600 and -300mV is applied one can see onset of oxidation of dopamine to dopaminequinone and epinephrine to epinephrinequinone when the generator electrode first reaches 200mV. During the reverse

cycle, onset of reduction of dopaminequinone to dopamine takes place first at voltage slightly lower than 200mV and this reduction continues at lower potentials till the reaction becomes diffusion limited. The onset of reduction of adrenochrome to leucoadrenochrome doesn't take place until the potential is reduced to -220mV or below.
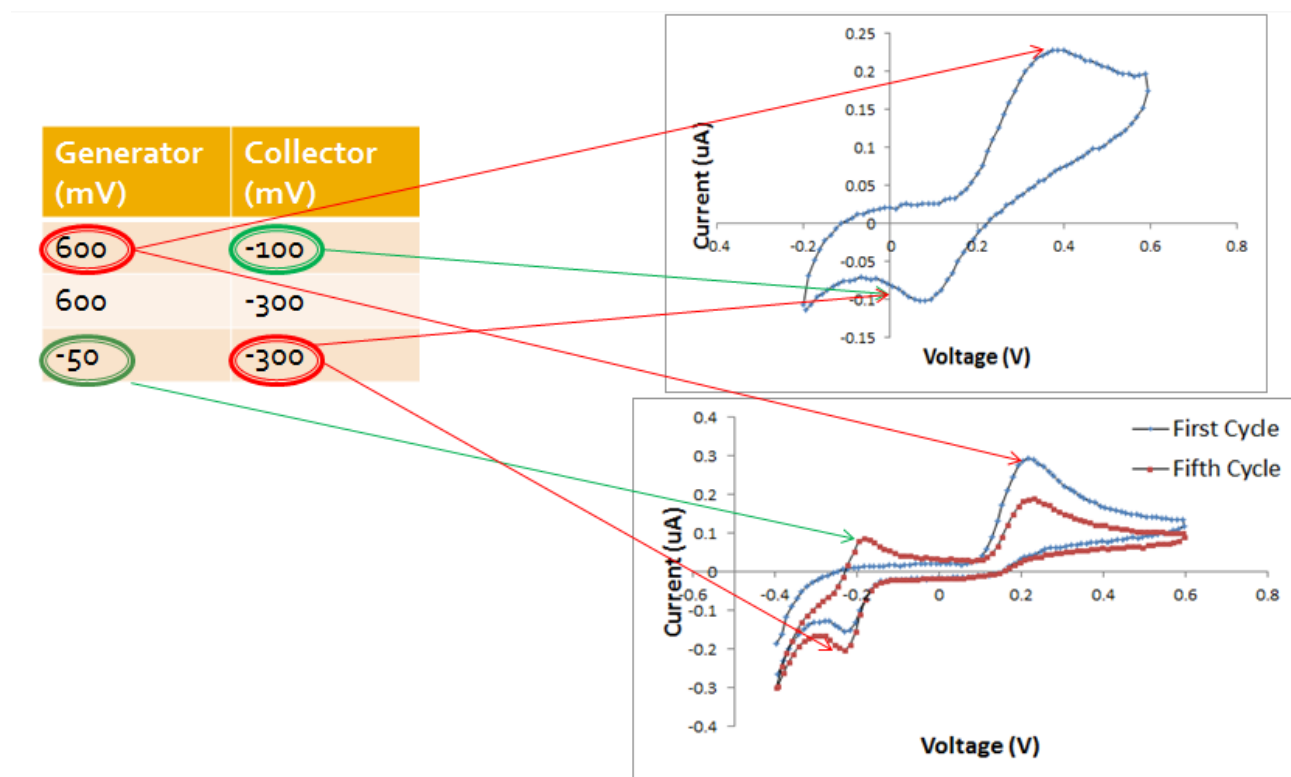
Figure 32: Schematic of selective amplification strategy of dopamine and epinephrine in their mixture. Dopamine is quantified first by measuring reduction current at -100mV. This step is followed by full potential range step for one minute to generate redox intermediates for epinephrine. Finally epinephrine is quantified by measuring oxidation current at -50mV

Hence if a potential is applied between 600mV and -100mV, one will observe participation of only dopamine/dopaminequinone redox couple. Ideally one could measure either the generator current or the collector current for dopamine quantification but there will be slight interference of epinephrine oxidation at the generator especially during first anodic

sweep of a CV or first few seconds in a chronoamperogram. For accurate dopamine quantification in the mixture, collector current should be used in the 600mV, -100mV potential range as there will be no interference from epinephrine.
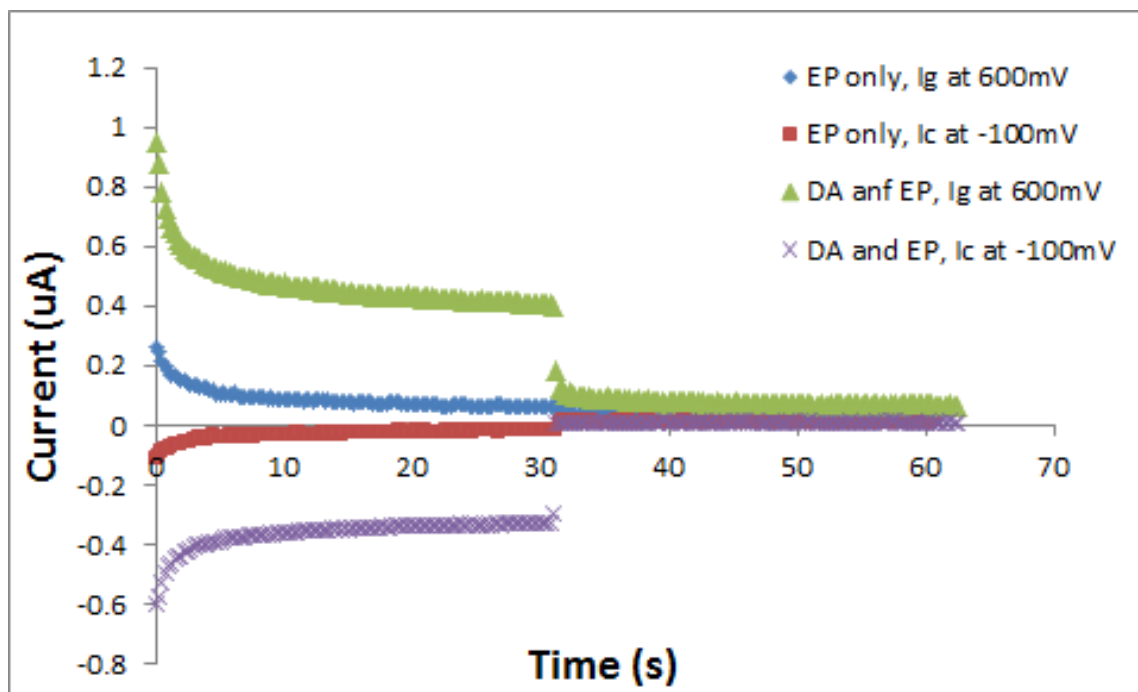
Figure 33: CAs of 50μM EP and mixture of EP and DA (50μM each) in 1XPBS containing 100μM OA

The Fig.33 displays chronoamperogram (CA) showing both the oxidation and the reduction currents at different conditions. During the first 30 seconds the CA was carried out in dual mode, thereafter the operation was carried out in single mode to observe amplification. At the beginning only 50μM of EP was present in the solution and CA was recorded to get the background current. The collector current (red curve) is almost zero in this case which the true background is. This shows absence of any adrenochrome reduction. Some generator current (blue curve) is observed which indicates the oxidation of EP to EPQ. On addition of 50μM DA one can observe significant increase in collector (purple curve) and the generator

current. One can use collector current directly to quantify DA in this case or subtract the generator current (green minus blue curve) to quantify DA indirectly.
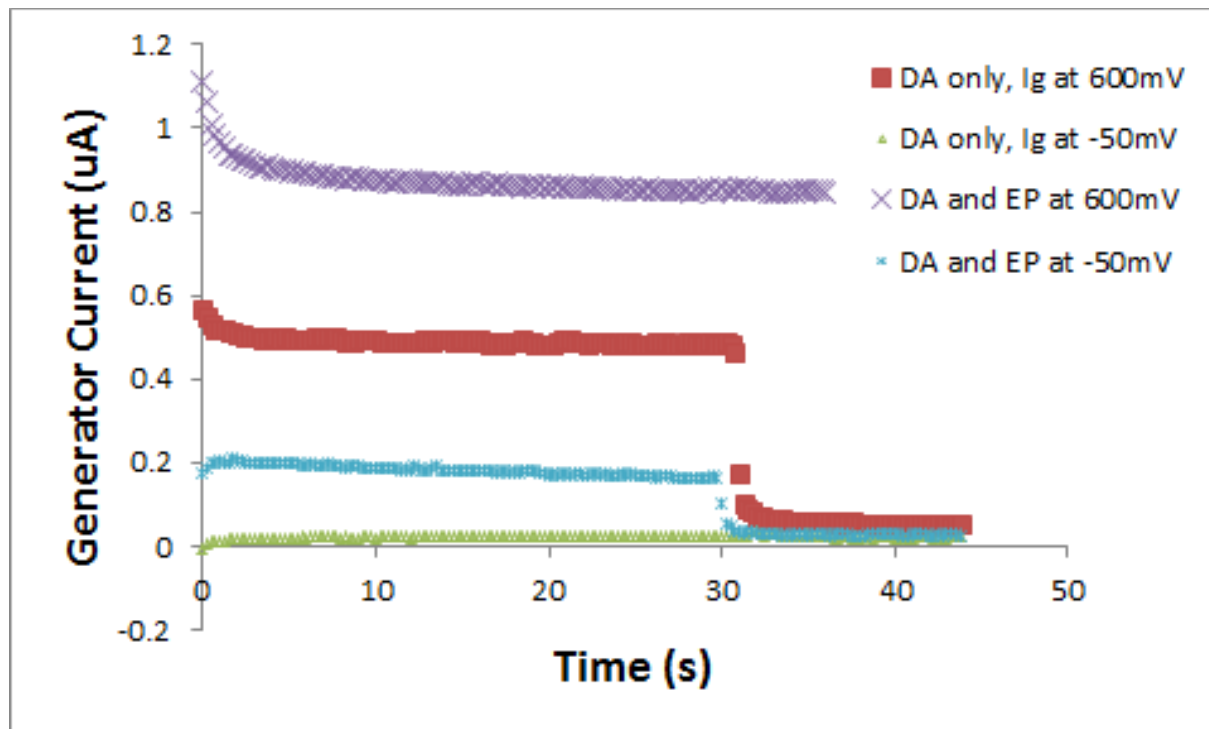
Figure 34: CAs of 50μM DA and mixture of EP and DA (50μM each) in 1XPBS containing 100μM OA

EP quantification is not as straightforward as DA. The oxidation product of EP, i.e., EPQ is unstable at neutral pH and undergoes spontaneous conversion into adrenochrome which is reduced to leucoadrenochrome around -220mV. However at this potential the collector electrode will also record reduction of DAQ to DA. To avoid interference from DA one can record the generator current beyond -200mV during the next anodic sweep. The generator current needs to be recorded before the onset of dopamine oxidation though. Hence the EP detection strategy involves a potential (regenerating) step where the generator and

collector is held at 600 and -300mV respectively for a minute allow generation of adrenochrome and leucoadrenochrome followed by amplification of the species by applying -50mV and -300mV at the generator and the collector respectively. To get reproducible results one has to keep the time for the regeneration step to be constant.

At the beginning only 50μM of DA was present in the solution and CA was recorded to get the background current. The generator current (green curve) is almost zero in this case which the true background is. This shows that there is absolutely no oxidation of dopamine at -50mV even after the regeneration step at full potential range between 600 and -300mV. Thereafter, 50μM of EP was added to the solution and the regeneration step at full potential range was applied for a minute. This was followed by recording generator current at -50mV. This generator current now shows the oxidation of leucoadrenochrome, a marker for EP. By keeping the time period for regeneration step constant one can selectively quantify EP in its mixture with DA.

Detection Limit

Detection limit and linearity of dopamine and epinephrine detection using carbon IDEAs were computed by testing out dual mode current for both the neurotransmitters at different concentrations. The IDEAs were first electrochemically cleaned to remove top passive layer for few seconds up to a minute. This was followed by measuring dual mode background current in 100μM oxalic acid in 1XPBS. Starting with the introduction of lowest concentration of neurotransmitter mixture, the concentration was increased after each measurement.
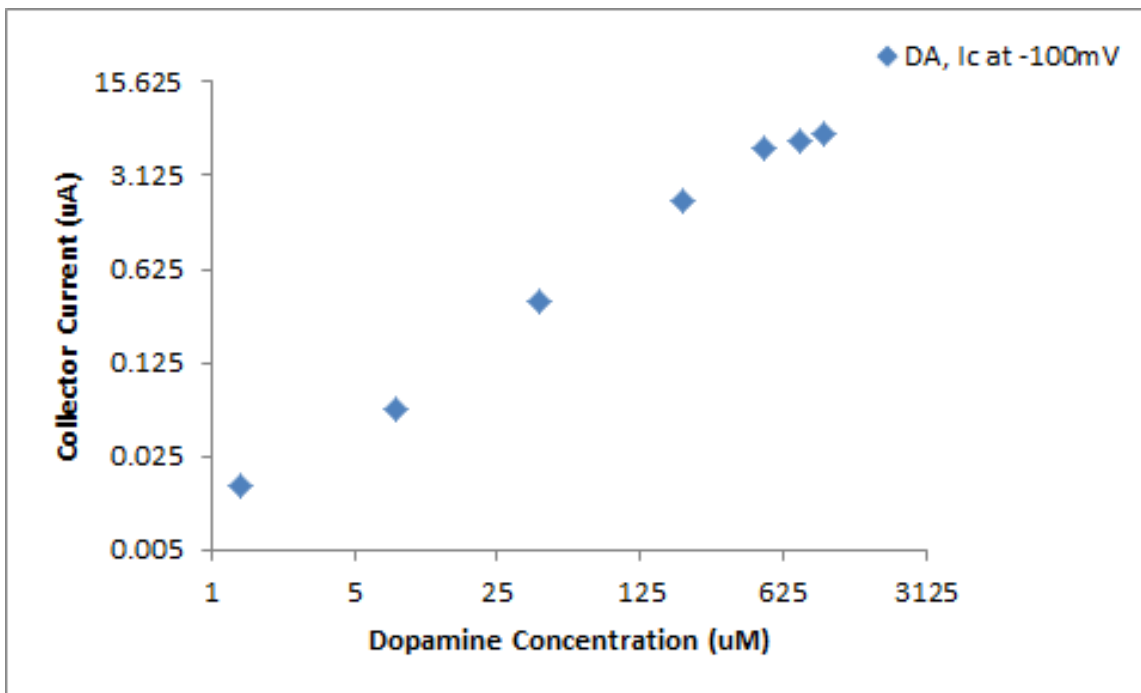
Figure 35: Dynamic range for dopamine in its 1:1 mixture with epinephrine in 1XPBS (pH 7.0) as detected by carbon IDEAs

Fig. 35 shows dual mode collector current at different concentrations of the mixture. The current was measured as the average for first 30 seconds. The background current in this case 5nA and the sensitivity is 10.42nA/μM with linearity over two orders of magnitude. Using 3*noise/sensitivity, we get detection limit of 1.44μM for dopamine in the presence of epinephrine at the same concentration.

Fig. 36 below shows dual mode generator current at -50mV for different concentrations of the mixture. The current was measured as the average for first 30 seconds. The background current in this case again 5nA and the sensitivity is 2.35nA/μM with linearity slightly under two orders of magnitude. The background current is also dependent on the detection

electronics. The EDAQ/Quadstat system has the lowest resolution of around 1- 5nA. Using

3*noise/sensitivity, we get detection limit of 6.38μM for epinephrine in the presence of

dopamine at the same concentration. At concentrations greater than 200μM of epinephrine

we observed a drop in oxidation of leucoadrenochrome which can be attributed to

passivation of the IDEA surface at higher concentrations. The passivation reduces the rate

of electron transfer thus reducing the oxidation current.
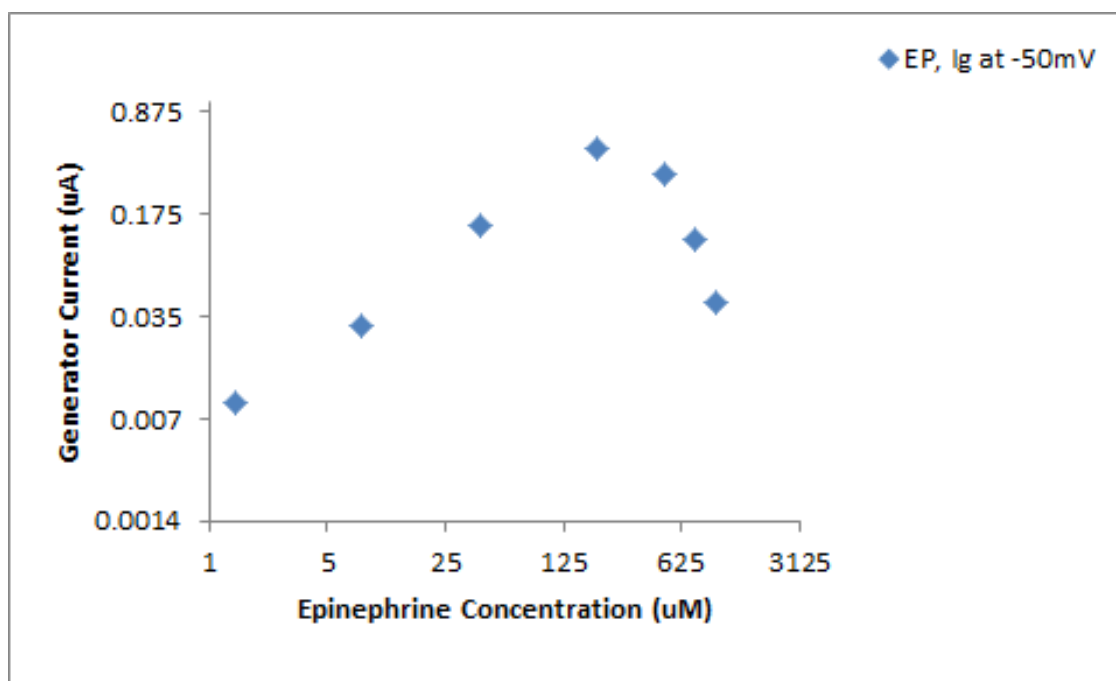
Figure 36: Dynamic range for epinephrine in its 1:1 mixture with dopamine in 1XPBS (pH 7.0) as detected by carbon IDEAs

Fig 37 gives the idea of how well the dopamine and epinephrine are oxidized effectively by

the carbon IDEAs. Here, the red dots correspond to the generator current measured at

600mV for the mixture at different concentrations at full potential range i.e, when collector

was held at -300mV. At 600mV we should ideally observe the oxidation of DA to DAQ and

EP to EPQ which is exactly the case. The blue dots corresponds to the summation of the generator current for dopamine only sample at 600mV and the epinephrine only sample at -50mV which indicates that the performance of IDEAs are identical for each neurotransmitters individually or in their mixture.
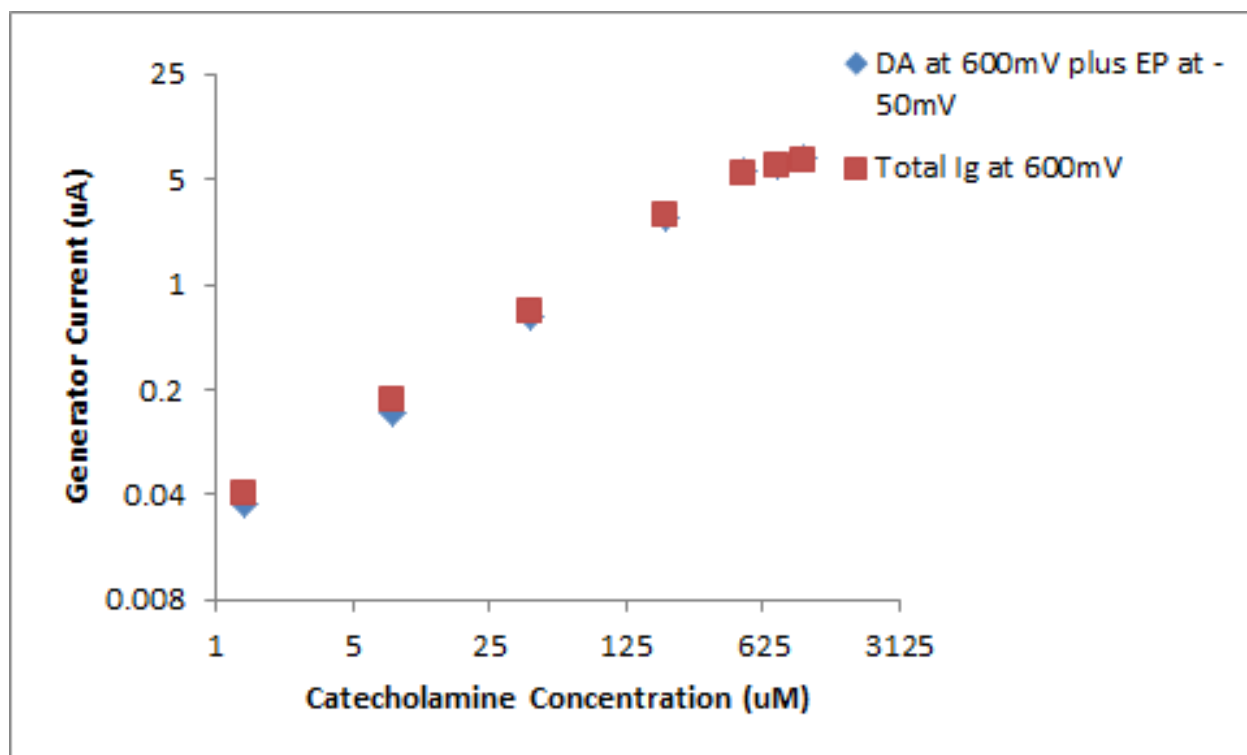
Figure 37: Dynamic range of the catecholamine concentration in their mixture in 1XPBS

5. Carbon IDEAs in Electrochemical ImmunoAssay

5.1 Background and Motivation

An Immunoassay is a biochemical test that measures the concentration of an analyte/antigen upon reaction with its antibody in a biological fluid, such as blood, serum, saliva, sweat, urine etc. Usually immunoassays employ labels such as enzymes,[74] radioactive isotopes,[75] DNA reporters,[76] fluorogenic reporters[77] or use of metal atoms in the form of their organometallic or co-ordination complexes.[78] The point of care devices that use immunoassays should be specific, easy to use, robust, portable and inexpensive, fast and should be able to work with low volume and turbid samples. The electrochemical immunoassay that employs electroactive labels or electroactive enzyme products has the capability to satisfy all the stated conditions.

Sensitive immunoassays for detection of biomarkers for disease diagnosis and of toxins/biological warfare agents to combat bioterrorism threat have been of great importance in recent years.[34,79] Electrochemical immunoassays can be direct or indirect. In direct electrochemical immunoassay, direct antigen-antibody binding can yield changes in charge densities that can be measured and do not require any side reaction. Essentially these are label free immunoassays.[80,81,82,83]

Indirect electrochemical immunoassays require labels to generate side reaction that is in direct proportion to the antigen-antibody binding. The labeling redox compound should be stable in buffer and should not cause electrode fouling.[84]

Electrochemical immunoassays utilizing recycling of redox species have been successfully explored in the past [34,79,85]. These are some of the examples of indirect electrochemical (amperometric) immunoassays. Carbon IDEAs can be effectively used to enhance

sensitivity using redox amplification of electroactive substrates. A proper choice of enzyme substrate combination is extremely important in such as case. The enzyme substrate is converted into a product which is redox active. This conversion takes place at the detection antibody that is labeled with the enzyme. This product will be oxidized or reduced at first working electrode array and the counter reaction will take at the second working electrode array. It is essential that the enzyme product is not converted back into the substrate by IDEAs which will result in false positive amplified signal. Some of the enzyme substrates combinations that can be used with IDEAs are listed in the Table 4.

Table 4: Enzyme substrates combinations that work with IDEAs

Enzymes	Substrates	Comments	Reference
Horseradish Peroxidase	o-Phenylenediamine (optical and electrochemical)	HRP catalyzes conversion of oPD into DAP (2,3-Diaminohenazine) which can be used with IDEAs	[86,87]
Horseradish Peroxidase	3,3',5,5'-Tetramethylbenzidine (optical and electrochemical)	HRP catalyzes oxidation of TMB into 3,3',5,5'-tetramethylbenzidine diimine. The reaction is highly reversible (goes back to TMB) and can work only using single working electrode configuration.	[88]
Horseradish Peroxidase	p-Aminophenol (electrochemical)	HRP oxidizes pAP into 3,4-di-[(4-hydroxyphenyl)amino]-6-[(4-hydroxyphenyl)imino]-2,4-cyclohexadiene-1-one which is highly reversible and can be used with IDEAs	[89]

Horseradish Peroxidase	Amplex red (10-acetyl-3,7-dihydroxyphenoxazine) from Life technologies	HRP catalyzes conversion of Amplex red into resorufin which can be detected by IDEAs. Between IDEAs it can be detected either as resorufin or dihydroresorufin.	90
β-galactosidase	p-aminophenyl-β-D-galactopyranoside (pAPG) (electrochemical)	β- gal catalyzes conversion of pAPG into p-Aminphenol (pAP) which is redox active and detectable by IDEAs	79
Alkaline Phosphatase	p-Aminophenyl phosphate (pAPP) (electrochemical)	ALP dephosphorylates pAPP into pAP which is redox active and detectable by IDEAs	91,92
Alkaline Phosphatase	p-Nitrophenyl phosphate (pNPP) (optical and electrochemical)	ALP dephosphorylates pNPP into pNP which undergoes irreversible oxidation and hence can only be used using a single working electrode.	93

In such a detection system the carbon IDEAs need not be functionalized. One can simply perform immunoassay in a microfluidic chamber that is in close proximity to the detection chamber where the IDEAs will be housed. Once the immunoassay reaction is completed, the product can be flown over to the IDEAs where the detection via redox cycling will take place in a stationary sample condition. This way electrode fouling can be minimized. The detection scheme can be used for detection various biological analytes using the same enzyme substrate combination.

5.2 Selection of Optimal Enzyme and Substrate Combination

The enzyme-conjugated antibodies along with the standard and other reagents for immunoassay such as assay diluent, phosphate buffered saline, TMB, oPD, DAP, and pAPP were provided by CerMed Corp. (Sunnyvale, CA). The pAP, sulfuric acid (for stopping enzyme reaction), and Tween20 (for washing step) were purchased by the UCI team from Sigma Aldrich.

The first experimental step (Step 1) is to confirm that carbon IDEAs could be used for the detection of the redox amplified signals generated by DAP and pAP (enzyme products). After successful completion of this step, (Step 2) known concentration of enzyme-conjugated antibodies were immobilized onto microtiter plates followed by addition of their respective substrates. Aliquots of from each reaction well, containing different ratios of substrate/products, were taken for electrochemical testing. This allowed the testing of an added level of complexity, demonstrating that the products of enzyme activity would be detected without any interference by the enzymes themselves or the substrates.

The next level of complexity, Step 3, was evaluated in the form of a complete sandwich immunoassay detecting the standard at different concentrations. This final level demonstrated that electrochemical testing could be carried out in the presence of the standard, generating dose-response curves. Optical density measurements were also taken to generate additional dose-response curves for comparison to those from electrochemical measurements.

5.2.1 Detection scheme using ALP and p-Aminophenol and Initial experiments (Step1)

As explained earlier, the enzyme substrate itself should be minimally electroactive whereas the product should exhibit excellent electrochemical properties such as low redox potential, negligible electrode fouling, reversible electrochemical behavior and the fact that the product should not reconvert back to the substrate itself. Keeping these constraints in mind, following general detection scheme had been developed and used by different groups.
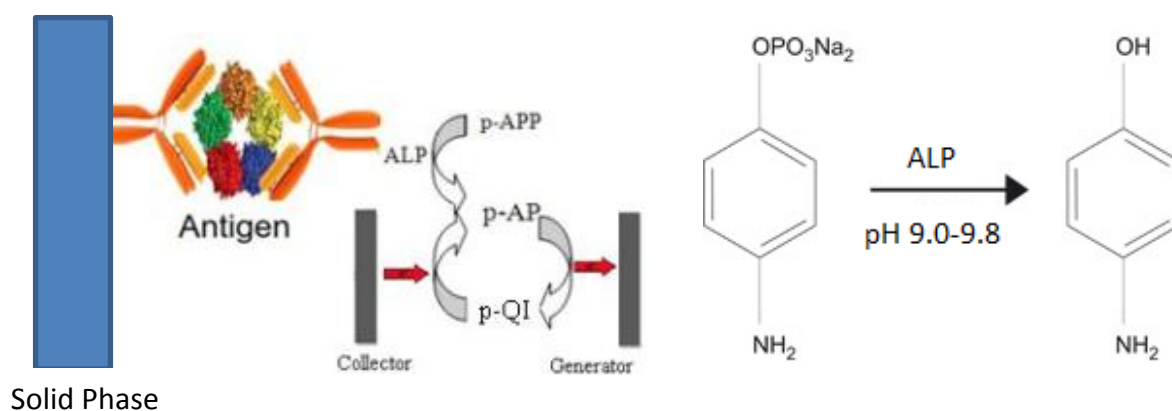
Figure 38: Detection Scheme using Alkaline Phosphatase and p-Aminophenyl Phosphate

Most of the biologically analytes are not redox active and hence they cannot be used directly for electrochemical sensing. Using a sandwich immunoassay these analytes can be selectively captured and detected nonetheless using the strategy depicted in Figure 38. The general strategy to detect such analytes using sandwich immunoassay and carbon IDEAs is as follows: First an antibody (known as the capture antibody) is immobilized on a substrate i.e., solid phase. This step is then followed by the incubation with the antigen (the protein biomarker of interest). Next a second antibody (known as the detection antibody), tagged with an enzyme such as Alkaline Phosphatase (ALP), is incubated to react with the antigen

already bound to the first antibody. By introducing a known concentration of p-aminophenylphosphate (p-APP), a substrate for ALP, the ALP starts catalyzing the conversion of p-APP to electroactive p-aminophenol (p-AP). The reaction product can can be transferred to a separate detection chamber housing the carbon IDEAs where only the p-AP, in the mixture of p-AP and p-APP, is oxidized to p-quinoneimine (p-QI) form by applying the appropriate potential to the generator electrode of the IDA. p-QI can be reduced back to p-AP form at the collector which is at appropriate lower potential initiating redox cycling. The advantage of this strategy is that p-AP will not be converted back to its original form p-APP at IDA and hence there will be no false positive detection. p-AP and p-QI are electrochemically reversible and the current signal so obtained will be indirectly but linearly proportional to the concentration of the target analyte captured in the sandwich immunoassay.

The above strategy was employed by Niwa *et al.*[94] using gold coplanar IDAs in conjunction with sandwich immunoassay of mouse IgG. They were able to achieve linearity range of 10-1000ng/mL and detection limit of 10ng/mL. Yasukawa *et al.*[79] used a similar strategy with a slight variation where the detection antibody was conjugated with β-galactosidase which catalyzed the conversion of substrate p-aminophenyl-β-D-galactopyranoside into p-AP. The p-AP was later detected using coplanar carbon IDA (purchased from BAS Inc). By employing carcinoembryonic antigen as a biomarker they were able to demonstrate detection limit as low as 0.01ng/mL with linearity of over two orders of magnitude. Similar strategies using p-AP as redox probe can be found in the literature.[95]

Testing the electrochemical behavior of pAP with carbon IDEAs

The first task to develop electrochemical immunoassay was to optimize the redox behavior of pAP using carbon MEMS derived electrodes. For preliminary testing we used 10mM pAP (purchased from Sigma Aldrich) in 1X Tris Buffered Saline (9.2pH). Initial experiments were carried on flat carbon electrodes as shown in the figure.
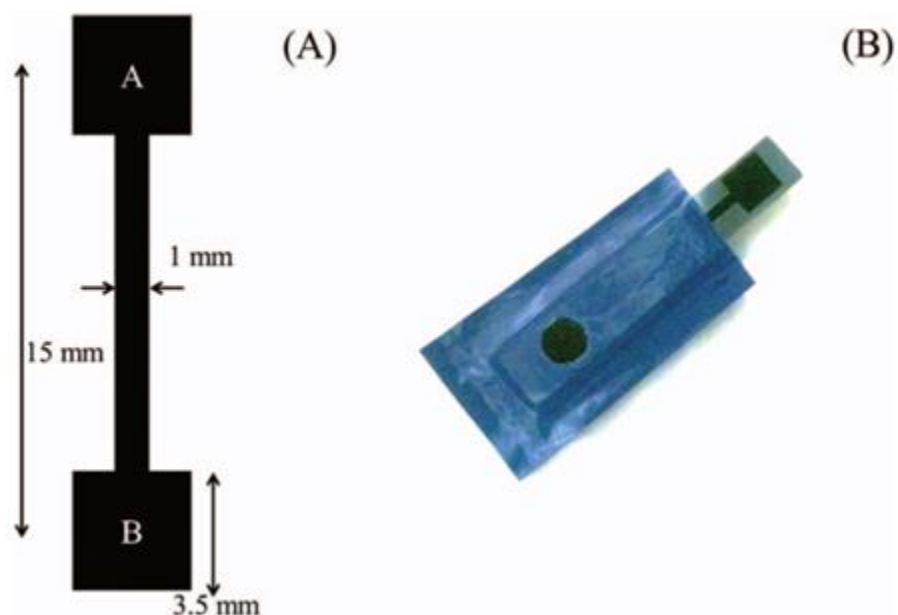
Figure 39: a) Schematic diagram of the electrode design b) Photograph of an electrode insulated by Monokote tape

These flat electrodes were preferred over IDEAs for initial experiments because: 1) They are made using similar carbon MEMS process as carbon IDEAs so they have similar electrochemical properties i.e., presence of redox peaks and reversibility. 2) They are much easier to fabricate, they give higher yield per wafer and therefore are available in plenty. 3) It makes sense to first optimize electrochemical properties as stated in 1 and then on to using immunoassay which is more tedious and involves use of expensive reagents.

In these set of experiments, electrodes T3, T5 and T7 were electrochemically activated in 1X PBS 6.0 pH solution. All the flat electrodes had the same geometric area but they were treated differently for electrochemical activation. The activation etches out an extremely thin (in nm range) passive layer and creates surface roughness. For T3, activation step involved carrying out cyclic voltammetry from 1.5 to 2V for 10 cycles.[96] For T5 and T7, the activation step involved applying a step potential of 1.8V for 20 and 300 seconds respectively. For T8 the electrodes were used for experiment without any electrochemical activation.
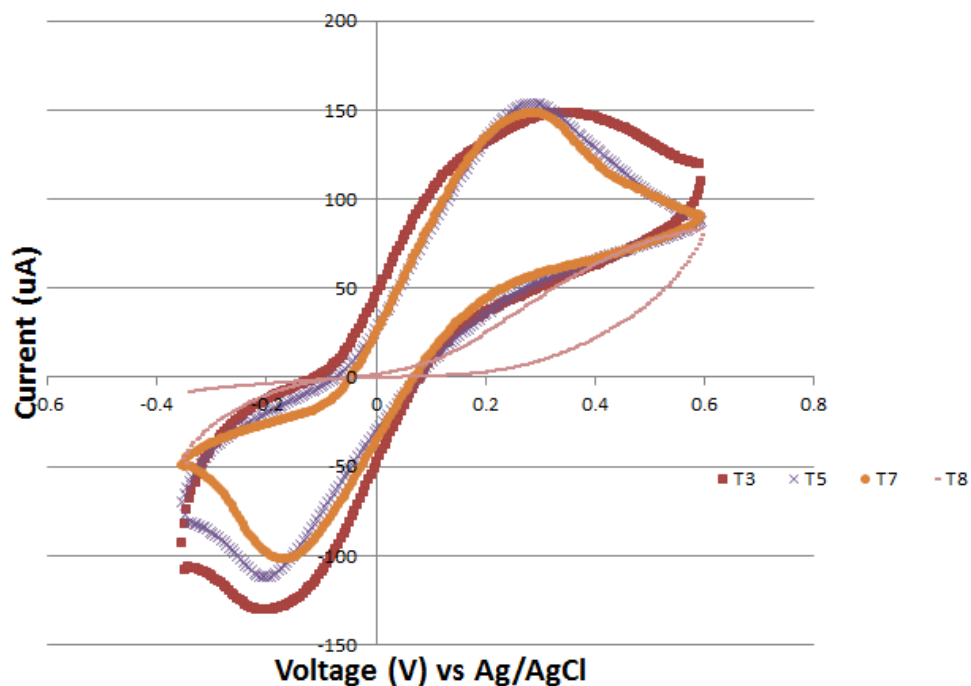
Figure 40: Cyclic voltammograms of flat electrodes after different surface activation processes
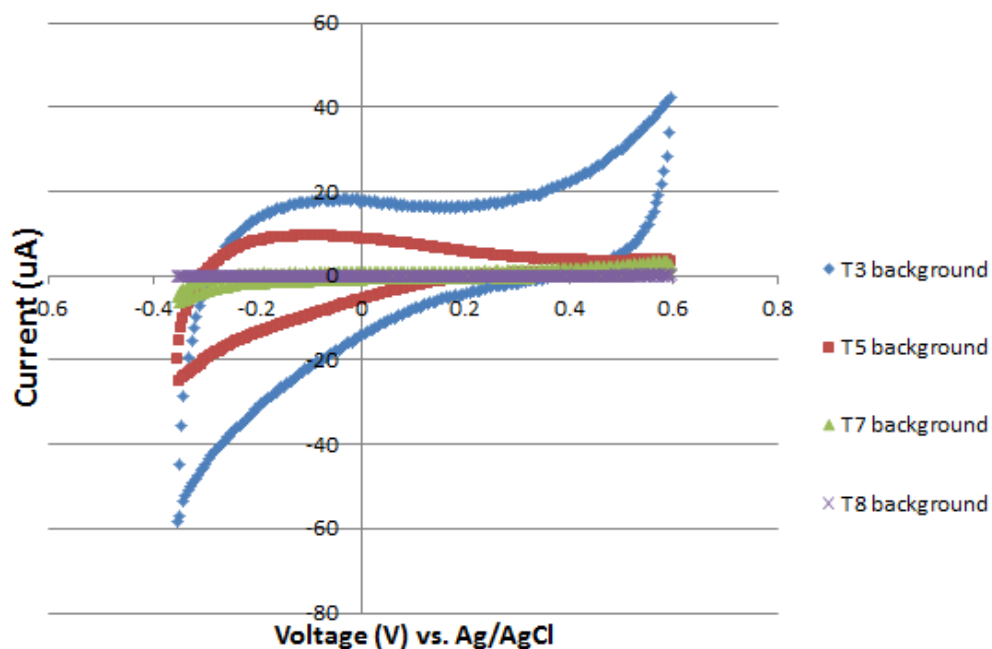
Figure 41: Background cyclic voltammograms of flat electrodes after different surface activation processes

As it can be seen from Fig 40 and Fig 41 above, T3 gives the best reduction to oxidation peak ratio but has the poorest background (charging current) and hence poor signal to noise ratio (SNR). T5 has the second best SNR, better signal but poorer background compared to T7. T7 gives the best SNR, lowest background amongst electrochemically activated electrodes. T8 gives lowest background which means that it has the most passive surface. T8 has a poor target signal, lacks prominent reduction peaks and shows continuous and significant decrease in peak current in successive cycles for 10 cycles.

Similar experiments were then carried out using carbon IDEAs with digit width of 2.7μm, gap of 1μm and height of 0.6μm. Target signal was observed using 1mM pAP in 1X TBS (9.2pH). For dual mode cyclic voltammetry experiments, the generator was scanned from -

0.2 to 0.6V vs. pseudo-reference and while the collector was held at constant -0.3V. In single mode, collector was kept open. For chronoamperometry experiments, the generator was set at 0.6V; collector was set at -0.3V vs. pseudo-reference in dual mode. After approximately 30s of dual mode operation, the collector was kept open to observe single mode generator current.
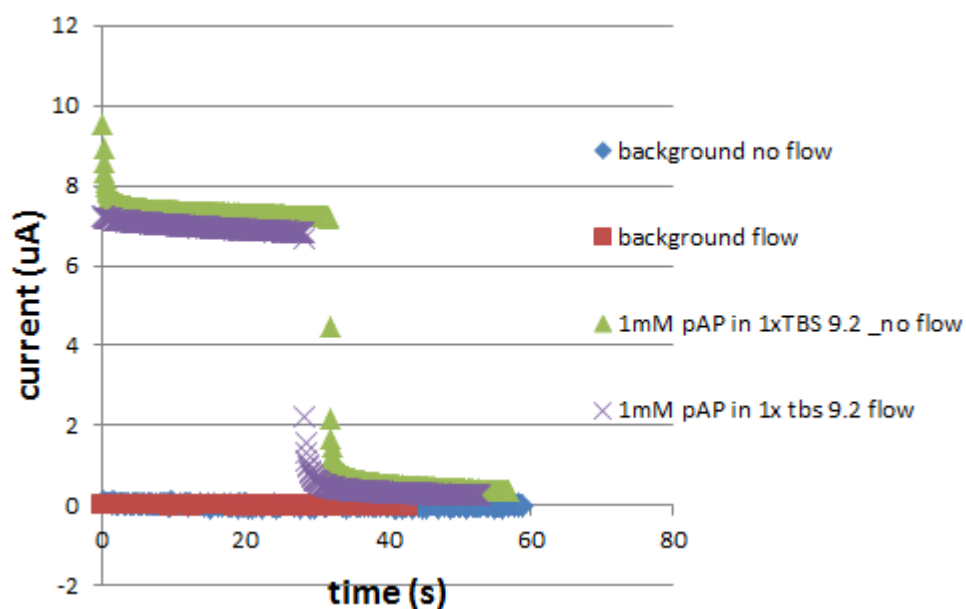
Figure 42: Chronoamperogram for 1mM pAP in 1X TBS 9.2pH. Dual mode operation for first 30 seconds followed by single mode using carbon IDEAs.
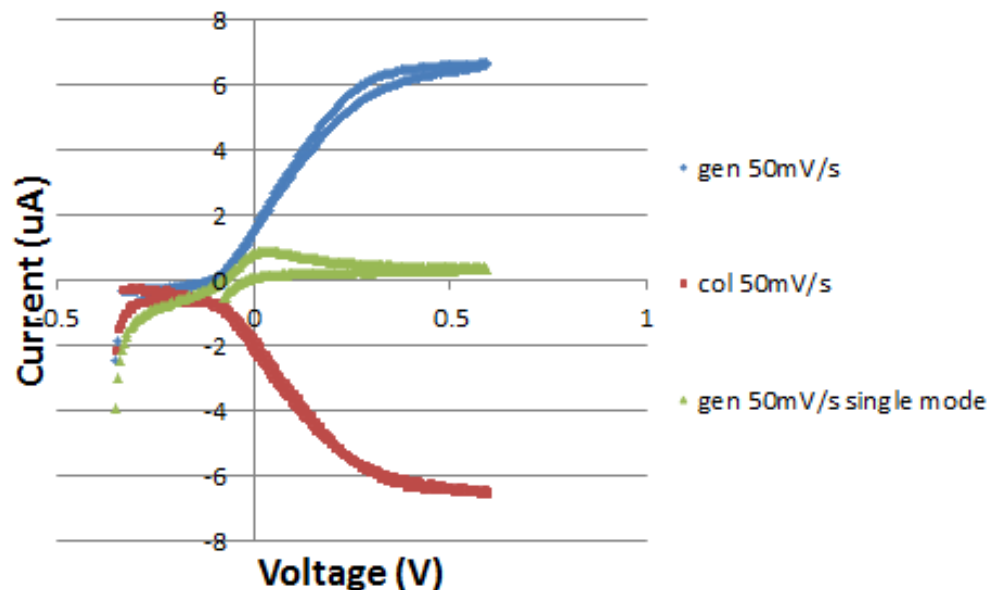
Figure 43: Cyclic voltammograms at 50mV/s potential sweep rate. Single mode generator current (green) and dual mode generator current (blue) and dual mode collector current (red) using carbon IDEAs

As it can be observed from Figure 42 and 43, the redox behavior of pAP is excellent at 1mM concentration in 9.2pH buffer solution. The redox amplification is as good as the one observed with standard redox probe such as Potassium Ferrocyanide in neutral buffer. However, there are practical issues in using pAP as a redox probe for electrochemical immunoassay. From our experiments we observed that pAP solution is highly unstable in the presence of oxygen. It undergoes oxidation easily in ambient conditions and it needs to be detected within few minutes especially at very low concentrations.

Even at a relatively high concentration of 1mM , the CVs showed a significant drop in peak currents with successive cycles as it can be observed in Fig 44 below.
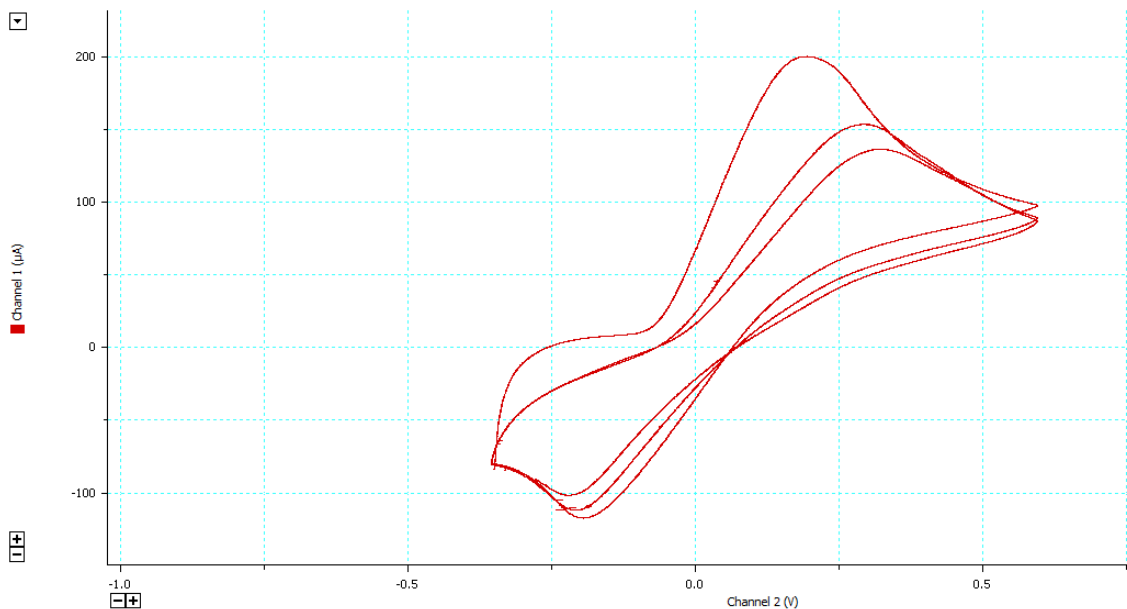
Figure 44: Successive cyclic voltammetry scans showing increase in peak to peak voltage for 1mM of pAP in 1X TBS, 9.2pH

In Figure 44 we have shown only three cycles but one can observe not only a significant drop in peak current but also see a shift in potential which is not an ideal redox probe. Because of these practical issues it was difficult to detect pAP lower than 10µm concentration. We observed a narrow linearity range of 10µm-2mM using our carbon IDEAs.
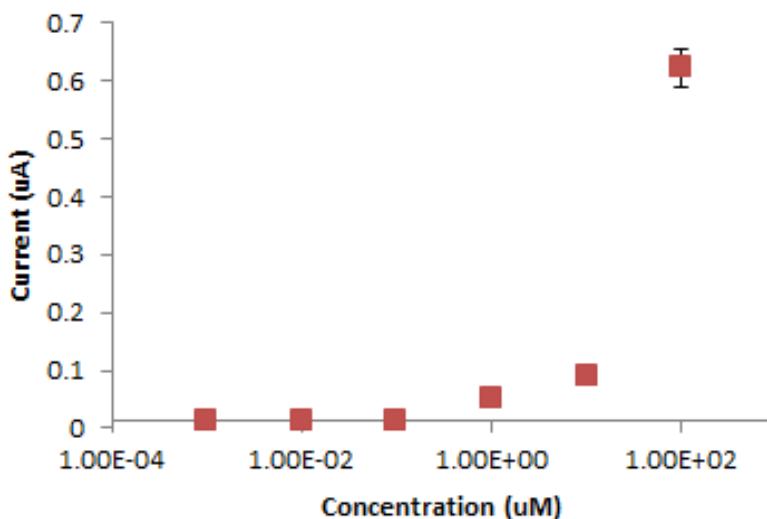
Figure 45: Dynamic range of pAP as tested in 1X TBS; 9.2pH using carbon IDEAs: width 2.7μm, gap: 1μm and 0.2μm height.

One another issue in using pAP as redox probe was its tendency to foul the electrodes.[97] At neutral or lower pH, pAP readily undergoes electrochemical oxidation to form p-quinoneimine which undergoes hydrolysis. Under neutral or acidic pH one can observe a reddish byproduct in the sample solution which can possibly contaminate electrode for further use. At higher pH of 9.2, this issue is more or less resolved. However, we still observe a continuous decrease in peak currents for multiple cycles of CV. This goes to show that even at higher pH there is still some adsorption of byproducts or the pAP itself onto the surface of the electrode; rendering it less sensitive for further use.

5.2.2 Detection scheme using HRP and 2,3 Diaminophenazine and Initial experiments

Our primary strategy to develop electrochemical immunoassay using carbon IDEAs was to use alkaline phosphatase as a label for detection antibody since it has been widely applied in conjunction with pAP for redox amplification. However, the detection scheme is riddled

with practical issues as explained before. The second detection scheme uses horseradish peroxidase (HRP) as enzyme label. HRP is smaller, more stable and less expensive compared to ALP. HRP also exhibits higher turnover rate compared to ALP which means that it can generate strong signals quicker compared to ALP.

o-phenylenediamine was chosen as electrochemical substrate for HRP to develop the electrochemical immunoassay. HRP catalyzes oxidation of OPD to 2,3-Diaminophenazine (DAP) in the presence of hydrogen peroxide. Upon application of specific potentials, the enzymatic product can be recycled between its redox states using carbon IDEAs without going back to its OPD form. The detection scheme using sandwich immunoassay is shown in Fig 46.
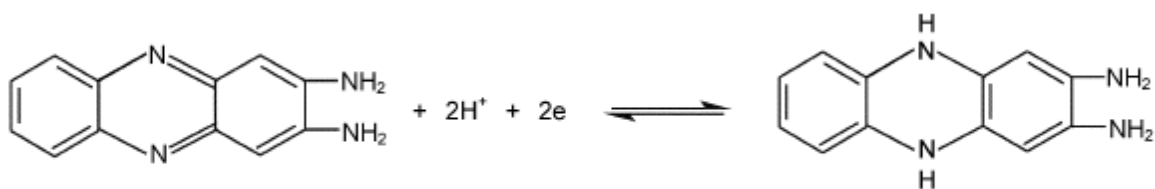
Redox behavior of DAP (left) and its reduced form.
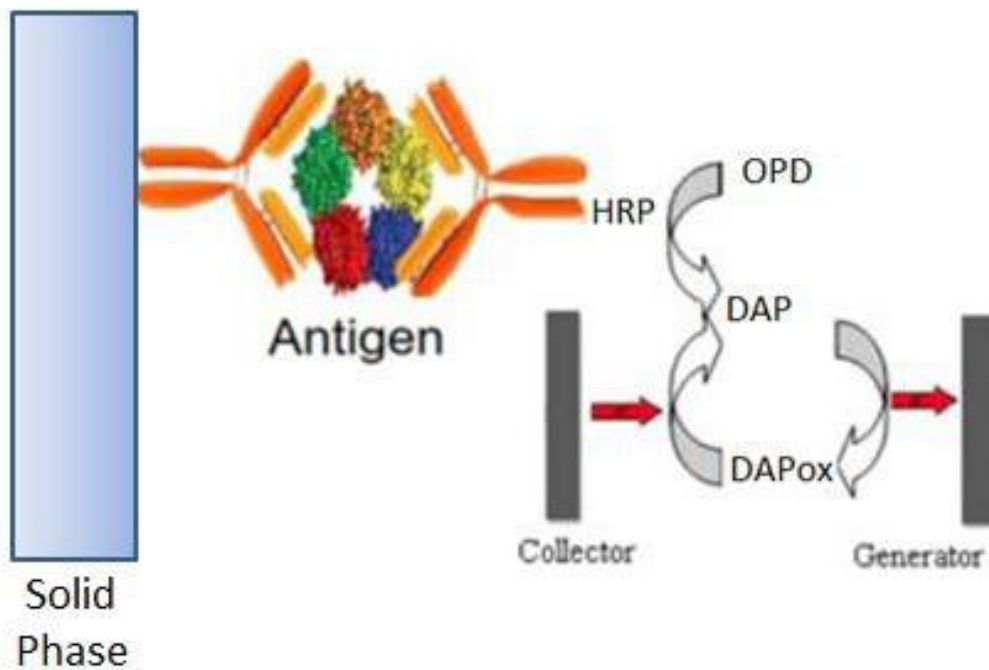
Figure 46: Detection Scheme using Horseradish Peroxidase and o-Phenylenediamine

To the best of our knowledge, the above detection scheme hasn't been reported yet. The only disadvantage with the scheme is that OPD is a suspected carcinogen and should be handled carefully.

Initial testing with flat electrodes

Since there is not much background literature on redox behavior DAP other than some references,[8687] we carried out some experiments using flat electrodes. 1mM DAP (obtained from Sigma Aldrich) in 1X TBS (adjusted to pH 7) was used to get target signal whereas the background was plain buffer. Experiments were also done to check if any kind of electrochemical activation was necessary to reliably detect DAP.
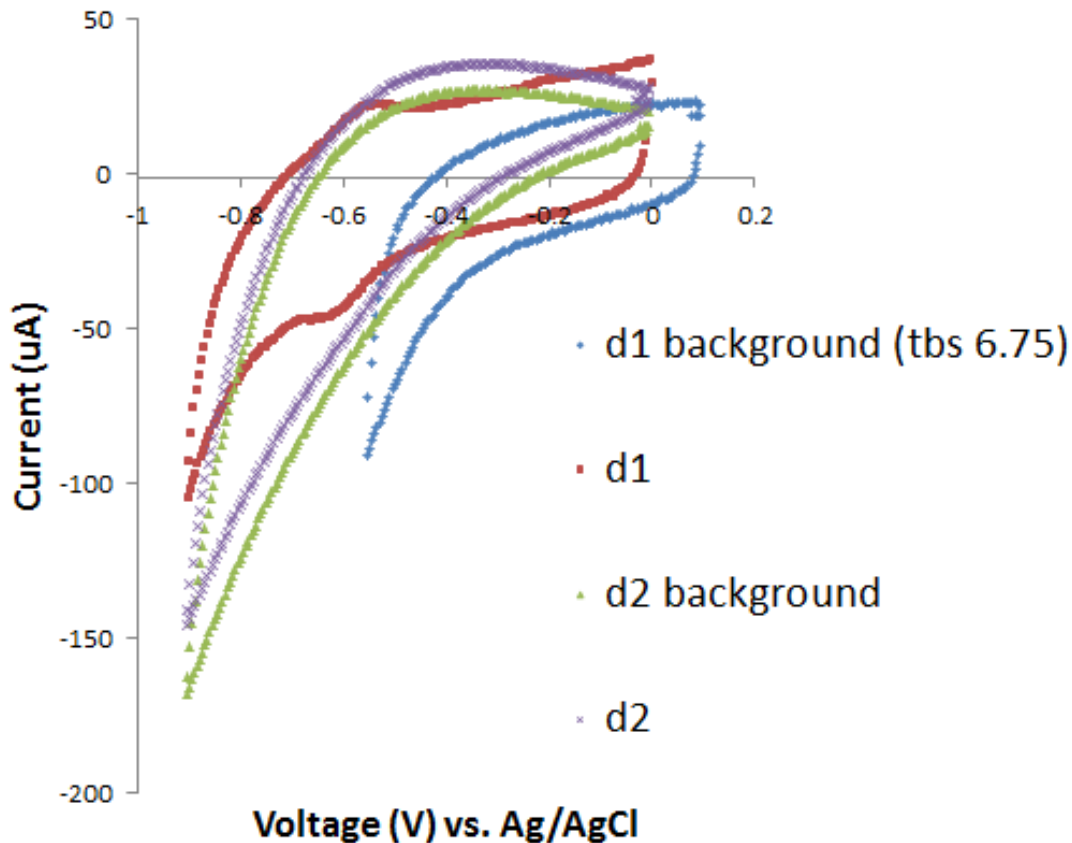
Figure 47: CVs on flat carbon electrodes in 1X TBS 7.0 pH (background) and in the presence of 1mM DAP

For the experiments above, the electrodes D1 was electrochemically activated in 1X PBS 6.0 pH for 20s and D2 was left untreated. Fig. 47 shows that untreated electrode doesn't show any redox peaks in the presence of DAP. D1 shows much improvement over D2 as it shows highly reversible redox peaks but still possess low of background charging current which reduces the signal to noise ratio considerably.

Using a different buffer, HOAc-NaOAc[87], at lower pH value of 4.8 showed immediate good results. This pH value was chosen as HRP activity is highest in 4.5 to 5.5 pH range. The electrode D3 was electrochemically activated the same way as D1. The target signal showed significantly higher redox peak currents compared to those observed in D1 and the

peak to peak separation was only 100mV which suggests that the reaction is highly reversible.
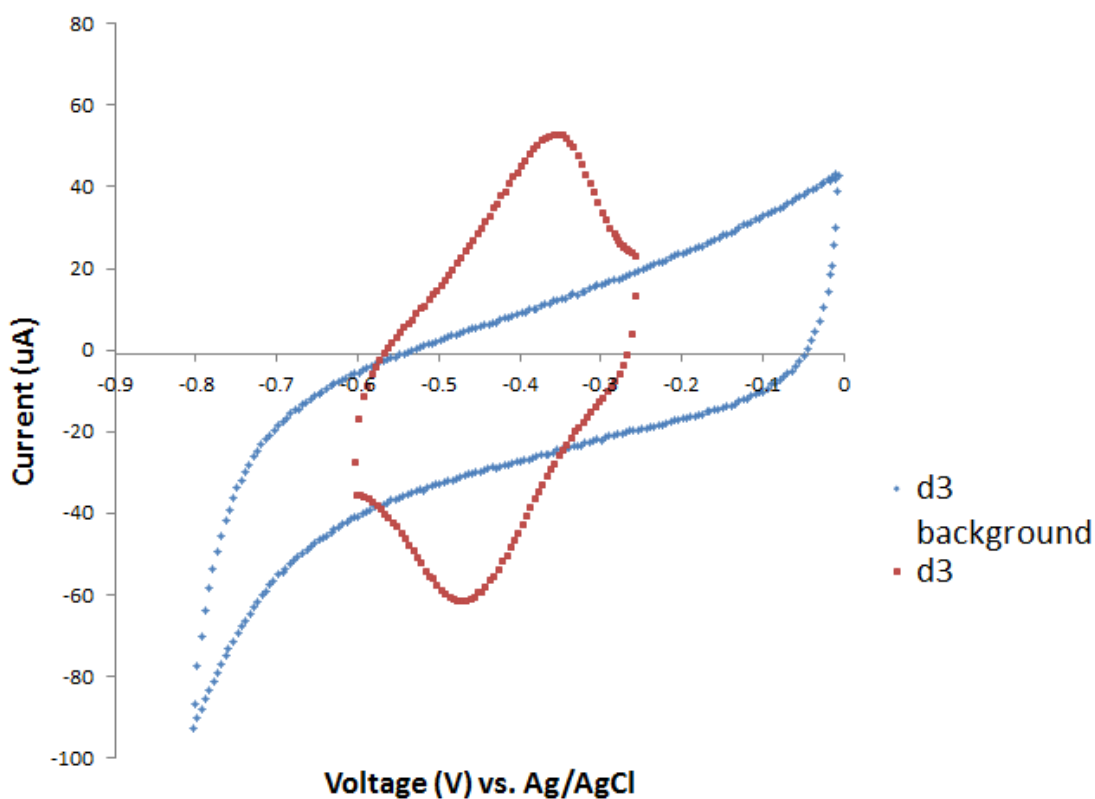
Figure 48: CVs on flat electrodes using 0.2M HOAc-NaOc; 4.5pH (background) and in the presence of 1mM DAP

Moving onto carbon IDEAs

Now that optimum conditions for detecting DAP using carbon flat electrodes were established, the next step was to test the carbon IDEAs for detection. The whole purpose of using carbon IDEAs was to improve detection limit. Similar experiments

94

using lower concentrations of DAP in 0.2M HOAc-NaOAc at 4.8pH were carried out. Fig. 49 shows that even the simplest of IDEA configuration i.e., lowest width/gap ratio of 0.54 and height of 0.2μm was able to detect (with redox amplification) 10nM DAP quite easily. The background signal shows no amplification in dual mode (signal for first 30s) which is obvious due to the absence of redox species. At higher concentrations the amperometric signal show linear improvement with concentration of DAP.
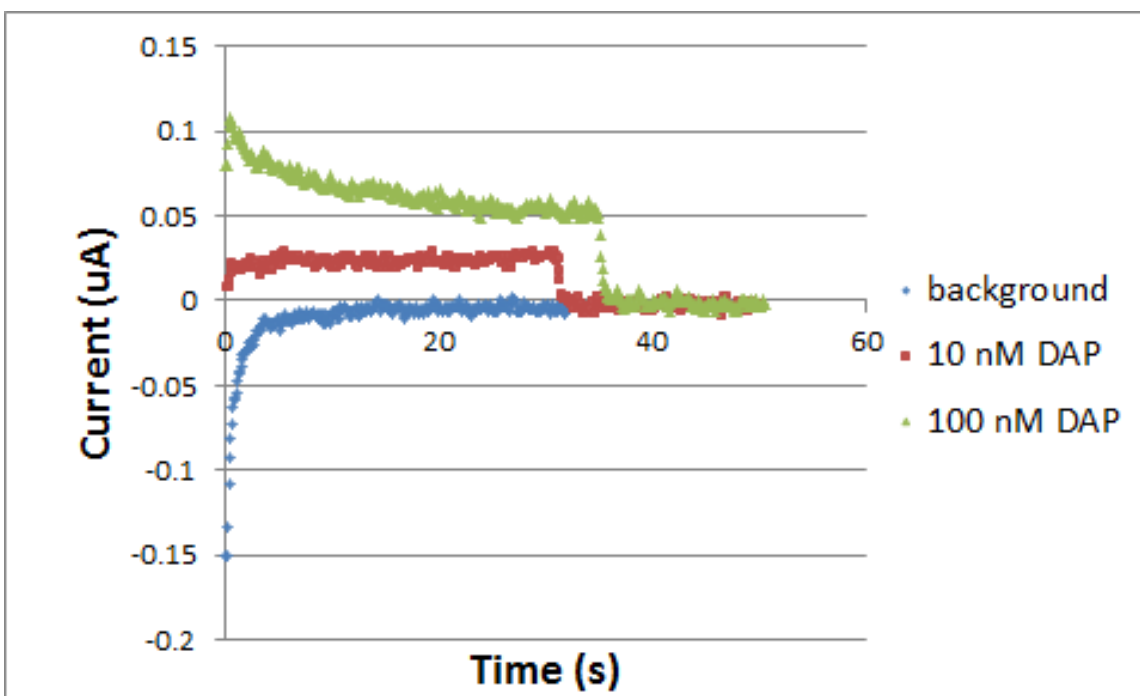
Figure 49: Chronoamperograms using carbon IDEAs with different concentrations of DAP in 0.2M HOAc-NaOAc buffer; 4.8pH

The dynamic range for DAP detection using one specific configuration of carbon IDEAs is displayed in Fig 50. At concentrations ranging from 100pM to 1μm one can clearly see linear increase in amperometric signal. Thereafter, the signal increases dramatically upto 1mM and then it plateaus; following a sigmoidal pattern.

95
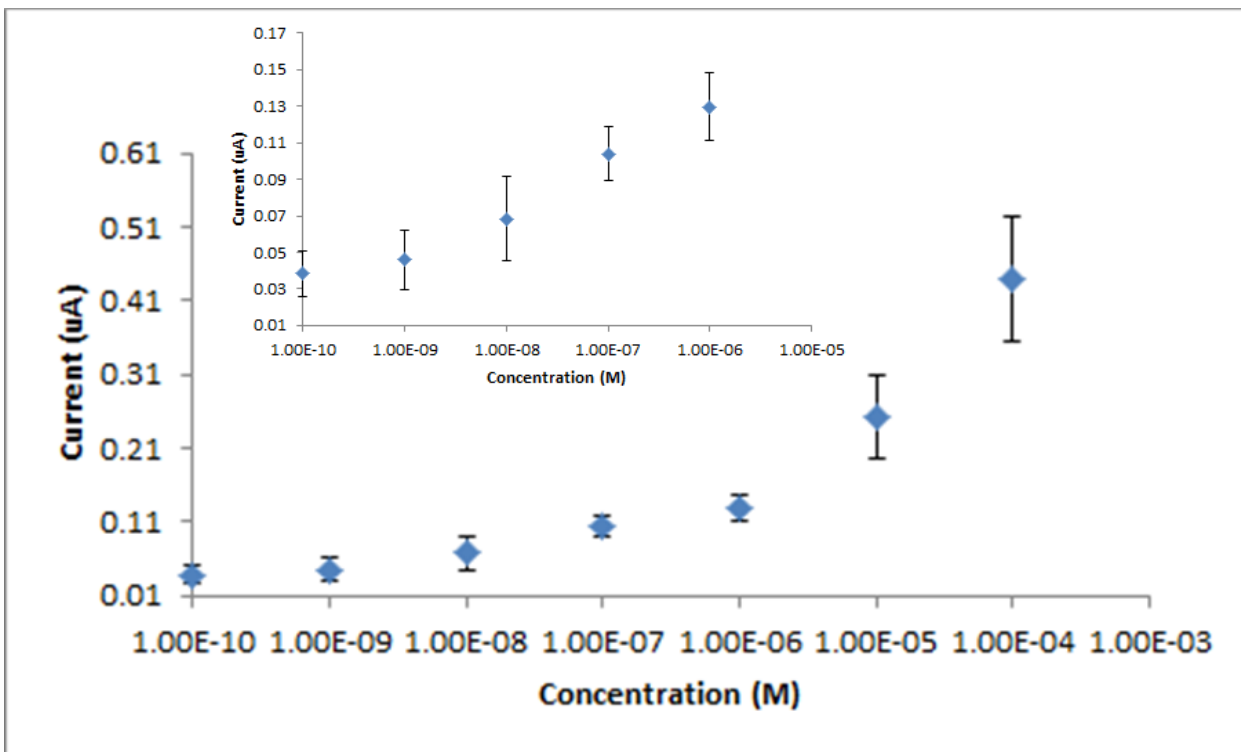
Figure 50: Dynamic range for 2,3 Diaminophenazine detection using carbon IDEAs

Comparison of pAP and DAP as redox probe (Step 1).

The Signal to Noise Ratio (SNR) of at least three was obtained for DAP at 1nM. However, the detection limit for pAP was poor compared to DAP. At concentrations >1µm we got a SNR of two for pAP. Hence DAP was discovered to be at least 1,000 times more sensitive compared to pAP. Moreover, pAP suffered from practical problems such as its instability in air and fouling of electrodes. 10µM of a colorless solution of pAP in 1X TBS degraded and started giving color (visible by naked eye) within 30 minutes. For experiments in Fig. 45, we made fresh solutions for each electrode. Also, at lower concentrations, the degradation takes place even faster. To avoid this, it was necessary to perform the electrochemical detection at the same site where the assay was performed to avoid any delays in detection.

Furthermore, it would be extremely tedious to calibrate (generate a dose response curve) at different concentrations since we can do only one at a time. In order to make sure we obtained the correct dose response, we would have to perform the same immunoassay multiple times and obtain electrochemical reading for different enzyme concentrations (step 2)/standard concentrations (step 3) each time. Considering all the above practical issues in addition to its poor sensitivity compared to DAP, we chose to move ahead only with DAP for next steps.

Conversion of OPD to DAP by HRP: Testing the efficiency of the enzyme (Step 2)

The next step was to check how well the enzyme HRP catalyzes oxidation of OPD to DAP and whether OPD interferes with electrochemical detection of DAP in its solution. The detection antibody (S-MD1, rabbit monoclonal) from Sigma (USA), labeled with HRP was immobilized on 96 well plates (clear, from NUNC) at different concentrations. The exact protocol for this experiment is given below:

1. Prepared Detection Ab Solution: Added 2μL stock detection monclonal antibody; [5.7 mg/mL]) labeled with HRP into 10mL 1xPBS (Final concentration: 1.14μg/ml). Mix well. I coated the first well in a column with 100μL of the above concentration. This was followed by 50% serial dilutions in subsequent wells. The plate was incubated the plate at 4°C overnight.

2. Plate was washed next day four times with 400μl/well of 1xPBS-tween (0.05%)

3. Added OPD (1mM) in 1xPBS at neutral pH and OPD (1mM) in HOAc-NaOAc, pH 4.8 in different columns. Hydrogen peroxide was added. The reaction was allowed to incubate up

to 20 min at room temperature before carefully aspirating out the solution for electrochemical detection. If this step is not carefully performed, HRP may leech out into the solution for electrochemical detection; creating false positive signal.

We see a linear increase in generator current with respect to concentration from 8ng/mL to 0.57µg/mL of the detection antibody labeled with HRP. This trend is more or less similar even if the buffer solution is 1xPBS at 6.0pH and for collector current. One can observe either generator or collector current (will be shown later) for determination as both show linear increase.
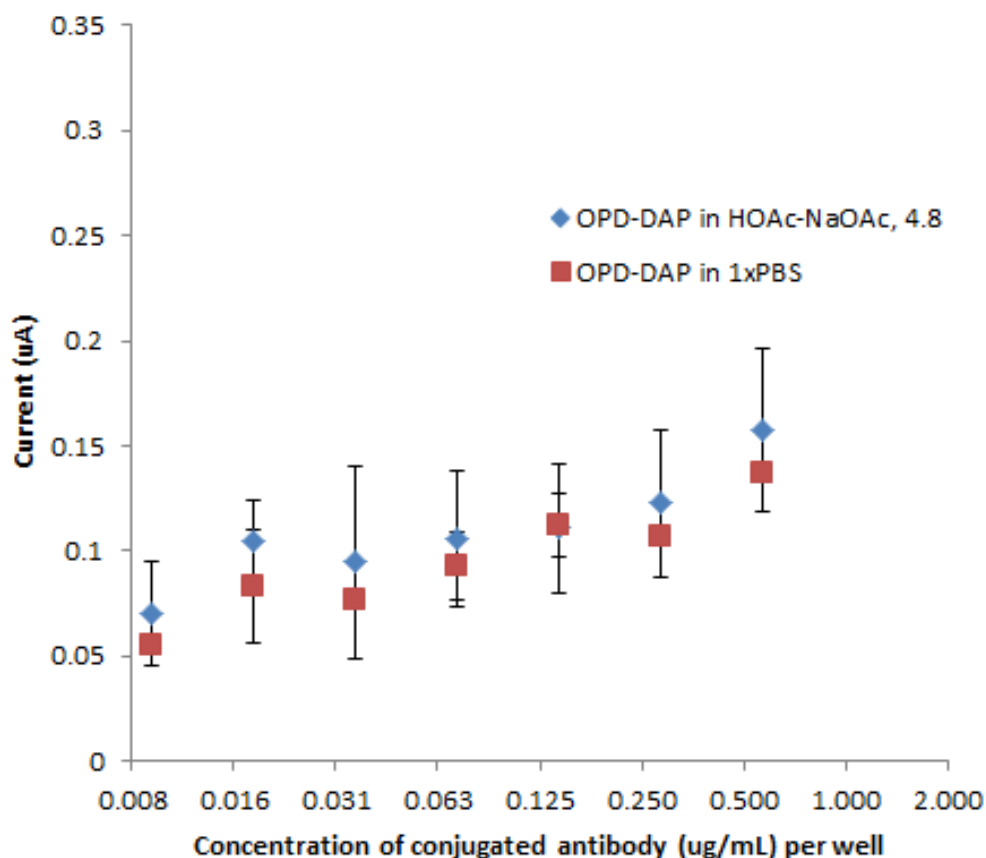
Figure 51: Average generator current (averaged over 30 seconds) vs. concentration of HRP conjugated detection antibody. Similar experiments were carried out in different buffers

i.e., HOAc-NaOAc, pHC 4.8 and 1X PBS, pH 6.0. Carbon IDEAs with width/gap ratio of .54 and height of 0.22μm were used for the experiments

In Fig. 52, we have displayed chronoamperogram from both the generator and the collector. For first 30 seconds, the generator was set at 0.6V vs. pseudo-reference and the collector was set at -0.3V. In single mode of operation, i.e., after 30 seconds, the collector was kept open and only generator current was recorded. An amplification factor of 16 was obtained. This amplificatory factor cannot be determined for collector since we get zero current during single mode operation. However, dual mode collector current which is also the reduction current can be used for analysis just like the generator current. However to use collector current, one must adjust the baseline for background since dual mode collector current shows more background noise than the generator.
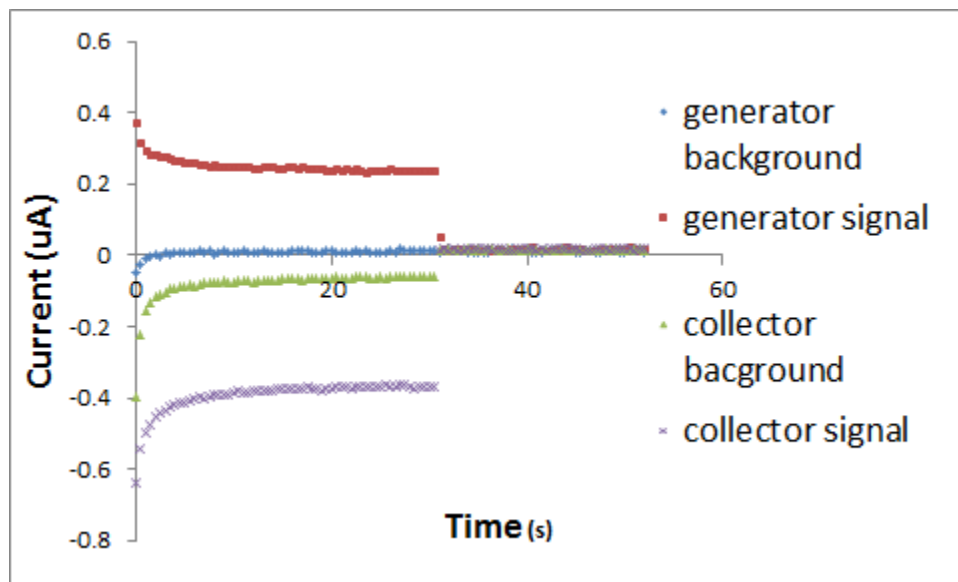
Figure 52: Chronoamperograms of both generator and the collector for carbon IDEAs with width/gap ratio of 0.54 and height of 0.22μm. The background was carried out in 0.2M

Sodium acetate-Acetic acid buffer containing 1mM OPD at pH 4.8 and the target signal arises from 0.57ug/mL of HRP conjugated antibodies. The final solution contained OPD HRP catalyzed DAP in buffer

5.3 Complete Electrochemical Immunoassay

Materials and Methods:

The reagents in the following protocol were provided by Cermed Corporation (Sunnyvale,CA). The capture antibody is a goat polyclonal antibody obtained from Sigma-Aldrich (USA) in storage buffer (TBS pH 7.3, 0.5% BSA, 0.02% NaN3). The 96 well plates were purchased from NUNC and SuperBlock buffer used as blocking buffer was purchased from Thermo Scientific (USA). The detection antibody is rabbit monoclonal antibody (Fab specific) in storage buffer (PBS 49%, 50% glycerol, 0.01% NaN3, BSA 0.5%) purchased from Sigma-Aldrich. The calibrator is an S-P1 recombinant protein stored in 25mM Tris-HCl, pH 7.3, and 100 mM glycine, 10% glycerol, obtained from Active Motif (USA).

 For complete immunoassay we used the following protocol:

1. Prepare Coating Solution: Dilute the stock solution of capture antibody appropriately in 1X PBS, neutral to get final concentration of 1ug/mL. Mix well.

2. Coat plate with 100 µL/well of Coating Solution and incubate overnight at 4°C.

3. Discard Coating Solution. <u>Do not wash</u>.

4. Add 200 µL/well of SuperBlock solution, cover and incubate at room temperature for 1 hour.

5. Discard Blocking Solution. <u>Do Not Wash</u>. Use the plate immediately or let dry inverted at room temperature for 2 hours. Store the dried plate with desiccant at 4°C for up to one week.

6. In a 1mL test tube, add 2.2uL of standard in 1mL of the assay diluent (final conc: 0.5ug/mL). Mix well. Take out 250uL in a separate test tube and 750uL of the assay diluent (final conc: (0.5/4) μg/mL. Mix well. In a 8 channel trough, add 500μL of the latest dilution in the first channel of trough and add 1.5mL of the assay diluent (final conc: 0.03125μg/mL). Dilute 1:4 serially for next 7 troughs.

7. Add 100μL of the above preparation in the corresponding wells in coated plate and incubate for 1 hour with shaking @ 180 rpm at room temperature.

8. Wash plate 4x with 400 μl/well of 1XPBS-tween (t; 0.05%).

9. Prepare Detection Ab Solution: Dilute the stock detection monoclonal antibody in Assay buffer to get final concentration of 0.4μg/ml). Mix well. Add 100μL of the detection antibody solution to the all the wells in the coated plate. Incubate at room temperature for 1 hour. Mix well.

10. Wash plate 4x with 400μl/well of 1XPBS-t.

11. Add 150μL of TMB substrate (Sigma) and incubate while shaking @ 180 rpm at room temp in dark for up to 20 min depending on rate of colorimetric change for optical detection comparison. Add 320μL of 1mM OPD susbtrate (in HOAc-NaOAc and Phosphate Citrate buffer.

12. Add 100μl/well of Stop Solution (0.16M Sulfuric Acid). For electrochemical readings, take out 150μL of reaction product before adding stop solution.

13. Read plate at 450 nm for TMB and 492 nm for OPD

The absorbance readings were done using VersaMax Elisa micro-plate reader and its proprietary software. The electrochemical data is obtained using EDAQ Quadstat 164 as a bipotentiostat and their Chart (version 5.1) software. We started with electrochemically activating the carbon IDEAs as described earlier. Background signal was recorded by solution used for negative control (wells in micro-plate with no standard recombinant protein). Thereafter, the solutions from wells with different standard concentrations were investigated for redox species, starting with the lowest in ascending order. Each data point in the dose response curve represents an average current signal obtained from 3 carbon IDEAs with same configuration.
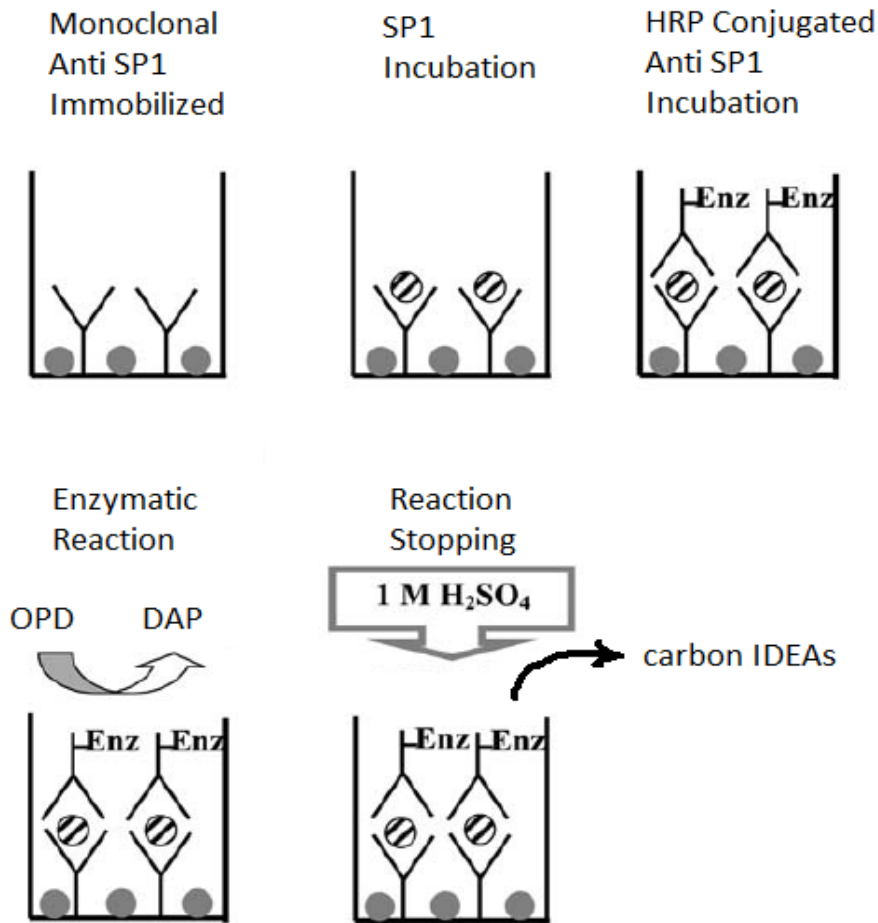
Figure 53: Process Schematic of Immunoassay before aspirating sample solution in to carbon IDEA chip

Results and Discussion

The absorbance data in the Fig. 54, shows a linear range of 0.1ng/mL to 10ng/mL of the standard. The background signal of 0.017 A.U. for negative control gives a detection limit of 0.1ng/mL according to $3\sigma/m$ criteria. The blank is plotted as 0.001 ng/mL instead of zero since zero concentration cannot be plotted on a log scale (x axis) using Excel.
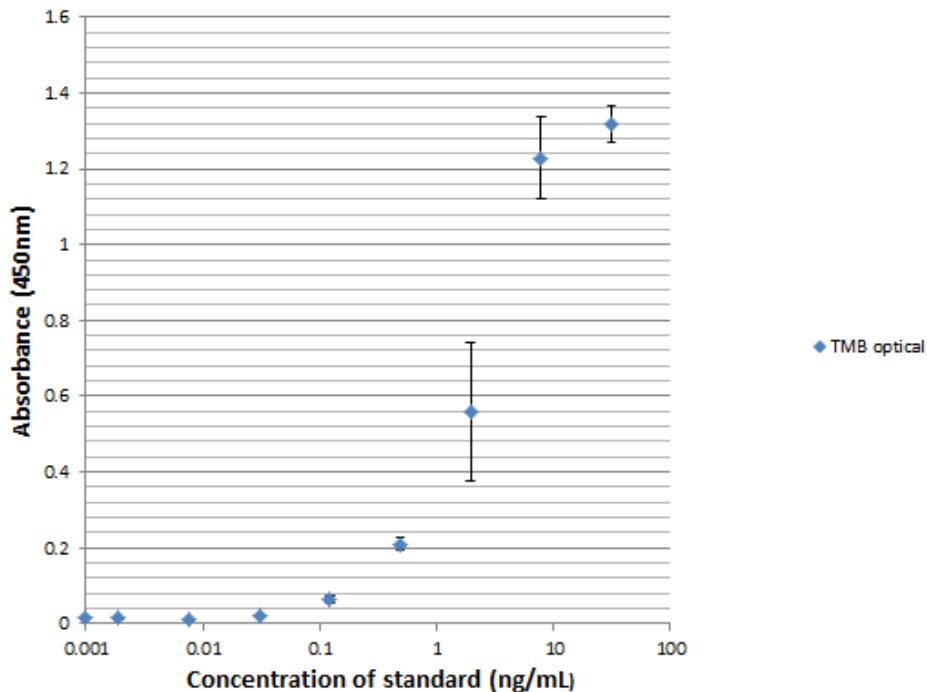
Figure 54: Dose response curve using absorbance signal from TMB vs. protein concentration

In comparison the electrochemical data using carbon IDEAs looks much more promising. In dual mode, the generator was held at 0.6V and the collector was held at -0.3V vs. pseudo-reference. After first 30s, the collector was kept open to operate in single mode. The chronoamperograms don't show any redox amplification for the background signal. Both the generator and the collector show step increase in current with increasing standard concentration. The single mode current did not show any increase for the range of concentration tested. The dual mode showed continuous increase from a factor of 2 to a factor of 30. The dual mode data shows a linear correspondence between the generator current and standard concentration from 0.002 to 10ng/mL. The blank is plotted as 0.001

ng/mL instead of zero since zero concentration cannot be plotted on a log scale (x axis) using Excel. Background signal (5nA) in HOAc-NaOAc is lower compared to that obtained in phosphate citrate buffer (10nA). The extremely low background signals obtained using carbon IDEAs enables a much superior detection limit compared to absorbance.
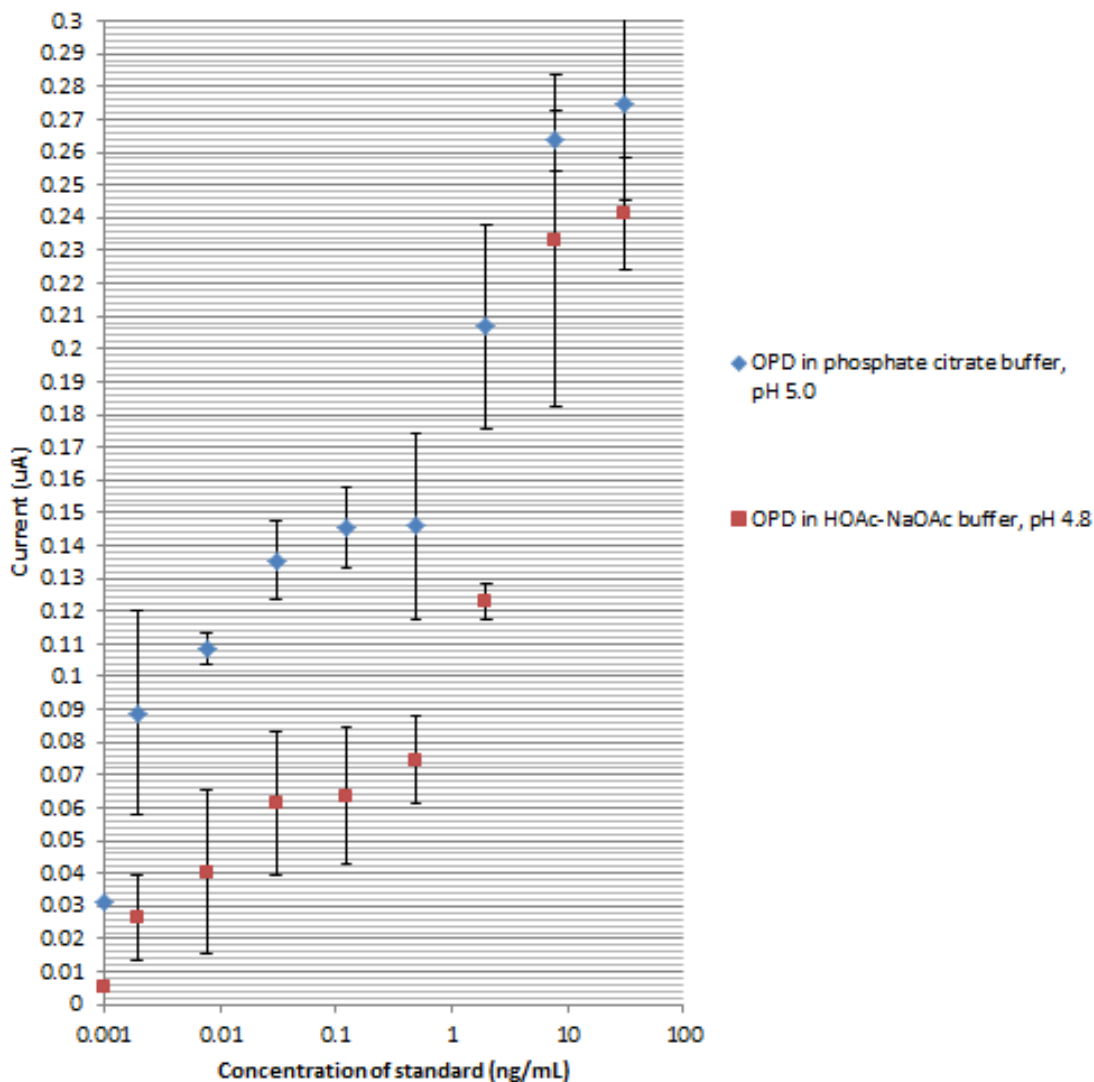
Figure 55: Dual mode generator chronoamperogram data for HRP catalyzed product DAP in both phosphate citrate buffer and HOAc-NaOAc buffer as a function of standard concentration.

Same protocol was carried out using 0.36μm tall carbon IDEAs with similar width/gap configuration. The collector current reponse showed impressive linearity for over 4 orders of magnitude. The background (where x axis coincides) is slightly higher for the collector current but still shows impressive detection limit of 3pg/mL. The molecular wieth of the SP1 recombinant protein is approximately 81kDA which correesponds to a

detection limit of 37fM. Using taller carbon IDEAs one can expect to further decrease the

detection limit.
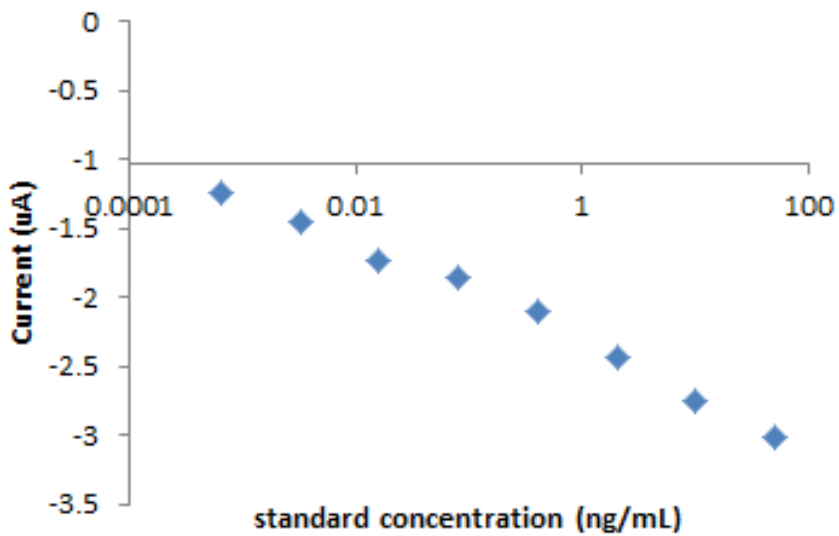
Figure 56: Dual mode collector chronoamperogram data for HRP catalyzed product DAP in phosphate citrate buffer as a function of standard concentration

6. Carbon MEMS Electrodes for Non-Biomedical Applications

6.1 Introduction

So far we have only focused on pyrolyzed carbon microelectrode arrays (Chapter 2) and the resultant phenomenon of redox cycling (Chapter 2), its dependence on geometry (Chapter 3) and biomedical applications of redox cycling (Chapter 4&5). We haven't really discussed fabrication, and materials characterization of pyrolyzed carbon macroelectrodes. In this chapter we will precisely do that along with discussing some of its applications.

The fabrication process of pyrolyzed carbon macroelectrodes is explained schematically in Fig. 8. The pyrolysis process plays an important role in the material properties of the final pyrolyzed product. One can control the process parameters such as temperature, ramp up rate, and dwell time to actually get the desired graphitic content in the pyrolyzed product. Pyrolysis in C-MEMS is often carried out in a flow of N_2 gas with a standard temperature ramp-up of about 10°C/min and a one hour dwell time at the maximum temperature of 900°C, followed by the natural cooling down of the furnace. The pyrolysis conditions we found sensitively impact the microstructure of the C-MEMS electrodes, and as consequence they also influence the chemical and electrochemical behavior necessitating an optimization of the entire C-MEMS process.

Lithographically patterned C-MEMS electrodes pyrolyzed under the standard conditions (as described above) usually result in glassy carbon with a low graphitic content.[98]

The C-MEMS electrodes we fabricated were first photo-patterned in SU-8, a negative tone epoxy based photoresist, and then pyrolyzed. The pyrolysis in this study was performed at three final pyrolysis temperatures, 800, 900, and 1000°C with variable dwell times (1, 4 and 8 hours) at 800 and 900°C. Besides carrying out electrochemistry on the thus obtained

electrodes we characterized them with resistivity measurements, Raman spectroscopy and X-ray diffraction (XRD). In this contribution we report on the optimization of the fabrication of C-MEMS electrodes that may be employed for biological applications,[99,100] chemical sensing[101] and microbatteries.[102] Moreover for the first time, we apply pyrolyzed photoresist electrodes for the analysis of heavy metals ions.

6.2   Fabrication and Optimization of Carbon MEMS Electrodes

The SU-8 photolithography was carried out as described in Chapter 2. However, the photolithography parameters were not modified much from the Microchem datasheets as it was done for carbon IDEAs fabrication. For this process we used SU-8 with higher viscosities (from 1250 to 7000 cSt) to get thicker films different viscosities. The soft bake, exposure and post exposure bake settings were kept according to the datasheets and varied only with thickness of the films used. The exposure was done using soft contact through high quality thin film optical mask that was printed on a high resolution printer.

The pyrolysis process parameters were varied to test its effects on carbon structure. The thus patterned structures were carbonized using a three-step pyrolysis process in an open ended quartz-tube furnace (RD Webb Red Mini #40). First, the samples were heated under N2 (flow rate: 2000 sccm) at 300°C for 60 minutes. The temperature was ramped up at a rate of 10°C/min to the final pyrolysis temperature (800, 900 and 1000°C). The samples were kept at the final pyrolysis temperature for the desired dwell times (1, 4 and 8 hours for both 800 and 900°C) before cooling down. One additional set of electrodes of the same dimensions were pyrolyzed at 1000°C with a dwell time of 1 hour. For prolonged dwell times, the samples used were 20μm thick before pyrolysis. For the 900°C/ 1 hour dwell

time experiment, we worked with five electrodes of different thicknesses, 1, 5, 10, 20 and 30μm before pyrolysis. Before carrying out the electrochemical measurements, the electrodes were insulated with a Monokote tape (Topflite, Champaign IL) in order to make sure that only a defined geometric area is exposed (0.07 cm^2) to the solution during the electrochemical experiments (Figure 39).

Electrode characterization

The thickness of the films before and after pyrolysis was measured on a profilometer (Veeco Dektak3). The resistivity of the electrodes was calculated using a two point probe resistance measurement unit (Keithly 2000 Sourcemeter) in a voltage range of −2.0 to +2.0 V. Raman spectroscopy was carried out on a Renishaw Raman Spectroscopy set up at 514.5 nm. Spectra in the range of 1000 to 1800 cm^{-1} were obtained for the characterization of disordered (D) and graphitic (G) bands of carbon. X Ray Diffraction experiments were carried out on a Rigaku SmartLab X-ray Diffractometer. All voltammetric measurements were carried out using a Palmsens electrochemical workstation at room temperature. A three electrode single compartment electrochemical cell was used for all our experiments with the fabricated carbon electrode as the working electrode, a platinum wire as the counter electrode and an Ag/AgCl (KCl saturated) reference electrode.

Results and Discussion

Effect of the substrate

In order to study the electrochemical response of the electrodes pyrolyzed at different conditions and fabricated on different substrates, a series of cyclic voltammetry (CV)

experiments was carried out using $[Fe(CN)^6]^{4-}$ as a redox probe. This constitutes a reversible redox couple that exhibits an ideal CV behavior characterized by a difference between anodic and cathodic potential peaks (ΔE) of 59 mV.[31] Another parameter that we took into account to evaluate the performance of the various electrodes is the peak current. According to Randles Sevcik equation (Equation 6) the peak current (Ip) is proportional to the electrode area, concentration and diffusion coefficient of the redox species and voltage scan rate. Since all these parameters are maintained constant in our experiments, a higher Ip indicates a lower electrode resistance. Electrodes with a higher Ip are considered more suitable in our experiments.

We UV photo-patterned SU-8 on 4 different substrates namely bare silicon, silicon coated with silicon nitride, silicon coated with silicon oxide and sapphire. The native oxide film on the bare Silicon wafers was removed using a buffer HF etching solution. In order to test the effect of the substrate on the electrochemical behavior of the carbon electrodes on them we performed electrochemical experiments in solutions containing 1mM $[Fe(CN)_6]^{4-}$ and 0.1 M KCl. The oxide and nitride layers offer the necessary insulation compared to bare silicon, which is a semiconductor. Silicon can act as a parallel resistance to the carbon electrodes, thereby drawing some amount of current in its path and increasing the overall resistance of the electrode.
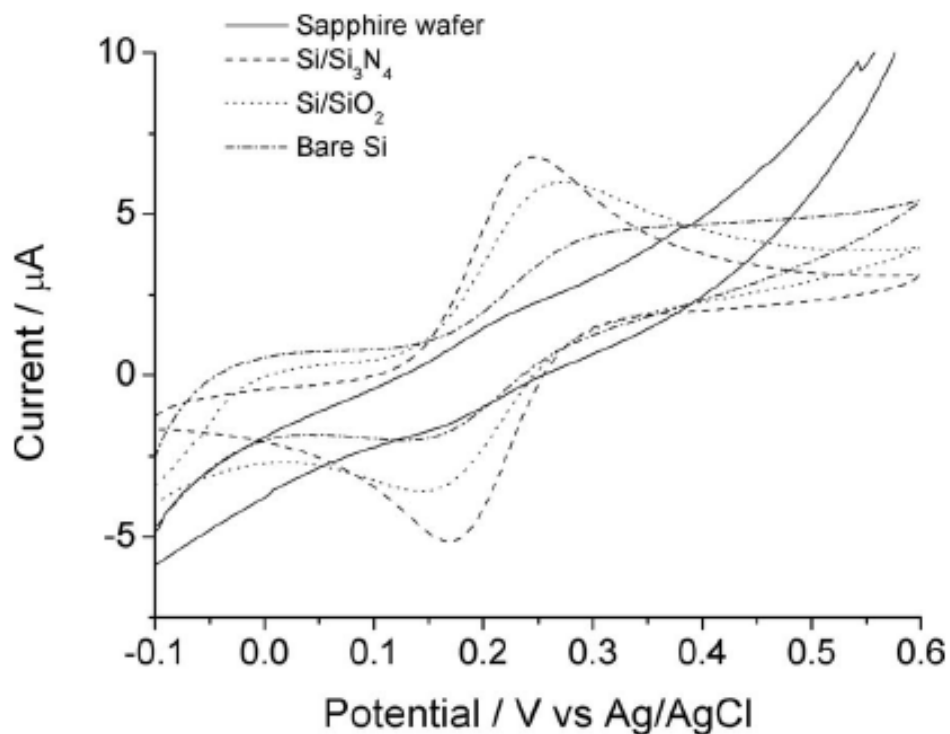
Figure 57: CVs recorded in 0.1M KCl and 1mM $[Fe(CN)_6]^{4-}$ for pyrolyzed carbon electrodes fabricated on different substrates. Scan rate 25mV/s.

In this case, the electrode behaves as if the reaction was quasi-irreversible (high ΔE). Having an insulating oxide or nitride layer ensures that only carbon participates in the electron transfer between electrode and $[Fe(CN)_6]^{4-}/ [Fe(CN)_6]^{3-}$ couple. Out of the 4 substrates, silicon nitride gave the best results in terms of a narrow separation between anodic and cathodic peaks. This response however was only slightly better than that of Si/SiO$_2$ (10% higher Ip and 15% lower ΔE). For the rest of the experiments we chose oxide over nitride as we could thermally grow the oxide layer in our laboratory thus providing a cheaper alternative. It is worth mentioning that carbon films on sapphire exhibited poor adhesion and often peeled off during pyrolysis. Hence we reduced the SU8 film thickness on sapphire to 2µm and the ramp rate to 5°C min^{-1} which resulted in better adhesion.

112

Thinner films increase the resistance of the electrode which is evident, for example, from the slope of the voltammograms in Figure 57

Effect of pyrolysis conditions on electrochemical behavior

Electrochemical and Electrical Characterization

Pyrolysis of a polymer for converting it into carbon encompasses a mass loss due to the release of gases such as oxygen and hydrogen, leading to an isometric shrinkage of the structure. Thermogravimetric analysis (TGA) of pyrolyzed photoresist film reported by Ranganathn et al.,[103] suggests that 80% of the mass loss occurs at temperatures below than 800°C. Our results indicate a further 10% shrinkage in carbon films as the dwell time is increased from 1 hour to 4 hours at 800°C as well as at 900°C.

The effect of the increasing the final pyrolysis temperature on the electrochemical properties of the carbon films has been studied and reported previously.[104] We demonstrate that a combined effect of temperature and dwell time leads to a much improved electrochemical performance of the SU-8 derived carbon. Figure 58 (A, B) illustrates that both ΔE and resistivity of our electrodes decrease on extending the dwell time from 1 to 8 hours. The curves represent ΔE and resistivity values for electrodes pyrolyzed at 800 and 900°C with dwell times 1,4 and 8 hours. For a 1000°C pyrolysis temperature, we only carried out a one hour dwell since the ΔE values were close to 59mV already.

(A)

(B)
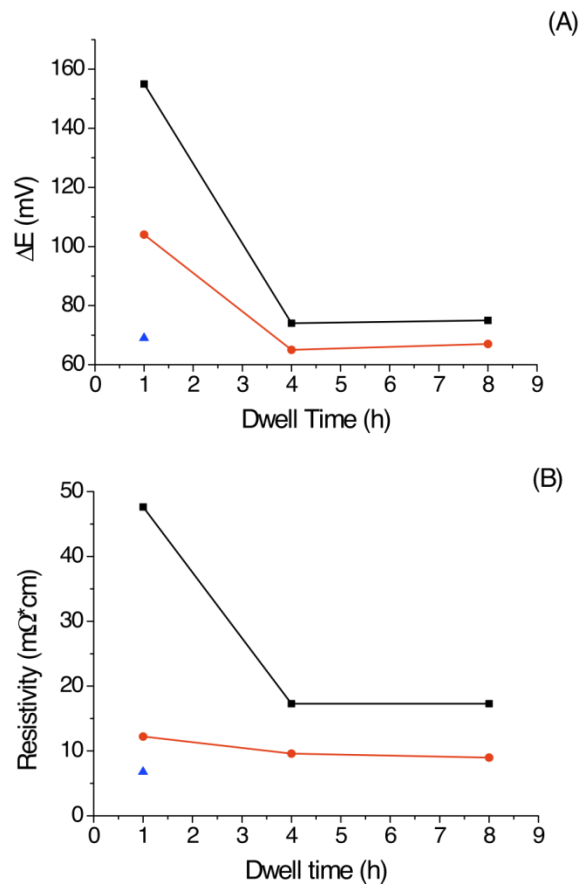
Fig 58: A: Effect of dwell time on the ΔE for the oxidation of $[Fe(CN)_6]^{4-}$ in 0.1M KCl at 25mV/sec. Electrodes pyrolyzed at 800°C (black curve), 900°C (red curve) and 1000°C (blue). B: Effect of the dwell time on the resistivity. Electrodes pyrolyzed at 800°C (black curve), 900°C (red curve) and 1000°C (blue).[25]

Figure 59 presents the cyclic voltammograms of $[Fe(CN)_6]^{4-}$ for electrodes pyrolyzed at different dwell times (1hour and 4 hours) for two different temperatures (A at 800°C and B at 900°C). The role of dwell time is quite evident in the improvement of the electrochemical response (narrower ΔE and higher peak current). No further improvement in the

electrochemical behavior was observed for dwell times longer than 4 hours (see also Table 5).
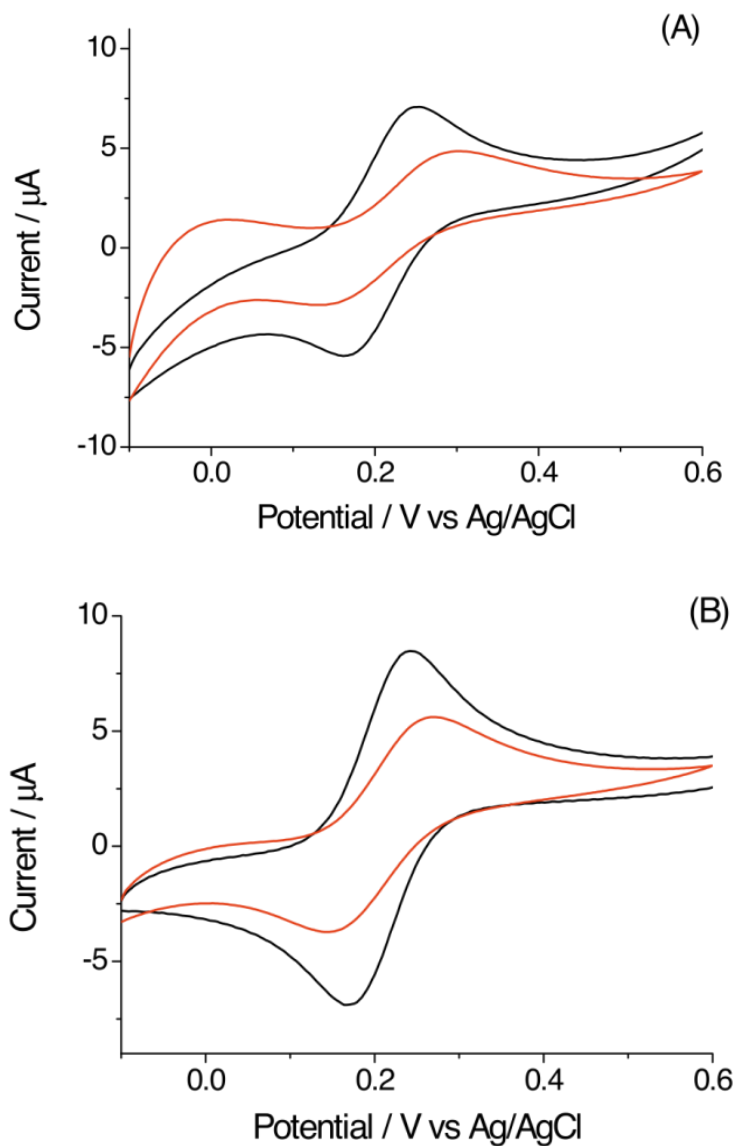
Figure 59: CVs recorded in 0.1 M KCl and 1 mM [Fe(CN)$_6$]$^{4-}$. Scan rate 25 mV/s. A) Red line displays an electrode pyrolyzed at 800°C for 1h; black line one treated at 800°C for 4h. B) Red line displays an electrode pyrolyzed at 900°C for 1h; black line one treated at 900°C for 4h. [25]

We compared the behavior of electrodes at varying scan rates (5 to 50 mV/seconds). Figure 60 represents a comparison between the two limiting cases, namely 800°C pyrolyzed at 1 hour dwell (Figure 60A), and 900°C pyrolyzed at 4 hour dwell (Figure 60B). It is evident that the voltammograms in Fig 60B result in a narrower ΔE , while the voltamograms in figure 60A do not. This behavior, which in principle also results from irreversibility of the redox reaction, is in this case principally attributed to high electrical resistance of the electrode material. The resistance measurements confirmed that the resistance of the glassy carbon material in these two limiting cases described here are indeed significantly different (see below).
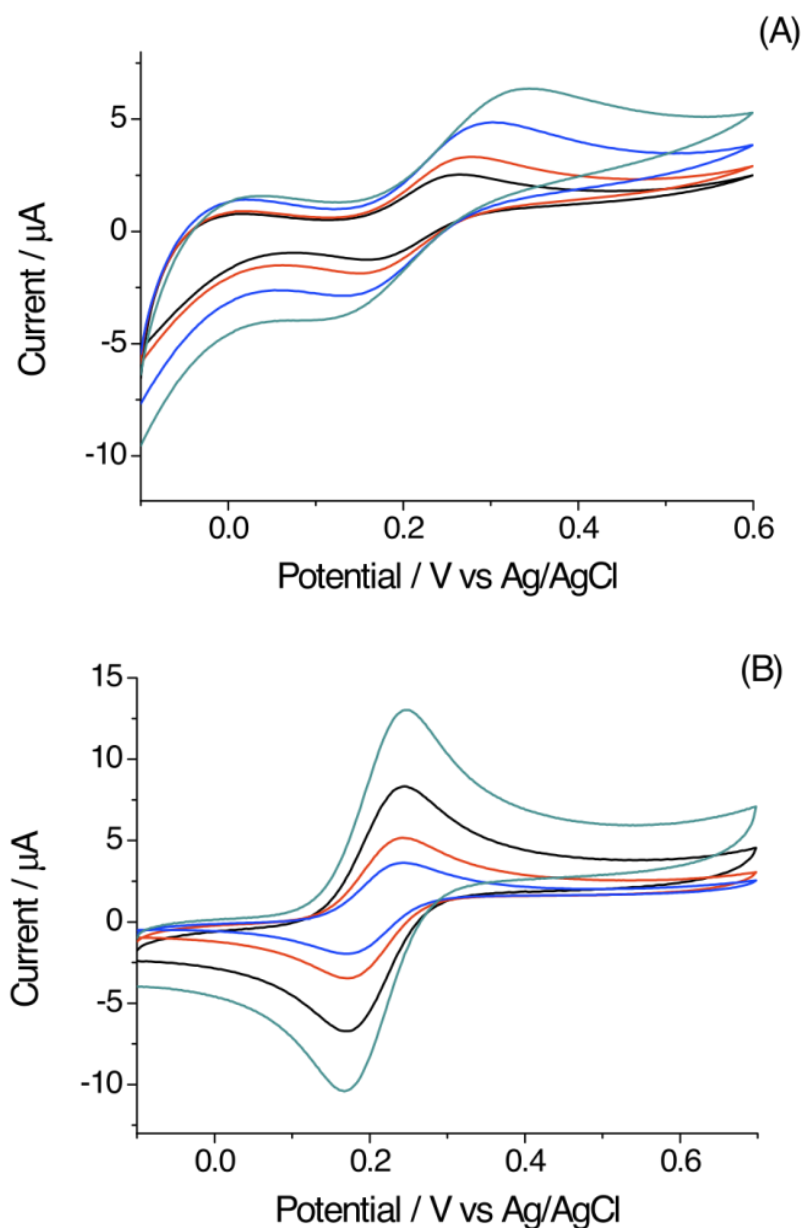
Figure 60: CVs recorded in 0.1 M KCl and 1 mM [Fe(CN)$_6$]$^{4-}$ at different scan rate (from 5 to 50 mV/s). A) Electrode pyrolyzed at 800°C for 1h. B) Electrode pyrolyzed at 900°C for 4h. [25]

Table 4 summarizes the ΔE values, corrections for the uncompensated resistance (iR compensation) and calculations of the ΔE values for electrodes pyrolyzed at different temperature and dwell times. At 800°C there is approximately a 53% decrease in the ΔE value as the dwell time is increased from 1 hour to 4 hour. Similarly, at 900°C, ΔE decreases

by almost 38% as the dwell time is increased from 1 hour to 4 hour, reaching closer to the theoretical value of 59mV. Moreover, a 34% reduction in ΔE is observed when the temperature is increased from 900°C to 1000°C for 1 hour dwell time. This behavior demonstrates that prolonged heat treatment at specified temperature changes the properties of SU-8 derived carbon significantly.

Table 5: Electrochemical and electrical data for electrodes pyrolyzed at different final temperatures and dwell times. *Resistance was measured between A and B in Fig 39A [25]

Temperature and dwell time	ΔE (mV)	Resistance* (Ω)	Corrected ΔE (mV)	Resistivity (mΩ*cm)
800°C 1h	155	1743	136	47.6
800°C 4h	74	701	64	17.3
800°C 8h	75	701	66	17.3
900°C 1h	104	459	98	12.2
900°C 4h	65	389	60	9.6
900°C 8h	67	365	63	9.0
1000°C 1h	69	283	63	6.8

Spectroscopic characterization

Raman spectra and X Ray Diffraction (XRD) patterns for the carbon electrodes were obtained to investigate the graphitic nature of the carbon pyrolyzed under different

conditions. The presence and area ratio of the characteristic "D" (1360 cm^{-1}) and "G" (1582 cm^{-1}) bands in the Raman spectra have been studied extensively for determining the nature of the underlying carbon microstructures[105,106]. A low value of the G/D ratio is an indicative of a smaller graphitic fraction, and is associated with the presence of a greater disorder. A typical spectrum is shown in Figure 61A.
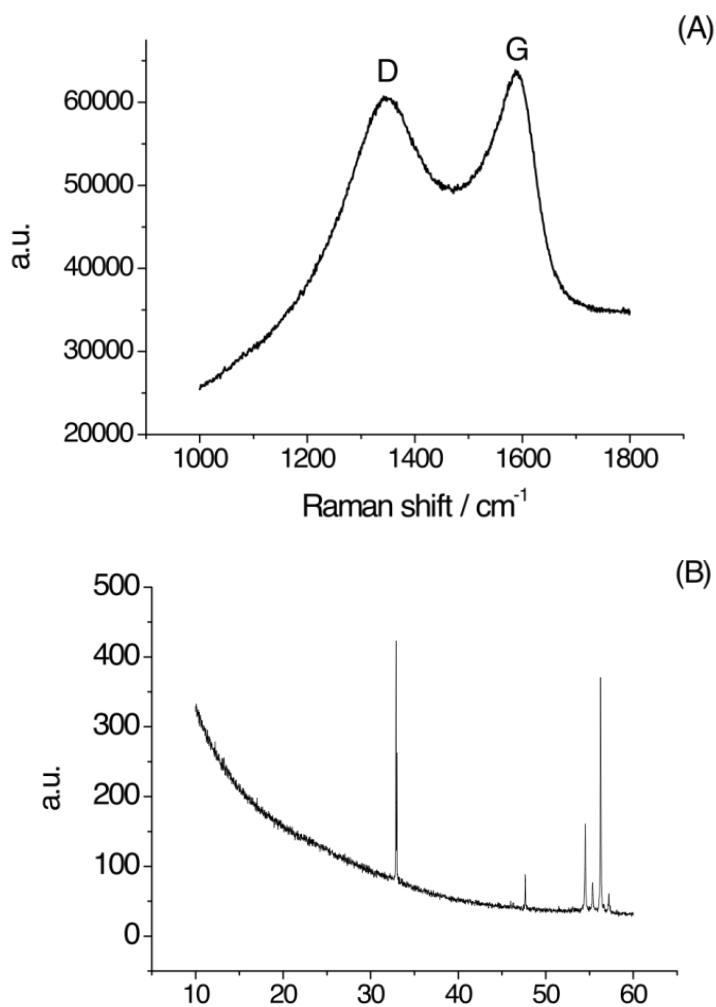
Figure 61: (A) Raman spectra and (B) X Ray Diffraction patterns for SU-8 derived carbon electrodes pyrolyzed at 900°C for 1h. [25]

119

We calculated the area ratio between G/D (applying the corrections for overlapping peaks[107] as function of pyrolysis time and temperature. As indicated in the Table 6, we observed a slightly increase in the graphitic content when pyrolysis temperature is increased.

Table 6: Effect of pyrolysis conditions on graphitic content of the final pyrolyzed carbon electrode. [25]

Pyrolisis conditions	Ratio (G/D)
800 1h	0.51
800 4h	0.52
900 1h	0.54
900 4h	0.65
1000 h	0.95

The increase in G/D ratio with dwell time can be explained with an increase in crystallite sites concentration due to film shrinkage. Indeed, as we mentioned earlier, increasing the dwell time from 1 to 4 hour (both at 800 and 900°C) leads to a reduced thickness of the resulting carbon (~10% further shrinkage), which could be due to a more compact arrangement of the carbon film. It is known that after 900°C, there is no further mass loss due to release of gases etc. from the polymer (i.e., it is already completely converted into carbon), therefore the shrinkage is due to rearrangement in carbon microstructure.

The XRD spectra (Figure 61B) for all samples exhibit a peak at ~54°, characteristic of the (004) planes of graphite[108]. However, a bump extending from 10-25° indicates the presence of amorphous regions. It is known that glassy carbon is composed of intertwined crystalline (graphite) ribbons, filled with amorphous carbons[109], and therefore features a certain degree of crystallinity. These percolated graphite ribbons also allow electron transport and make glassy carbon more suitable for electrical and electrochemical applications, unlike other totally amorphous materials. In-plane and normal to the plane conductivities of graphite have different values[110]. In glassy carbon the random orientation of these ribbons[109] exposes more edge planes, allowing for an enhanced electron transport.

According to IUPAC[111] if the crystalline structure of carbon can be detected in the material by diffraction methods, independent of the volume fraction and the homogeneity of distribution of such crystalline domains, the term graphitic can be used. Pyrolyzed glassy carbon is therefore considered graphitic, which explains the presence of 004 planes at 54° in our XRD spectra. The area of this peak however does not increase significantly for samples pyrolyzed at different temperatures/ dwell times, and we can conclude that there is no, or very small increase in crystallinity of the thus fabricated electrodes. Figure 61B represents one characteristic spectrum. The additional peaks appearing at 33° can be attributed to Silicon.

Effect of film thickness on the resistance and on electrochemical behavior

To determine the effect of film thickness and the change in electrical resistance that goes with that on ΔE, we fabricated SU-8 electrodes of different thicknesses on SiO_2 wafers. In Figure 62 the thicknesses of the electrodes after pyrolysis at 900°C for 1 hour and their respective resistance and ΔE values are illustrated.
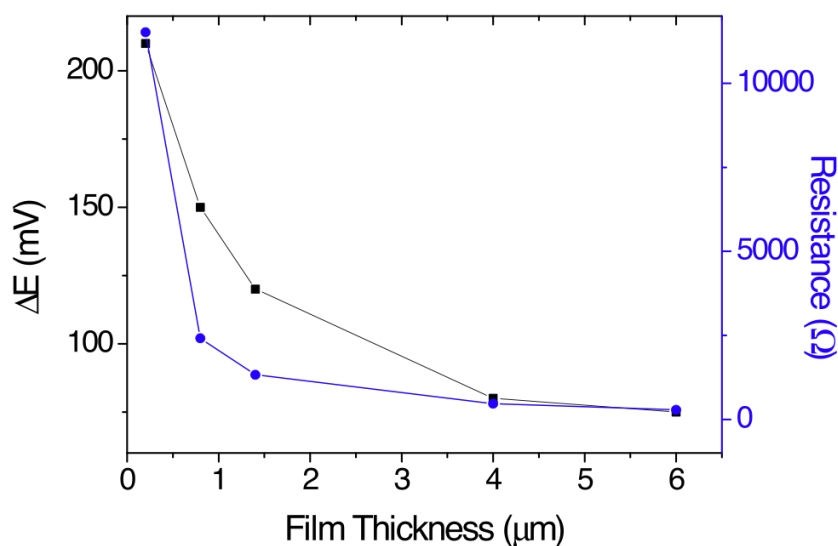
Figure 62: Difference in anodic and cathodic peak potential (ΔE) and resistance for different film thicknesses and keeping other dimensions constant. [25]

In this case we decided to plot resistance (instead of resistivity) because the starting material and the pyrolysis parameters are the same. Since resistivity is a property of the material (instead of geometry) this parameter is not affected by thickness. The values we found were in fact all in good agreement one with the others.

As the thickness of the carbon film decreases, the end to end resistance (between point A and B in Figure 39) goes up, which in turn increases the ΔE and the electrodes are no longer ideal for electrochemical applications. We can conclude from this data (collected for 900°C, 1h) that there is a minimum required thickness (~4μm for the given electrode dimensions, see also Figure 39) which gives a quasi-ideal response. Thicker films don't bring significant improvement of the electrochemical performances.

Effect of the supporting electrolyte concentration

In order to explore the potential of these electrodes for a wide range of electrochemical applications, we studied the effect of the electrolyte concentration on the standard potential of ferro/ferricyanide couple.

Figure 63 shows CVs for the 1mM $[Fe(CN)_6]^{4-}$ in solutions containing four different concentrations of KCl (from 0.05 to 1M) at 5 mVs^{-1}. It can be observed that $E_{1/2}$ changes with the electrolyte concentration. Such behavior, which was demonstrated previously for Pt microelectrodes[112], can only arise if the formal potential for the ferro/ferrricyanide depends on the concentration of KCl.

As per the Nernst equation (equation 8) to determine the equilibrium potential of a half cell in an electrochemical cell, the activity of the redox species is expressed as product of an activity coefficient (γ) and the concentration (C).

$$E = E^0 - (RT/nF)ln(\gamma_r/\gamma_o) - (RT/nF)(C_r/C_o)$$
<div align="right">Equation 8</div>

In the absence of supporting electrolyte $\gamma_r = \gamma_o$ but in the presence of added salt the activity coefficients for both oxidized and reduced species change[113], which in turn explains the shift.
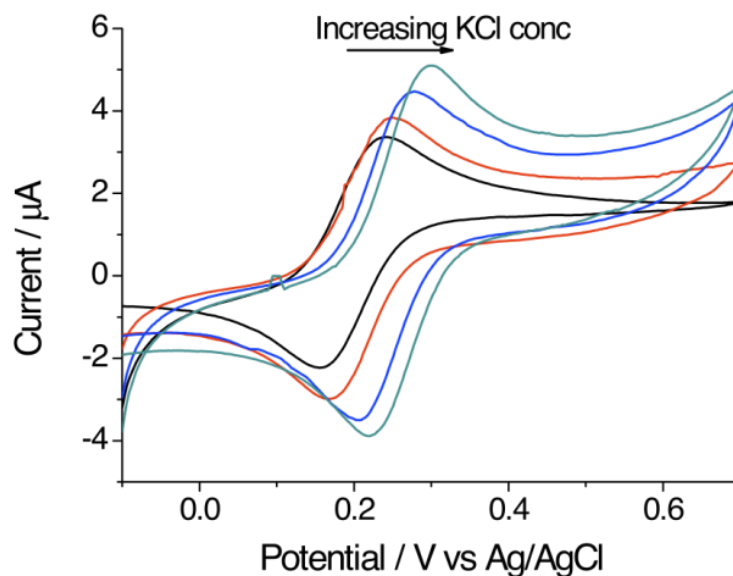
Figure 63: CV recorded using C-MEMS electrode, at 5mV/s, in solution of 1mM [Fe(CN)$_6$]$^{4-}$ and four different concentrations of KCl (from 0.05 to 1M). [25]

Table 7: Data taken from cyclic voltammograms at C-MEMS electrode, in solutions of 1 mM [Fe(CN)$_6$]$^{4-}$ in 4 different concentrations of aqueous KCl. [25]

Scan rate mVs^{-1}	0.05 M KCl		0.1 M KCl		0.5 M KCl		1 M KCl	
	E$_{1/2}$ (mV)	ΔE (mV)	E$_{1/2}$ (mV)	ΔE (mV)	E$_{1/2}$ (mV)	ΔE (mV)	E$_{1/2}$ (mV)	ΔE (mV)
50	196	99	206	89	240	81	258	97
25	197	90	208	81	241	75	259	87
5	197	77	210	75	241	63	259	74

This data demonstrates that the carbon derived from pyrolyzed photoresist can be used to study redox reaction kinetics as the electrochemical behavior of these electrodes is similar to that of the traditionally used electrodes such as noble metals (Pt, Au) or commercially available glassy carbon.

Accessible potential window

It is also important to explore both the accessible potential window and the electrochemical behavior of the photoresist derived carbon electrodes at negative potential values. Figure 9A presents a CV recorded in 0.01 M HCl (pH 2) in the absence of dissolved oxygen which shows that the potential window can go down to 1.4V in acidic media. Repetitive scanning to -1.3V at C-MEMS electrode in acidic media didn't give any change in the double layer charging currents demonstrating the stability of these electrodes also in extreme pH values.
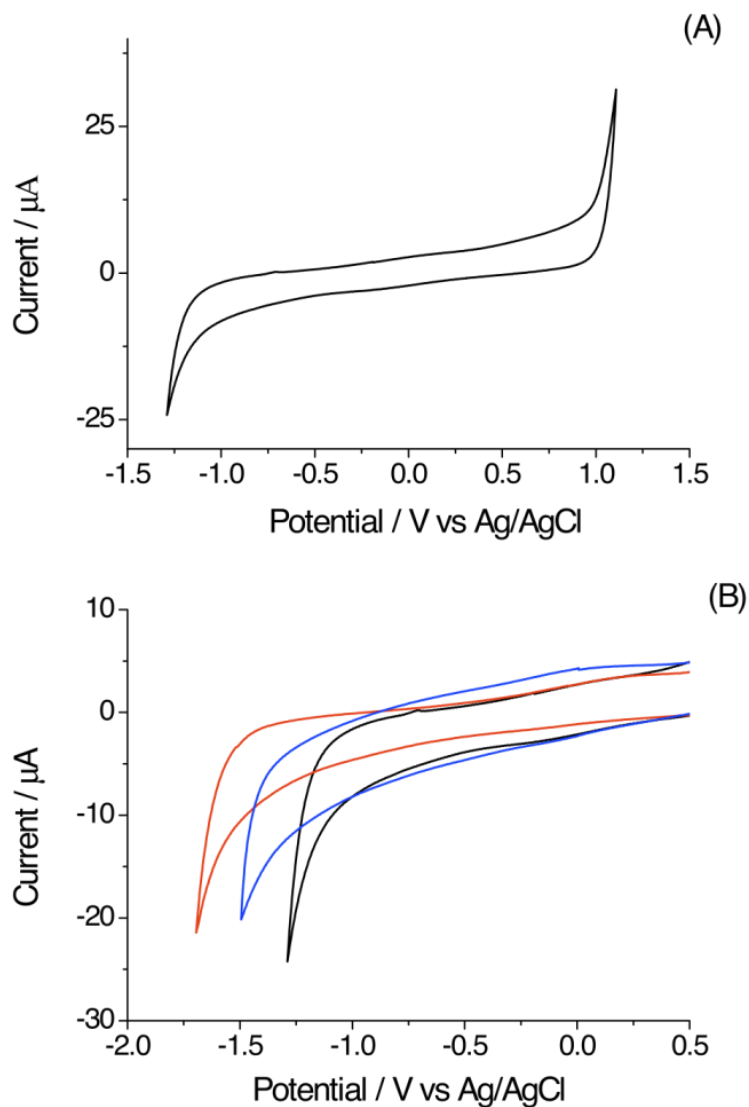
Fig. 64. A) Background cyclic voltammogram recorded at 25 mV s^{-1} in 10^{-2} M HCl, pH 2.2. B) Background cyclic voltammograms recorded at 25 mV s^{-1} at a carbon electrode in: 10^{-2} M phosphate buffer, pH 7.0 (red line); 10^{-2} M acetate buffer, pH 4.5 (blue line); (black line). [25]

As previously demonstrated in the literature[114], the nature of the increase in the background current in the cathodic range is made clear by examining its pH dependence. The voltammograms in Fig. 64B clearly show that these currents are attributable to proton reduction; indeed, the potential value at which a certain reduction current is measured, shifts negatively by 60 mV per unit increase in the pH of the solution.

Conclusions

We carried out pyrolysis of SU-8 patterns at different temperatures and dwell times and demonstrated the effect of these conditions on the electrochemical behavior of the thus derived carbon. The electrodes are also characterized by Raman spectroscopy, XRD, and resistance measurements. Carbon electrodes pyrolyzed at 900°C for 4 hours display near-ideal electrochemical behavior. We also investigated the influence of substrate and electrode thickness on electrochemistry of carbon. We found that the electrodes fabricated on Si_3N_4 and SiO_2 substrates display better electrochemical response compared to those fabricated on bare silicon. We also tested electrode fabrication on to sapphire substrate, however a poor adhesion of carbon films on sapphire caused SU8 films thicker than 2μm to peel-off during pyrolysis.

6.3 Applications of Cabon MEMS Macroelectrodes

6.3.1 Anodic stripping voltammetry of Cd(II) and Pb(II) at Bi modified Carbon Electrodes

The electroanalytical performance of the previously described carbon electrodes was studied for the first time in the simultaneous determination of lead and cadmium through anodic stripping voltammetry (ASV). In situ surface modification of SU-8 derived carbon electrodes with bismuth was performed in order to increase the overpotential for hydrogen evolution in the cathodic range, thus, enabling detection of both analytes.

Bismuth electrode exhibits a cathodic part of the operational potential window which is very similar to that of mercury, with even superior performance in the presence of dissolved oxygen. Due to its non-toxic character and excellent electro-analytical

performance, bismuth electrodes have been exploited for various electro-analytical applications[115,116].

In-situ modified carbon electrode was studied while increasing the concetration of Pb(II) and Cd(II) in the range of 5 and 30.0 µgL^{-1}, as shown in Figure 65A and B.

The electrode revealed a good linear behavior in the examined concetration range for both analytes in combination with 300 s accumulation time being the stripping signals well good separated and surrounded by low background contribution. The detection limit (DL) was calculated by using the $3\sigma/m$ criterion and resulted 0.8 µgL^{-1} for Pb(II) and 0.7 µgL^{-1} for Cd(II), which are close to those obtained with commercially available glassy carbon substrates[117,118].
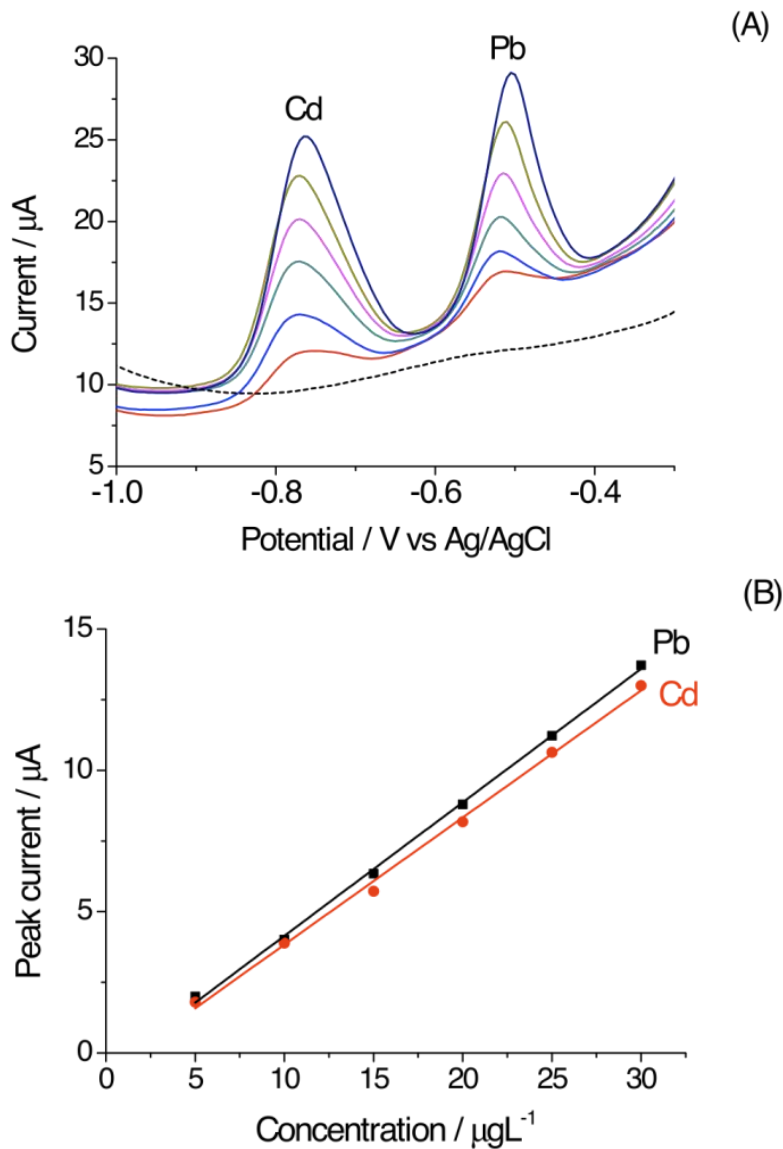
Figure 65: SW-ASV recorded at the in-situ prepared Bi-carbon electrode in 0.1 M acetate buffer (pH 4.5), 10mgL^{-1} Bi(III) in the absence (dotted line) and presence of increasing concentrations of Pb(II) and Cd(II), from 5 to 30µg L^{-1} (full lines). Deposition at -1.1V for 300s. SWV parameters: frequency 20Hz, amplitude 50mV, potential step of 5mV. Inset: corresponding calibration plot. [25]

Pyrolyzed photoresist carbon electrodes have been applied for the first time as substrates for the simultaneous determination of Cd (II) and Pb (II) through anodic stripping

voltammetry and DL as low as 0.7 and 0.8 µgL^{-1} were calculated. Carbon constitutes excellent material for electrochemical applications that can be optmized employing the pyrolysis conditions we reported. CMEMS process can lead to various two and three dimensional electrode designs suitable for a wide range of nextgeneration electrochemical sensors.

6.3.2 Adsorptive cathodic stripping voltammetric determination (AdCSCV) of Cr(VI) using bismuth modified carbon MEMS electrodes

Carbon MEMS electrodes, as shown in Fig. 39, was modified with bismuth via ex-situ modification. During the plating step, the PPCE was placed in 0.1M acetate buffer (pH 4.5), 1 mg/L Bi(III) solution[119]. After an electrochemical cleaning step (+0.5V for 120s), bismuth was potentiostatically deposited at 1.2V for 300 s under stirring conditions. Afterwards, the modified electrodes were placed in an electrochemical cell together with 0.5µmol/L pyro-catechol violet and 0.1mol/L NaNO$_3$ in 0.01mol/L acetate buffer (pH 6). After accumulation (adsorption) at -0.2V for 60s, followed by a 15s equilibration step, a cathodic stripping square-wave voltammogram (SWV) from 0.2 V to 1.2V was recorded, with a frequency of 25Hz, a potential step of 5mV and an amplitude of 50mV. After each measurement, a cleaning step was performed by keeping the potential at 1.4V for 20s.

The total inorganic Cr concentration was determined by first oxidizing Cr(III) to Cr(VI). This step was carried out avoiding chemical contamination by using UV irradiation of an oxygen-saturated solution. A photochemical reactor was designed for Cr(III) oxidation, consisting of a 20mL quartz cell; the cell was irradiated by a 400W medium pressure mercury vapor lamp (Hanovia). Prior to and during the irradiation, (usually 30 minutes),

the solution was continually purged with high purity O_2 (SAPIO). Ozone formed in this process is able to effectively oxidize Cr(III) to Cr(VI), according to the following reaction.

$$O_3 + 2Cr(III) + 6H^+ \rightarrow 2Cr(VI) + 3H_2O$$
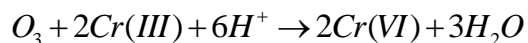
In order to lower the detection limit of Cr(VI), the choice of the supporting electrolyte concentration and electroanalytical parameters were optimized[119] The adsorptive cathodic stripping voltammetric determination of Cr(VI) at the modified carbon MEMS electrodes was selective even in the presence in Cr(III).
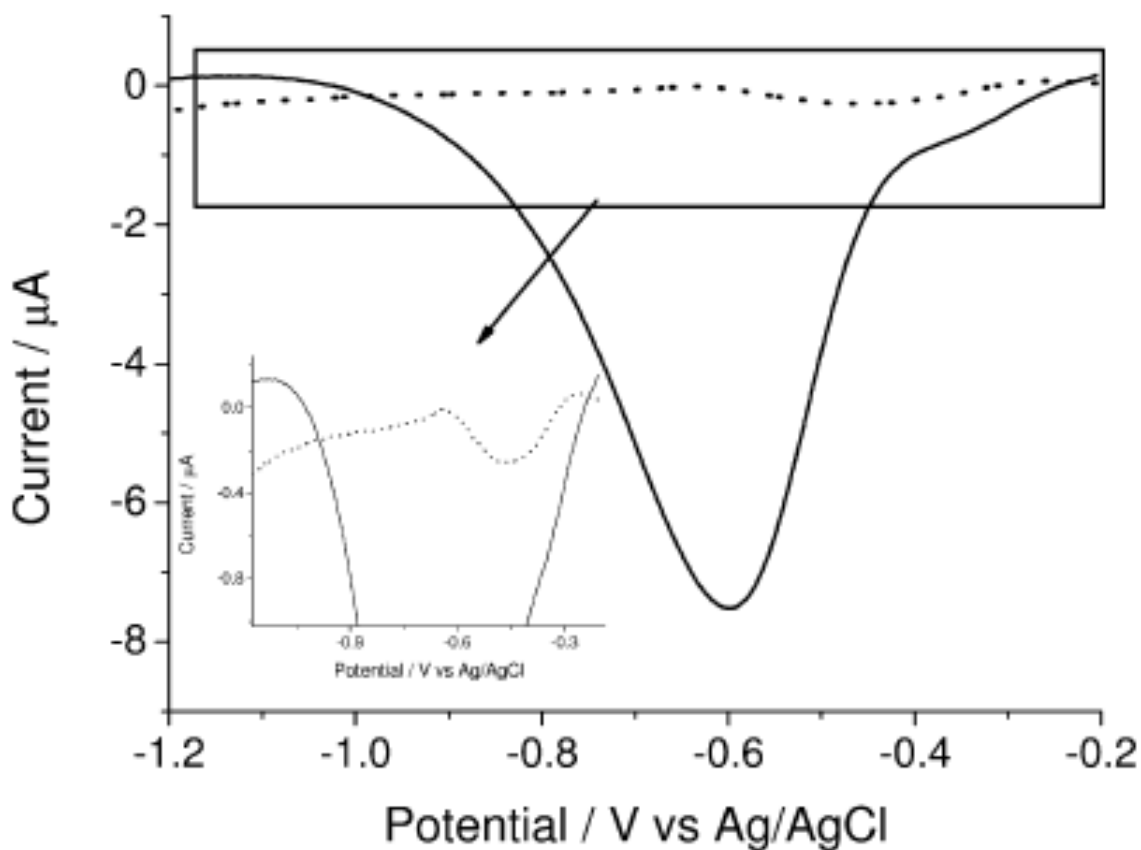
Figure 66: AdCSVs at the ex-situ prepared carbon MEMS electrodes in solution of 10μg/L of Cr(VI), acetate buffer and 0.5μmol/L pyro-catechol violet in the presence (solid line) and in the absence (dotted line) of 0.1mol/L $NaNO_3$. Accumulation at -0.2V for 60s; equilibration time of 15s; SWV parameters: frequency of 25 Hz, potential step of 5mV and amplitude of 50mV [119]

The selectivity of the method to Cr(VI) in presence of Cr(III) was verified. The dotted line voltammogram in Figure 5 presents the CSV recorded at the bismuth modified carbon MEMS electrodes in a solution containing Cr(III): the pattern is identical to the blank signal. On the other hand, when increasing the concentration of Cr(VI) from 5 to 25µg/L a well-defined peak is detected at -0.65V, whose peak current increases linearly with the concentration of Cr(VI) (see inset in Figure 5). A detection limit of 0.1µg/L was calculated by using the $3\sigma/m$ criterion, where σ is the standard deviation of the blank and m is the slope of the calibration plot. The calculated detection limit is comparable or lower than those obtained with other electro-analytical methods[120–122].
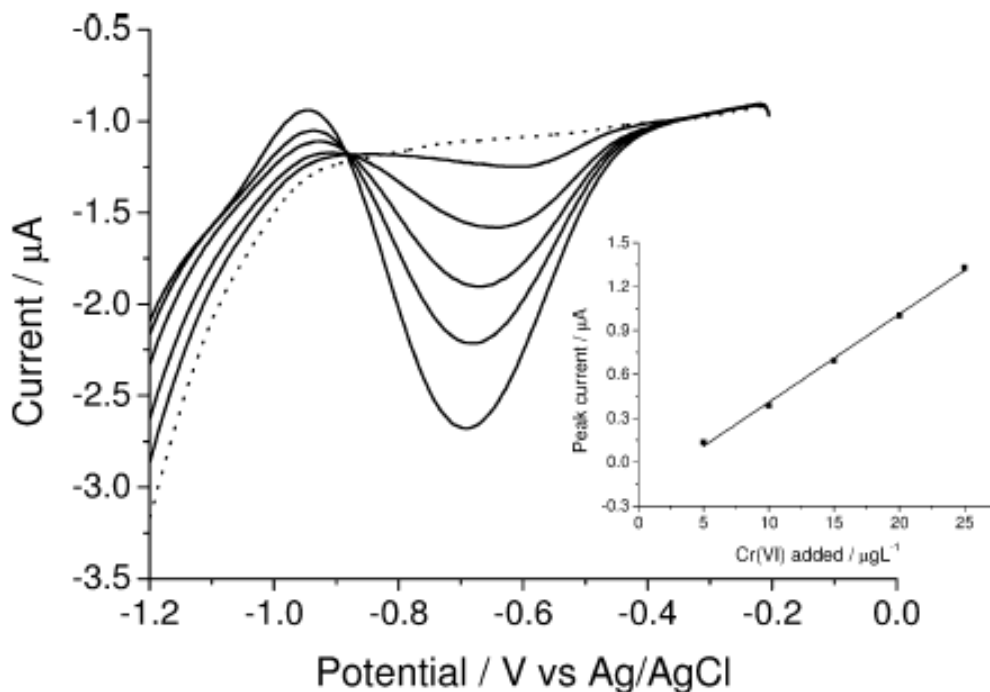
Figure 67: AdCSVs recorded at Bi modified carbon MEMS electrodes in solution of waste-water sample after UV oxidation, spiked with increasing concentrations of Cr(VI), from 5 µg/L up to 20µg/L. Other conditions are as in Figure 66. [119]

6.3.3 Carbon MEMS Electrodes as Electrochemical Double Layer Capacitors (EDLC)

In this contribution, we introduce a new type of high surface area porous glassy carbon (PGC) material for EDLC applications. PGC is obtained from lithographically patterned SU-8 by a modified 'rapid' pyrolysis technique featuring an ultra-fast temperature ramp rate. The chemical structure of SU-8 is illustrated in Fig. 68(a). SU-8 yields an extremely low porosity graphitic GC when slowly pyrolyzed at 900°C. The long polymer chains with aromatic carbon backbone facilitate C-C bond formation during pyrolysis, which results in GC with greatly improved ordering of the graphite crystallite than that obtained from other polymers. Fig. 68(b) represents the microstructure of the GC derived from pyrolysis of SU-8 at 900°C with a temperature ramp rate (room temperature to 900°C) of 2°C/min. If the temperature ramp up is rapid, i.e., is maintained above 25°C/min, we obtain a bubble containing GC material (PGC) that features the GC microstructure, but with a much enhanced surface area due to the morphological changes resulting from the presence of bubbles. PGC features hemispherical pores on its surface created by the bursting of bubbles (~5μm wide) generated due to the release of the indigenous O and H of SU-8 during pyrolysis (see Fig. 69).
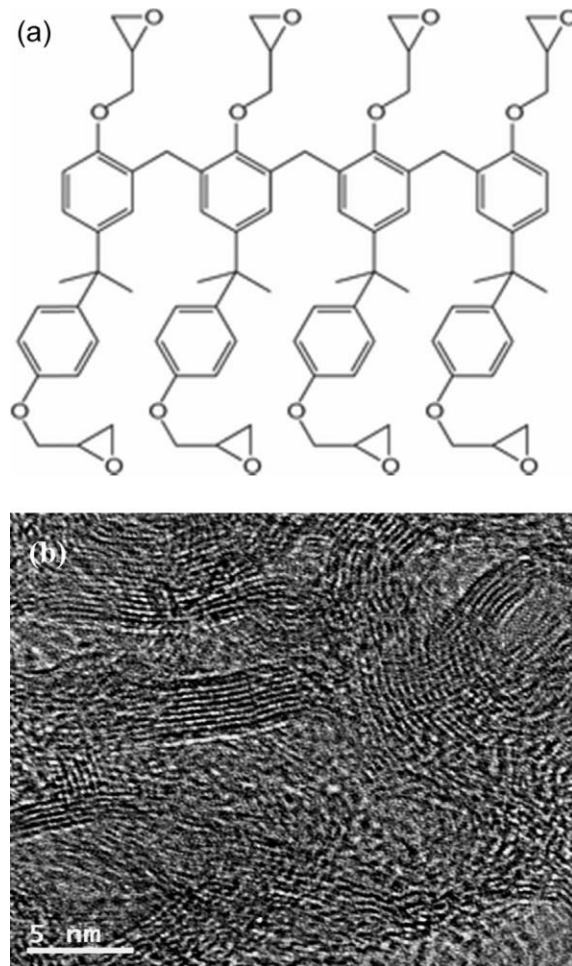
Figure 68: a) Chemical Structure of SU-8 b) TEM micrograph of GC derived pyrolysis of SU-8 at 900°C at a ramp rate of 5°C/min. [132]

The bubble generation renders the car-bon surface rough and leads, as we shall see below, to a three-fold increase in the electrode surface area. We performed a reactive ion etch (RIE) employing oxygen plasma and calculated the electrical resistance for PGC to confirm that the microstructure and electrical conductivity of PGC remain the same as that of the flat GC obtained from SU-8 via standard pyrolysis (performed at lower than10°C/min temperature ramp rate).Rapid pyrolysis (ramp rate $\geq$25°C/min) is a one-step carbonization approach that enables the manufacture of enhanced surface area carbon with tunable

bubble density from SU-8 films of pre-defined dimensions. This technique does not require any modifications in the composition of SU-8, or any change in the pyrolysis environment and thus offers a highly pure material. We carried out a study on pyrolysis at three different temperature ramps rates (25, 50 and 75°C/min) and determined the surface area of the thus fabricated PGC employing chronoamperometry. Unlike other surface area measurement techniques such as gas adsorption isotherms that utilize the Brunauer–Emmett–Teller (BET) theory to obtain the specific surface area irrespective of its wetting during the electrochemical tests, chronoamperometry measures only the electrochemically available (wetted) surface. Therefore, we evaluated the specific capacitance of PGC based on its chronoamperometric surface area, which is more pertinent to electrochemical applications reported here. The wetting of the electrodes during CV is extremely important in order to completely utilize the extended surface for electrochemical measurements. Even for a very low density/high surface area carbon, the capacitance may not increase as expected if the electrolyte cannot access the entire surface. Wetting of carbon electrodes has been extensively studied by electrochemists, and various physical and chemical pathways for improving the electrochemically accessible area have been suggested. After determining which pyrolysis ramp rate yielded the highest electrochemically available surface area carbon based on chronoamperometry we tested these same electrodes for their capacitance values as determined from cyclic voltammetry in a voltage region where there are no faradaic reactions. High surface area carbons are known to have complicated kinetics due to the presence of various surface functional groups[123]. These surface groups contain functionalities such as quinoid, quinhydrone, phenolic, carboxyl, carbonyl and lactone depending upon the fabrication technique used for manufacturing the

135

electrodes[124]. As a consequence capacitance measurements employing various characterization techniques often exhibit inconsistencies due to some pseudo capacitance contributions. We have found that, GC electrodes made at very slow ramp rates require a chemical or physical etch for surface area activation before any electrochemical experiment[110,125]. This is most likely due to the very low chemical reactivity of GC electrodes made under very slow ramp rates and in an inert gas atmosphere. We conducted H_2SO_4 washing for surface pre-treatment for all our electrodes before CV experiments. In addition, we investigated the effect on the double layer capacitance of PGC electrodes after this acid pre-treatment, which led to a 1.3 times increase of the capacitance. Further, we evaluated the performances of PGC50 (PGC pyrolyzed at 50°C/min temperature ramp up, electrodes as capacitors at five different potential scan rates. Whereas for the CVs of an ideal electrode, the charging current value remains constant irrespective of potential sweep rate[110], for electrodes with a high degree of roughness such as PGC, it has been reported that the capacitance becomes a function of potential sweep rate[126]. Both fast and slow charging processes coexist in rough electrodes and if a slower potential sweep is applied, the slow charge/discharge processes also contribute to the calculated capacitance[127]. In addition to EDLCs, PGC can be utilized for a range of applications such as adsorbents, molecular sieves, filters and catalyst supports, sensors, electrosorption, and other biomedical devices[128–131]. This material can also serve as a liquid foam model because on specific temperature ramp the bubbles in PGC can be made interconnected.
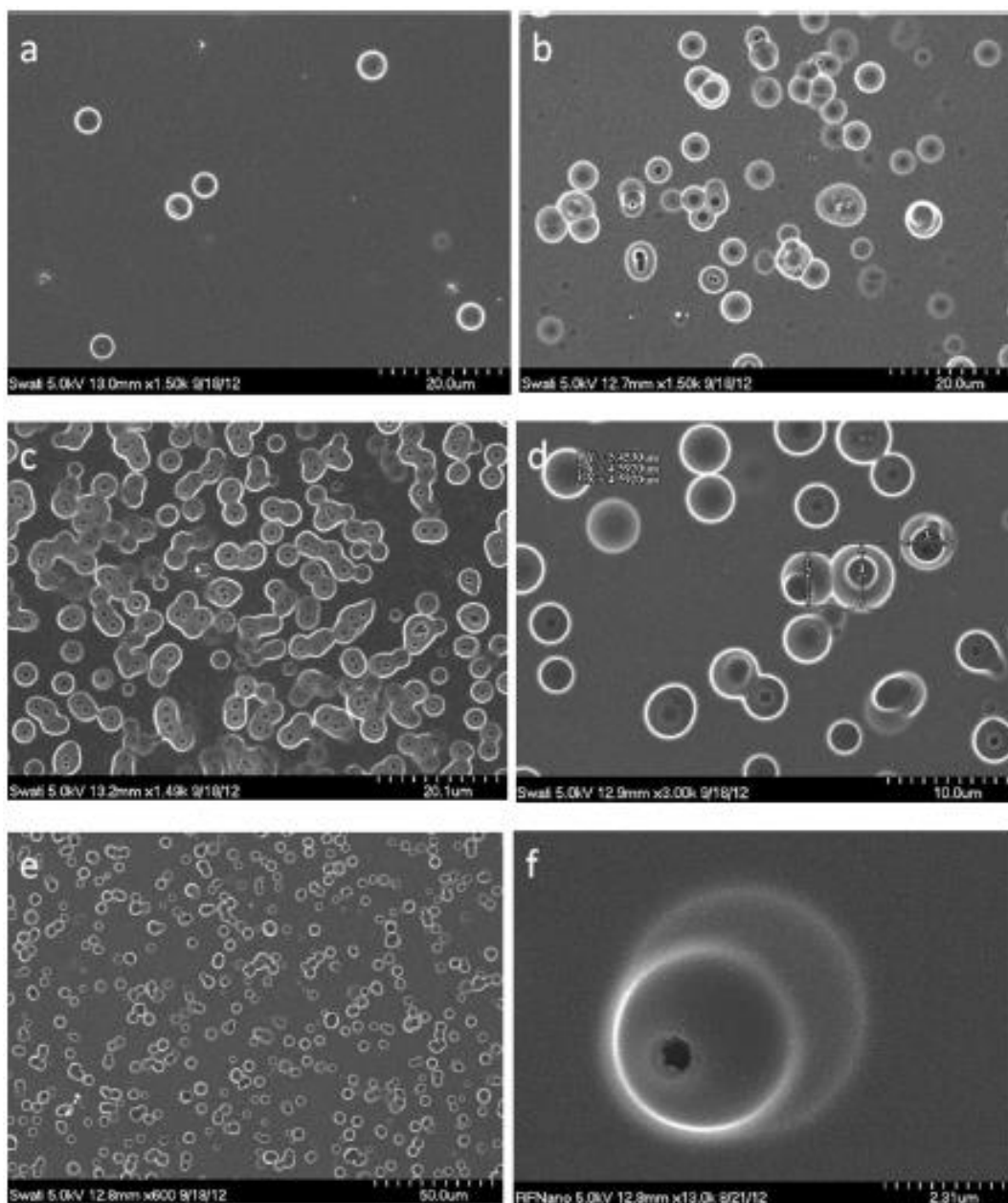
Figure 69: SEM micrographs of (a–c) 3mm × 3mm wide and 30μm high SU-8 derived PGC electrodes pyrolyzed employing rapid pyrolysis of SU-8 at 25, 50 and 75°C/min, respectively. (d) Diameter distribution in carbon electrode pyrolyzed at 50°C/min. (e) Lower magnification image of carbon electrode pyrolyzed at 50°C/min. (f) A single bubble formed during rapid pyrolysis of SU-8. [132]

137

Materials and Methods

We used the same the same carbon MEMS electrodes (Fig. 39) for this study. Details of fabrication and optimization steps are provided in section one of this chapter as well as in the published paper[132].

Electrical resistance tests were carried out on a Dektak XT resistance measurement apparatus. CV and chronoamperomety were carried out on a Gamry potentiostat model PC4 using a three-electrode system in a 0.5M KCl. The auxiliary electrode used was flat GC with $1cm^2$ surface area and the reference electrode was Ag/AgCl in 3M NaCl.

As working electrodes during chronoamperometry we used flat GC (control), PGC25, PGC50 and PGC75 respectively. The area was calculated employing Cottrell equation (explained in next section). For PGC25, PGC50 and PGC75, an area ratio compared to flat GC was determined. PGC50 exhibited the largest electrochemically available surface area; therefore further CV experiments were performed only using PGC50 as the working electrode. CA experiments were carried out in a 10mM $[Fe(CN)_6]^{3-}$ solution in 0.5M KCl (supporting electrolyte) employing a three electrode system same as what we stated above. First, an initial potential of 600mV was applied where no electrochemical reduction of $[Fe(CN)_6]^{3-}$occurs. This was followed by a step potential of 0V where essentially all the $[Fe(CN)_6]^{3-}$ is reduced to $[Fe(CN)_6]^{4-}$. CV on PGC50 was carried out at 5 different potential scan rates:5, 10, 25, 50 and 75 mV/s. All electrodes were washed in a 0.1M H_2SO_4 solution. First 20 cycles of each CV were discarded and the value of the 21st cycle was taken as the data point in order to ensure equilibrium. A set of five different samples for each carbon type (at each scan rate for multiple scan rate CV test) was used for calculating the standard deviation.

Results and discussion

Morphological characterization

Typical SEM micrographs of PGC electrodes fabricated at three different temperature ramp rates (25, 50 and 75°C/min) are illustrated in Fig. 69(a–f). Fig. 2(a–c) are images for PGC25, PGC50 andPGC75, respectively. The average pore diameter for PGC50 as shown in Fig. 69(d) is 5μm. Fig. 69(e) is a lower magnification image of PGC50 that displays better the bubble distribution on a larger electrode surface. The detailed geometry of a bubble can be seen in Fig. 69(f), which is an SEM micrograph of a typical single bubble. GC electrodes carbonized by slow pyrolysis of SU8 tend to have a very flat surface since during photolithography a uniform layer of SU-8 is spin-coated on to the substrate and the slow temperature ramp rate allows all the escaping gases to be annealed out smoothly. During pyrolysis the process temperature is always kept below the glass-transition temperature (Tg) of the carbonizing material in order to maintain the original lithographic pattern intact[133]. The semi-solid material state under such process conditions helps in retaining the high flatness of the surface and results in carbon electrodes with negligible surface roughness, this and the inert processing gas lead to a very un-reactive type of GC surface. However, if the temperature ramp rate is sufficiently fast during pyrolysis and the gases (O and H present in SU-8) are unable to diffuse out towards the resist/air interface, and the gas pockets become "frozen" into the carbon matrix.

Electrical resistance measurements

Flat GC and PGC50 electrodes were characterized for their electrical resistance by four-point probe. The average resistivity of flat GC and PGC50 were 3.63E−04 and 3.78E−04 Ωm,

respectively, which is in accordance with the reported resistivity of polymer derived GC pyrolyzed at 900°C[134].

Chronoamperometry and surface area calculation from the Cottrell equation

The electrochemically accessible area of GC and PGC (25, 50 and75) electrodes was determined employing chronoamperometry. For this experiment we used 10mM $[Fe(CN)_6]^{3-}$ as the active redox species because it is an outer sphere redox species and does not adsorb onto the surface contributing to background currents[106]. In chronoamperometry the current (i) response with respect to time (t), after an applied step potential is given by Cottrell equation (Equation 9) and this expression allows one to obtain the electrode surface area

$$i = nFAC\sqrt{D/\pi t}$$
Equation 9

where i is the current, t is time in seconds, F is the Faraday constant (96,485coulombs), n is the number of electrons transferred (=1 in this case), A is the surface area of the electrode, and C and D are the $[Fe(CN)_6]^{3-}$ concentration and diffusion coefficient (10 mM and1.6 $\times$ $10^{-5}cm^2s^{-1}$) respectively. A plot of i vs. $t^{-1/2}$ transforms the data into a linear relationship with a slope that equals $nFACD^{1/2}\pi^{-1/2}$. The electrochemical surface area A for the PGC50 electrode, which had the largest area of the three PGCs, was calculated from this slope as 0.17cm². The area for PGC25 and PGC75 calculated in the same fashion was 0.11 and 0.12cm², respectively. The geometric area of all electrodes, including flat GC, was 0.07cm² in the latter case the electrochemical area derived from the Cottrell equation was 0.06cm². This means that the PGC50 electrode has three times the electrochemical area of that of a GC electrode of the same geometric surface area. From the above, PGC25 and PGC75

display lower electrochemically accessible surface areas compared to PGC50. For PGC25 a lower area is apparent from the SEM micrographs that show fewer bubbles, however for PGC75 one would have expected to have a yet higher surface area as this electrode come with yet more bubbles. But upon closer observation and more extensive SEM imaging we found that the bubbles formed in PGC75 electrodes tend to minimize their surface area by merging and forming bigger bubbles. The resulting pores in the PGC75 carbon therefore have a lower overall surface area. This phenomenon explains an optimal surface area for the PGC50 samples. The formation during rapid pyrolysis of photo-patterned resists of bubbles with geometries very similar to those of bubbles observed in liquids suggests a semi-solid rubbery state of the matrix, soft enough to allow bubble movement while still retaining the overall morphology of the original patterned polymer. The bubble merging phenomena can be understood from the Laplace–Young law as expressed in equation 10:

$$R = 2\lambda / \Delta p \hspace{4cm} \text{Equation 10}$$

where R is the curvature, λ is the surface tension and Δp is the pressure difference at the interface of a bubble and the matrix it is embedded in. This expression relates the pressure difference at the interface between two fluids to the shape of the surface wall (bubbles in our case). Accordingly, to minimize pressure differences (Δp), small gas bubbles in the SU-8 fluid matrix tend to merge and form bigger bubbles in order to minimize the curvature R.

Effect of H_2SO_4 wash

As mentioned in the introduction we used a H_2SO_4 wash (0.1M H_2SO_4) for all carbon electrodes before CV experiments to ensure reproducibility. In addition, in order to understand the effect of this acid treatment on capacitance, a CV test before and after the acid wash was carried out for PGC50 electrodes. Typical cyclic voltammograms, before and

after acid treatment, are shown in Fig. 70(a). The capacitance of the electrode increased 1.3 times after acid treatment. With H_2SO_4 cleaning of the PGC electrodes, one of the most common chemical pre-treatment methods, one oxidizes the surface leading to more reactive groups that contribute to an added pseudo capacitance by reduction during CV[135].

Comparison of flat and porous GC

We carried out a comparison of PGC50 and flat GC electrodes by CV at 25mV/s potential scan rate, the cyclic voltammograms for which are shown in Fig. 70(b). The electrode and specific capacitance values for flat GC at 25mV/s were found to be 41 and 681µF, respectively. The ratio of the specific capacitance (PGC50/flat GC) was approximately 5, and that of the electrode capacitance was 15.

Capacitance at five different scan rates for PGC50

Having established that carbon electrodes formed at a ramp rate of 50°C/min leads to the largest surface areas (PGC50 electrodes) these electrodes were singled out for further study. The double layer capacitance of GC and PGC50 electrodes was calculated from the capacitance charging current (i_c) in cyclic voltammograms in the potential range where no Faradic reactions occur. Capacitance values from the cyclic voltammograms were determined using the following equation:

$$C = \int_{v_1}^{v_2} \frac{i(v)dv}{v(v_2 - v_1)}$$
Equation 10
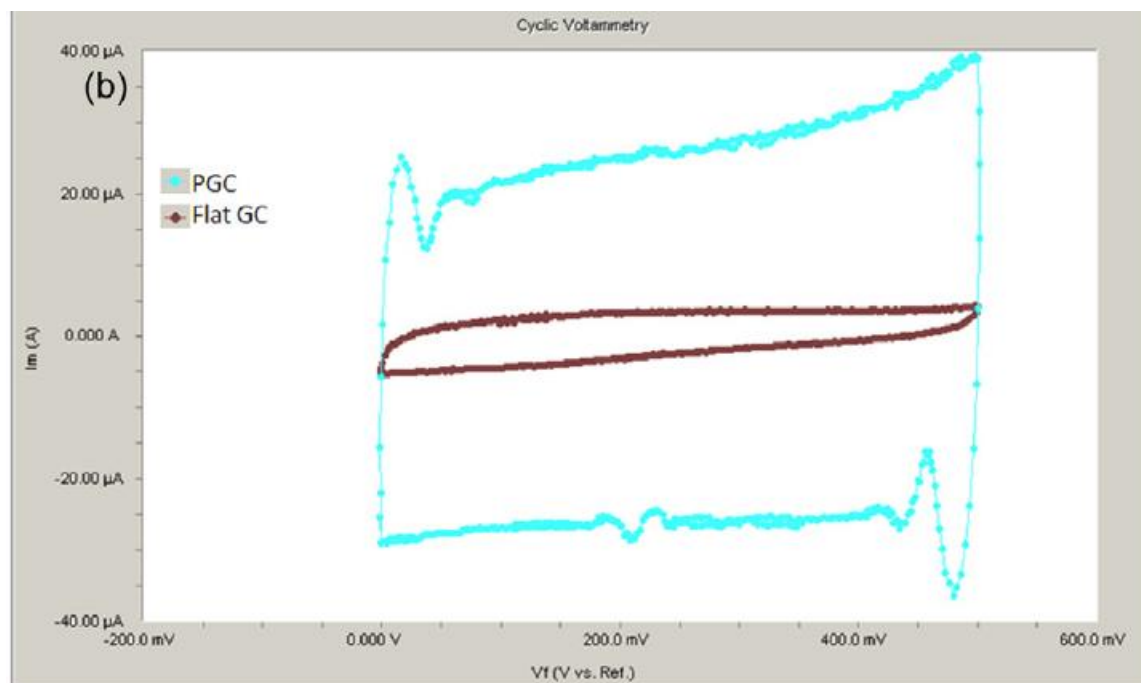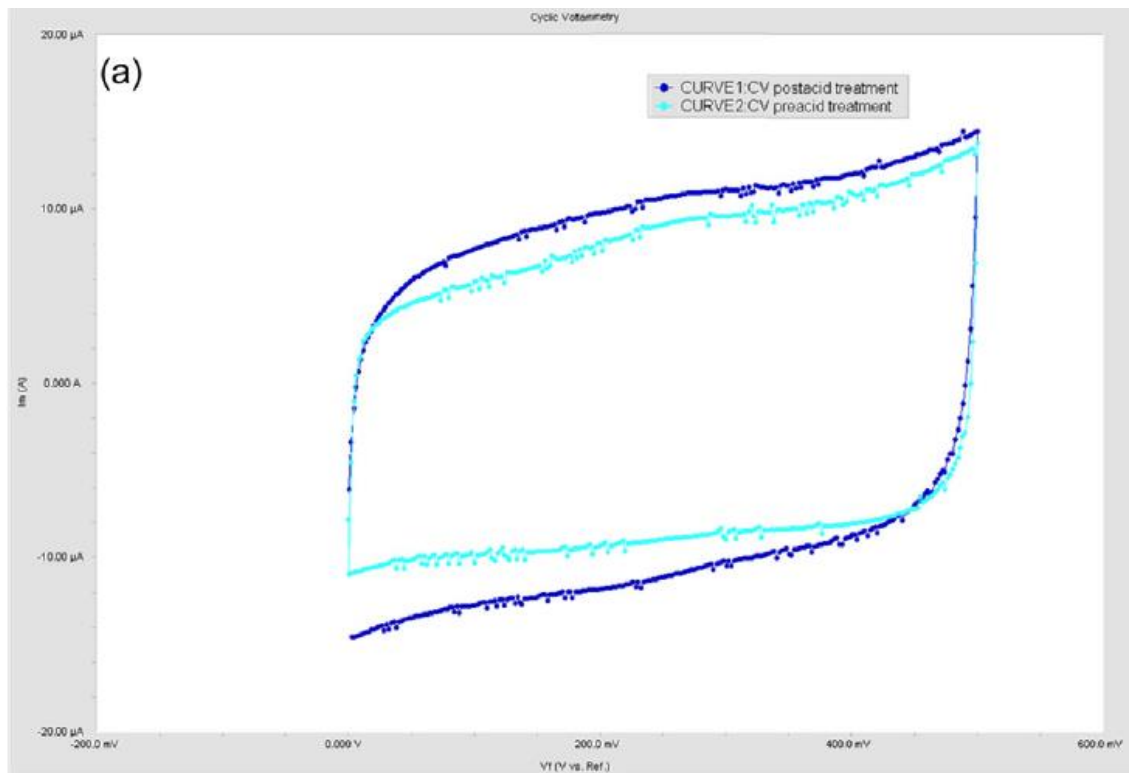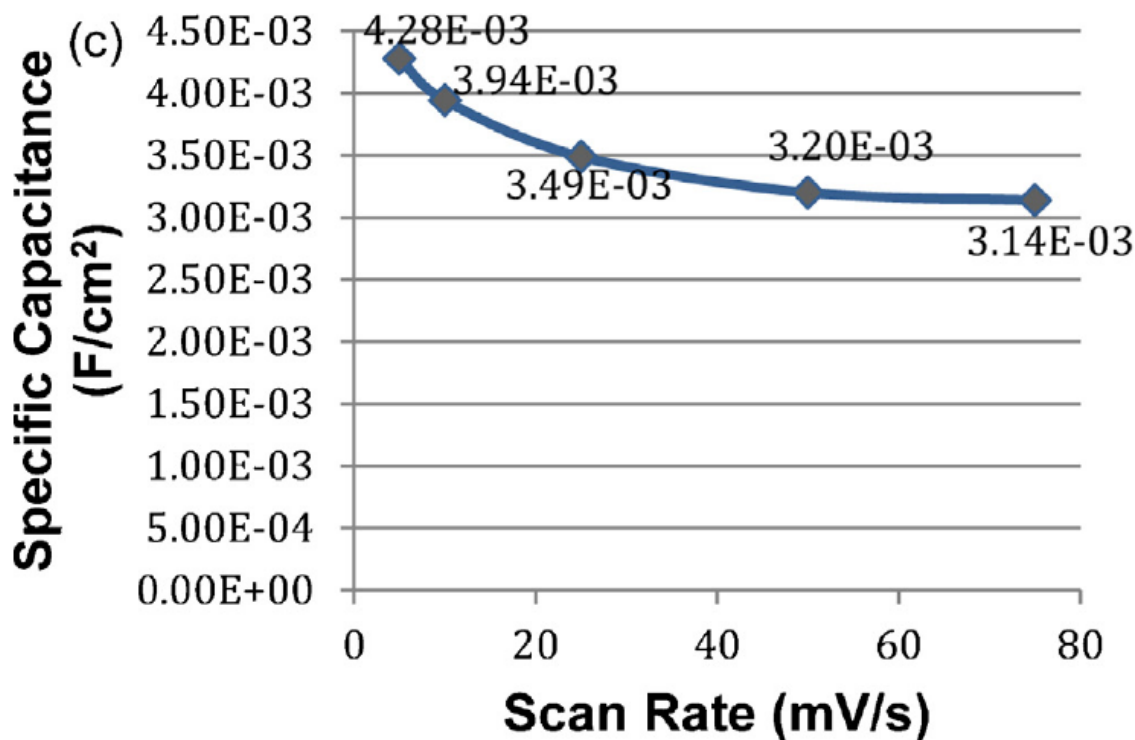
Figure 70: Cyclic voltammograms in 0.1M KCl for PGC50 electrode carbonized by rapid pyrolysis of SU-8 before and after 0.1M acid wash at potential scan rate25 mV/s. (b) Cyclic voltammograms in 0.1M KCl for flat GC and PGC50 electrodes at potential scan rate 25 mV/s. Comparison of specific capacitance of PGC50 electrodes carbonized by rapid pyrolysis of SU-8 in 0.1M KCl at different scan rates.(c) Graphical representation of EDL capacitances measured at various potential scan rates for a PGC50 electrode.[132]

where i (Ampere) is the instantaneous current, V_1 and V_2 (Volt) are switching potentials, and *v* is the scan rate (V/s). For electrodes with a high degree of roughness, it has been reported that the capacitance becomes a function of potential sweep rate[126]. Both fast and slow charging processes co-exist in rough electrodes and if a slower potential sweep is applied, the slow charge/discharge processes also contribute to the calculated capacitance[127]. Accordingly we observe more capacitive charging currents at the lower ramp rates. Electrode and specific capacitance obtained from CVs at potential scan rates of 5, 10, 25, 50 and 75mV/s for PGC50 (after H_2SO_4 washing) are detailed in Table 8.

Table 8: EDL capacitances measured at various potential scan rates for a PGC50 electrode. Specific capacitance values are calculated as (electrode capacitance)/(wetted surface area).[132]

S.No.	Potential Sweep rate (mV/s)	Electrode Capacitance (F)	Specific Capacitance(F/cm^2)
1	5	7.27E-04	4.28E-03
2	10	6.70E-04	3.94E-03
3	25	5.93E-04	3.49E-03
4	50	5.44E-04	3.20E-03
5	75	5.34E-04	3.14E-03

The specific capacitance values are also graphically represented in Fig. 70(c) to illustrate the decreasing trend in the observed specific capacitance when faster potential scan rates are applied to PGC electrodes. To obtain the specific capacitance, electrode capacitance was divided by chronoamperometrically computed surface area (0.17 cm^2 for PGC50 and 0.06 cm^2 for flat GC). As is clear from Table 8 and Fig. 70(c), the specific capacitance values increase with a decrease in the potential scan rate and this change is more significant below 10 mV/s scan rate. The ratio of the capacitance at 5 and 75mV/s is 1.36 for PGC50, which indicates that the contribution of the slow charging processes is not very significant. It is expected however that at yet slower

potential rates the capacitance will further increase. Also, carbon materials display a frequency dependent capacitance known as "frequency dispersion" unlike what is theoretically predicted[136]. The main reasons responsible for such behavior are the fabrication method and precursor used for the manufacture of electrode, insufficient wetting, surface functionalities and the inhomogeneity in size and shape of surface features[124,136].

Reactive ion etch for PGC50

We carried out reactive ion etching (RIE) in oxygen plasma on PGC50 electrodes as RIE has been shown to reveal the under-lying microstructure of GC[137]. Typical SEM micrographs of the etched PGC surface are illustrated in Fig. 71. It can be observed that nano scale features, caused by different etch rates of graphitic and amorphous regions of the GC[137], are present in the bubble impressions as well as in the surrounding flat area. Based on the electrical resistance and the plasma etching behavior described here we conclude that the microstructure of PGC is same as that of SU8 derived GC obtained at slower pyrolysis ramp rates. From the SEM pictures we were also expecting the oxygen plasma etched electrodes to exhibit a much-enhanced capacitance owing to the surface area increase. Unfortunately the results displayed significant variations with time. The nano features on the plasma-etched electrodes could only be captured by electron microscopy when the samples were fresh (within a day after etching). If the electrodes are exposed to air for extended periods, they tend to develop an insulating layer that blocks the electrons during SEM imaging. This suggests that the oxygen plasma etching renders the PGC surface highly reactive by exposing a large number of

reactive graphite edge planes present in GC[124]. We are currently working on further optimization of the thus processed electrodes.
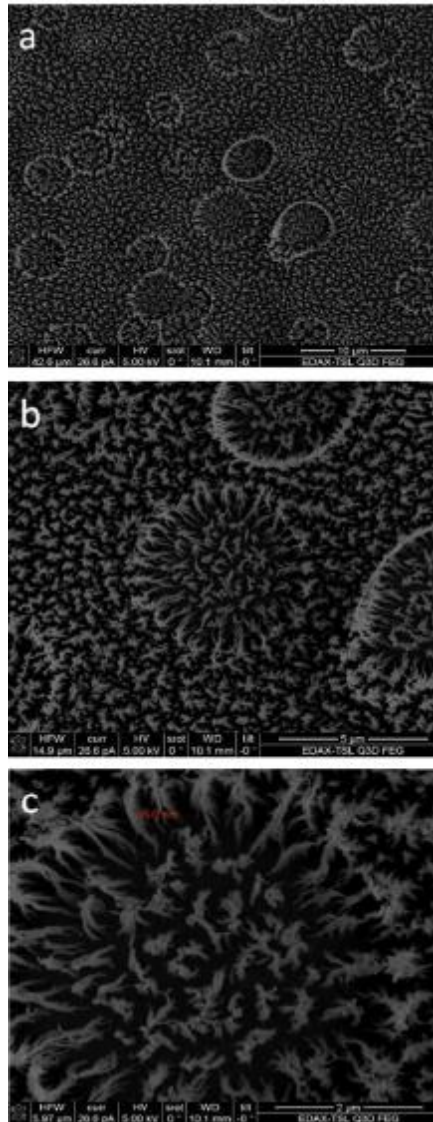
Figure 71: SEM micrographs of oxygen plasma etched PGC at increasing magnification from (a) to (c). [132]

7. Conclusion and Future Work

The goal of this thesis was primarily to optimize fabrication of 3D carbon IDEAs, followed by their electrochemical characterization and finally demonstrating some of its biomedical application. They are summarized as follows:

a. Fabrication

Traditionally the interdigitated electrode array or "comb" arrays are fabricated using multistep process that requires expensive instrumentation/training to pattern the resist followed by metal deposition step and finally the lift off step. More the number of steps higher is the probability of fabrication defect and lower is the yield which in turn, makes them extremely expensive. Moreover, the IDEAs fabricated this way are only planar. To make 3D metal IDEA one needs to add a few more steps as shown in Fig. 6. This way the height of the electrodes can be exploited for further enhancing the redox amplification.

The method described in this thesis, UV patterning to get submicron resolution followed by pyrolysis solves the problems posed by metal IDEAs. The electrodes can offer higher amplification, are much cheaper and simpler to fabricate, this amenable to mass production. For future work we will focus on using deep UV systems to see how far one can go in reducing the gap spacings between IDEAs without compromising on height. We will also explore nano-imprint lithography (NIL) to increase mass production and enhance resolution. Based on replication from a mold (stamp) NIL is based on a simple set-up and because it allows for parallel printing, it is inherently a high throughput and a low cost fabrication process. In NIL, the mold is made up of a hard material (usually Si, Ni or Quartz) using high resolution electron beam lithography or focused ion beam lithography. The

resolution of NIL is a direct function of the resolution of this hard mold. NIL does not involve complicated steps such as lift-off or electroless deposition and once a high-resolution mold has been made that mold can be used over and over again without the need for another expensive high-resolution exposure step. It has been demonstrated that the hard mold templates do not deteriorate even after 1500 imprints with sub-100 nm feature sizes. Fabricating the mold is the only expensive process involved in NIL; however, it's a onetime process. The simplicity of the NIL technique as well as its amenability to rapid fabrication makes it also a very attractive choice for patterning polymer precursors that can be pyrolyzed to produce carbon IDA electrodes.
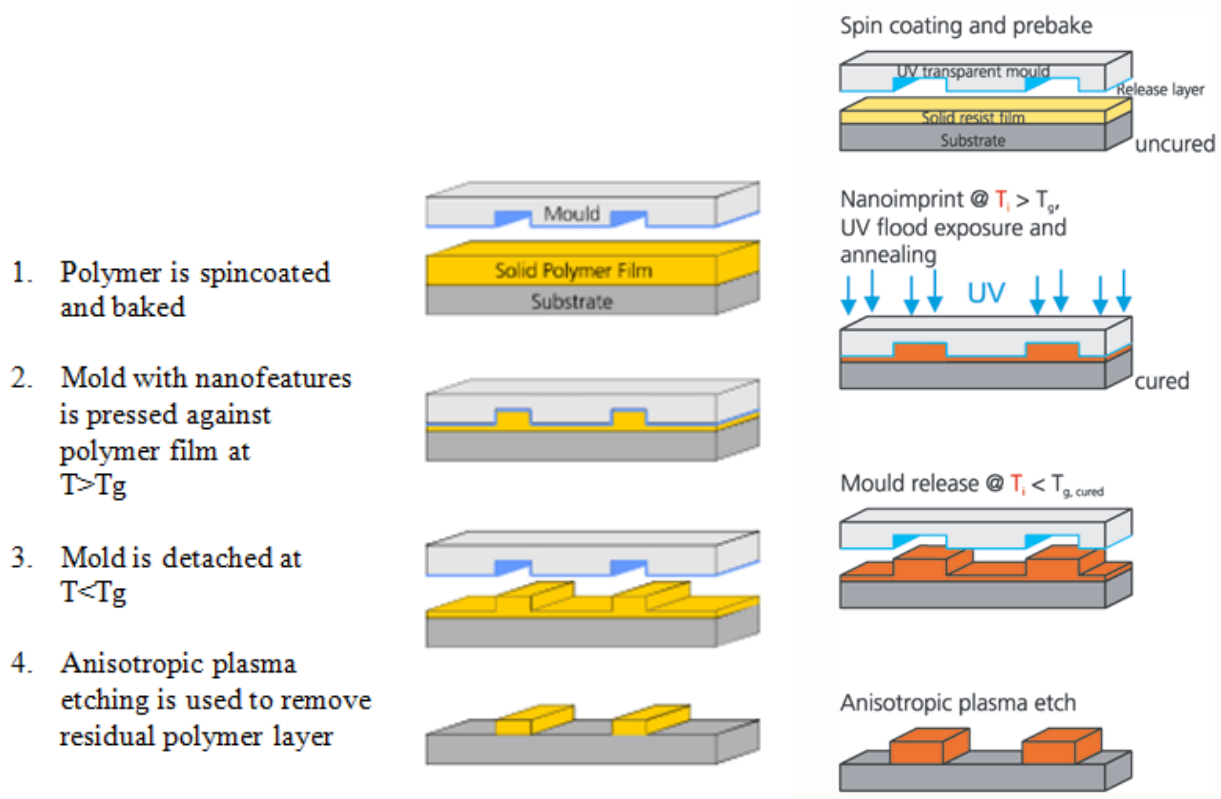
Figure 32: Process flow for thermal NIL (left) and UV based NIL (right). Courtesy: Microresist Technology, GmbH

b.   Electrochemical Characterization

Electrochemical characterization for carbon IDEAs was done extensively for different geometries and its effect on amplification was studied. The effect of potential sweep rate on redox amplification was discussed extensively in this work. Besides, we also found how the shrinkage affects amplification for taller IDEAs. Currently our best electrodes are the ones with the width/gap ratio of 1.58 and height of 1.1μm that provides amplification factor of 37. This factor is half of the maximum amplification factor recorded for the 3D platinum IDEAs i.e., 74 by Dam *et al*. The group used platinum electrodes which had height of 7μm and width of 2μm, gap of 1μm at the top. To achieve amplification similar to the one achieved by Dam *et al,* the height of 3D carbon IDEAs needs to be increased. Predicting the exact height required to achieve a factor of 70 is not intuitive as the amplification does not linearly increase with height for 3D carbon IDEAs. This is mainly because the digit side wall profile varies with different heights. Also, it will require further optimization of photolithography parameters to completely resolve the same gap spacings at higher SU-8 heights, which may be extremely difficult using conventional UV lithography.

Future work on characterization will involve simulation work to find out the effect of flow on redox amplification and collection efficiency for 3D IDEAs with different pyrolyzed side wall profiles, the diffusion flux of redox species at different voltage sweep rate. We would also like to do both experimental and simulation studies to observe the effect of increasing width, keeping gap and the number of digits constant, on increasing the amplification. We speculate the presence of a sweet spot i.e., the amplification will peak or plateau at some width/gap value. We would also like to find out the redox amplification dependence on concentration of the species. Though we haven't done detailed studies on this topic, we

have done enough to observe that amplification peaks at certain concentrations and then drops on either side with concentration change for different species. This effects needs to be investigated better.

c. Demonstrating Biomedical Application for Carbon IDEAs

So far we have demonstrated three biomedical applications. Firstly, a method to selectively determine dopamine in the presence of ascorbic acid at physiological concentrations and pH was demonstrated. The method employed redox cycling of dopamine using 3D carbon IDEAs without any electrode modification using only SDS, a masking agent, at a concentration greater than its critical micellar concentration to achieve a detection limit of 1.5µM. Next, we developed a strategy to selectively amplify neurotransmitters in their mixture without chemically modifying the electrodes or using any masking agent. We were able to achieve low detection limit of 1.3µM for dopamine and 6.3µM for epinephrine. The detection limits can be further lowered using IDEAs with better geometry as described in Chapter 2 and 3. Future work on these projects will involve use of actual biological samples and studying its effects on carbon IDEAs.

Finally, we demostrated the application of carbon IDEAs in electrochemical immunoassay. We found a novel detection scheme using horseradish peroxidase as the enzyme and o-phenelylenediamine as the redox substrate. The susbtrate is converted selectively by thr enzyme into a redox active product that is electroactive and detectable by carbon IDEAs. Using this detection scheme we were able to achieve detection limit as low at 37fM. Future work on this project will integrate electrochemical detection with carbon IDEAs on centrifugal microfluidic platform. The centrifugal microfluidic platform will be able to

automate upto 4-6 immunoassays for different biomarkers on a single disc whereas the carbon IDEAs will quantify the results amperometrically.

8. References

1.   Janata, J. *Principles of Chemical Sensors*. (Springer Open Ltd, 2009).

2.   Coetzee, J. F. Current trends in electrochemical studies of nonaqueous solutions. *Pure Appl. Chem.* **58,** 1091–1104 (1986).

3.   Weigl, B. H., Darling, R. B., Yager, P., Kriebel, J. & Mayes, K. Optical and electrochemical diffusion-based detection of analytes in complex samples using microfabricated flow structures (T-SensorsTM). in *SPIE Proceedings, Microflabricated FLow Syst. Appl. Biol. Biochem. Anal.* **3606,** 82–89 (1999).

4.   Bond, A. M. Past , Present and Future Contributions of Microelectrodes to Analytical Studies Employing Voltammetric Detection. *Analyst* **119,** 1–21 (1994).

5.   Bard, A. J., Faulkner, L. R., Swain, E. & Robey, C. *Electrochemical Methods: Fundamentals and Applications*. 448,813 (John Wiley & Sons, Inc, 2001).

6.   Compton, R. G., Fisher, A. C., Wellington, R. G., Dobson, P. J. & Leigh, P. a. Hydrodynamic voltammetry with microelectrodes: channel microband electrodes; theory and experiment. *J. Phys. Chem.* **97,** 10410–10415 (1993).

7.   Strutwolf, J. & Schorller, W. W. Linear and Cyclic Sweep Voltammetry at a Rotating Disk Electrode . A Digital Simulation. *Electroanalysis* **8,** 1034–1039 (1996).

8.   Bratov, A., Abramova, N., Marco, M. P. & Sanchez-Baeza, F. Three-Dimensional Interdigitated Electrode Array as a Tool for Surface Reactions Registration. *Electroanalysis* **24,** 69–75 (2012).

9.   Sheppard, N. F., Tucker, R. C. & Wu, C. Electrical Conductivity Measurements Using Microfabricated Interdigitated Electrodes. *Anal. Chem.* **65,** 1199–1202 (1993).

10.   Ahadian, S. *et al.* Interdigitated array of Pt electrodes for electrical stimulation and engineering of aligned muscle tissue. *Lab Chip* **12,** 3491–503 (2012).

11.   Sun, T., Morgan, H. & Green, N. Analytical solutions of ac electrokinetics in interdigitated electrode arrays: Electric field, dielectrophoretic and traveling-wave dielectrophoretic forces. *Phys. Rev. E* **76,** 046610 (2007).

12.   Aoki, K. Theory of Ultramicroelectrodes. *Electroanalysis* **5,** 627–639 (1993).

13.   Aoki, K. Approximate models of interdigitated array electrodes for evaluating steady-state currents. *J. Electroanal. Chem. Interfacial Electrochem.* **284,** 35–42 (1990).

14.   Iwasaki, Y. & Morita, M. Electrochemical Measurements with Interdigitated Array Microelectrodes. *Curr. Sep.* **1,** 2–8 (1995).

15.   Niwa, O., Morita, M. & Tabei, H. Highly sensitive and selective voltammetric detection of dopamine with vertically separated interdigitated array electrodes. *Electroanalysis* **3,** 163–168 (1991).

16.   Niwa, O. Electroanalysis with Interdigitated Array Microelectrodes. *Electroanalysis* 606–613 (1995).

17.   Niwa, O., Morita, M. & Tabei, H. Electrochemical behavior of reversible redox species at interdigitated array electrodes with different geometries: consideration of redox cycling and collection. *Anal. Chem.* **175,** 447–452 (1990).

18.   Rahimi, M. & Mikkelsen, S. R. Cyclic biamperometry at micro-interdigitated electrodes. *Anal. Chem.* **83,** 7555–9 (2011).

19.   Jin, P. *et al.* Glucose sensing based on interdigitated array microelectrode. *Anal. Sci.* **17,** 841–6 (2001).

20.   Dam, V. a T., Olthuis, W. & van den Berg, a. Redox cycling with facing interdigitated array electrodes as a method for selective detection of redox species. *Analyst* **132,** 365–70 (2007).

21.   Martinez-Duarte, R. SU-8 Photolithography as a Toolbox for Carbon MEMS. *Micromachines* **5,** 766–782 (2014).

22.   Keller, S., Blagoi, G., Lillemose, M., Haefliger, D. & Boisen, A. Processing of thin SU-8 films. *J. Micromechanics Microengineering* **18,** 125020 (2008).

23.   Zaouk, R. B. Carbon MEMS from the nanoscale to the macroscale: Novel fabrication techniques and applications in electrochemistry. *ProQuest Diss. Theses* 204 (2008). at <http://search.proquest.com/docview/304660195?accountid=14509>

24.   Sharma, S. Microstructural Tuning of Glassy Carbon for Electrical and Electrochemical Sensor Applications. *ProQuest Diss. Theses* 236 (2013). at <http://search.proquest.com/docview/1476199980?accountid=14509>

25.   Mardegan, A. *et al.* Optimization of Carbon Electrodes Derived from Epoxy-based Photoresist. *J. Electrochem. Soc.* **160,** B132–B137 (2013).

26.   Martinez-Duarte, R., Renaud, P. & Madou, M. J. A novel approach to dielectrophoresis using carbon electrodes. *Electrophoresis* **32,** 2385–92 (2011).

27. Odijk, M., Olthuis, W., Dam, V. a. T. & van den Berg, a. Simulation of Redox-Cycling Phenomena at Interdigitated Array (IDA) Electrodes: Amplification and Selectivity. *Electroanalysis* **20,** 463–468 (2008).

28. Iwasaki, Y. & Morita, M. Electrochemical Measurements with Interdigitated Array Microelectrodes. *Curr. Sep.* 2–8 (1995).

29. Aoki, K. Quantitative analysis of reversible diffusion-Connolly currents of redox soluble species at interdigitated array electrodes under steady-state conditions. *J. Electroanal. Chem.* **256,** 269–282 (1988).

30. Tomčík, P. Microelectrode arrays with overlapped diffusion layers as electroanalytical detectors: theory and basic applications. *Sensors (Basel).* **13,** 13659–84 (2013).

31. Stulik, K., Amatore, C., Holub, K., Marecek, V. & Kutner, W. Ł. O. MICROELECTRODES . DEFINITIONS , CHARACTERIZATION , AND APPLICATIONS. *Pure Appl. Chem.* **72,** 1483–1492 (2000).

32. Zanello, P. *Inorganic Electrochemistry: Theory, Practice, and Application*. 606 (Royal Society of Chemistry, 2003).

33. Heo, J. I. *et al.* Carbon Interdigitated Array Nanoelectrodes for Electrochemical Applications. *J. Electrochem. Soc.* **158,** J76 (2011).

34. Kim, S. K. *et al.* Fabrication of comb interdigitated electrodes array (IDA) for a microbead-based electrochemical assay system. *Biosens. Bioelectron.* **20,** 887–894 (2004).

35. Takahashi, M., Morita, M., Niwa, O. & Tabei, H. Highly sensitive high-performance liquid chromatography detection of catecholamine with interdigitated array microelectrodes. *J. Electroanal. Chem.* **335,** 253–263 (1992).

36. Takahashi, M., Morita, M., Niwa, O. & Tabei, H. Highly sensitive detection of catecholamine with interdigitated microelectrodes in HPLC. *Sensors (Basel).* **14,** 336–339 (1993).

37. Bjorefors, F., Standman, C. & Nyholm, L. Electrochemical Detection Based on Redox Cycling Using Interdigitated Microarray Electrodes at uL/min Flow Rates. *Electroanalysis* **12,** 255–261 (2000).

38. Niwa, O. & Morita, M. Carbon Film-Based Interdigitated Ring Array Electrodes as Detectors in Radial Flow Cells. *Anal. Chem.* 355–359 (1996).

39.   Alden, J. A. & Compton, R. G. The multigrid method, MGD 1: an efficient and stable approach to electrochemical modelling. The simulation of double electrode problems. *J. Electroanal. Chem.* **415,** 1–12 (1996).

40.   Damier, P., Hirsch, E. C., Agid, Y. & Graybiel, A. M. The substantia nigra of the human brain: II. Patterns of loss of dopamine-containing neurons in Parkinson's disease . *Brain* **122 ,** 1437–1448 (1999).

41.   Castellano, C., Cabib, S. & Puglisi-Allegra, S. Psychopharmacology of memory modulation: Evidence for multiple interaction among neurotransmitters and hormones. *Behav. Brain Res.* **77,** 1–21 (1996).

42.   Berridge, K. C. & Robinson, T. E. What is the role of dopamine in reward: hedonic impact, reward learning, or incentive salience? *Brain Res. Rev.* **28,** 309–369 (1998).

43.   Wise, R. A. Drug-activation of brain reward pathways. *Drug Alcohol Depend.* **51,** 13–22 (1998).

44.   Wightman, R. M., May, L. J. & Michael, A. C. Detection of Dopamine Dynamics in the Brain. *Anal. Chem.* **60,** 769A–793A (1988).

45.   Bibb, J. A. *et al.* Severe deficiencies in dopamine signaling in presymptomatic Huntington's disease mice. *Proc. Natl. Acad. Sci.* **97,** 6809–6814 (2000).

46.   Mink, J. W. Basal ganglia dysfunction in Tourette's syndrome: a new hypothesis. *Pediatr. Neurol.* **25,** 190–198 (2001).

47.   Grace, A. A. Phasic versus tonic dopamine release and the modulation of dopamine system responsivity: a hypothesis for the etiology of schizophrenia. *Neuroscience* **41,** 1–24 (1991).

48.   Phillips, P. E. M., Stuber, G. D., Heien, M. L. A. V, Wightman, R. M. & Carelli, R. M. Subsecond dopamine release promotes cocaine seeking. *Nature* **422,** 614–618 (2003).

49.   Stokes, A. H., Hastings, T. G. & Vrana, K. E. Mini-Review Cytotoxic and Genotoxic Potential of Dopamine. *J. Neurosci. Res.* **665,** 659–665 (1999).

50.   Santiago-López, D., Bautista-Martínez, J. a, Reyes-Hernandez, C. I., Aguilar-Martínez, M. & Rivas-Arancibia, S. Oxidative stress, progressive damage in the substantia nigra and plasma dopamine oxidation, in rats chronically exposed to ozone. *Toxicol. Lett.* **197,** 193–200 (2010).

51.   Bisaglia, M., Soriano, M. E., Arduini, I., Mammi, S. & Bubacco, L. Molecular characterization of dopamine-derived quinones reactivity toward NADH and

glutathione: implications for mitochondrial dysfunction in Parkinson disease. *Biochim. Biophys. Acta* **1802,** 699–706 (2010).

52. áO'Neill, R. D. Microvoltammetric techniques and sensors for monitoring neurochemical dynamics in vivo. A review. *Analyst* **119,** 767–779 (1994).

53. Robinson, D. L., Hermans, A., Seipel, A. T. & Wightman, R. M. Monitoring rapid chemical communication in the brain. *Chem. Rev.* **108,** 2554–2584 (2008).

54. Yogeswaran, U. & Chen, S.-M. Separation and concentration effect of< i> f</i>-MWCNTs on electrocatalytic responses of ascorbic acid, dopamine and uric acid at< i> f</i>-MWCNTs incorporated with poly (neutral red) composite films. *Electrochim. Acta* **52,** 5985–5996 (2007).

55. Zhang, L. & Jiang, X. Attachment of gold nanoparticles to glassy carbon electrode and its application for the voltammetric resolution of ascorbic acid and dopamine. *J. Electroanal. Chem.* **583,** 292–299 (2005).

56. JIANG, L., LIU, C., JIANG, L., PENG, Z. & LU, G. A chitosan-multiwall carbon nanotube modified electrode for simultaneous detection of dopamine and ascorbic acid. *Anal. Sci.* **20,** 1055–1059 (2004).

57. Adams, R. N., Conti, J., Marsden, C. A. & Strope, E. Measurement of dopamine and 5-hydroxytryptamine release in CNS of freely moving unanesthetized rats. *Br J Pharmacol* **64,** P470–P471 (1978).

58. Hoffman, A. F. & Gerhardt, G. A. In Vivo Electrochemical Studies of Dopamine Clearance in the Rat Substantia Nigra: Effects of Locally Applied Uptake Inhibitors and Unilateral 6-Hydroxydopamine Lesions. *J. Neurochem.* **70,** 179–189 (1998).

59. Niwa, O., Morita, M. & Tabei, N. Highly Selective Electrochemical Detection of Dopamine Using lnterdigitated Array Electrodes Modified with Nafion / Polyester lonomer Layered Film. **6,** 237–243 (1994).

60. Aggarwal, A., Hu, M. & Fritsch, I. Detection of dopamine in the presence of excess ascorbic acid at physiological concentrations through redox cycling at an unmodified microelectrode array. *Anal. Bioanal. Chem.* **405,** 3859–69 (2013).

61. Vandaveer, W. R., Woodward, D. J. & Fritsch, I. Redox cycling measurements of a model compound and dopamine in ultrasmall volumes with a self-contained microcavity device. *Electrochim. Acta* **48,** 3341–3348 (2003).

62. Alarcón-Angeles, G. *et al.* Selective electrochemical determination of dopamine in the presence of ascorbic acid using sodium dodecyl sulfate micelles as masking agent. *Electrochim. Acta* **53,** 3013–3020 (2008).

63. Aggarwal, A., Hu, M. & Fritsch, I. Detection of dopamine in the presence of excess ascorbic acid at physiological concentrations through redox cycling at an unmodified microelectrode array. *Anal. Bioanal. Chem.* **405,** 3859–69 (2013).

64. Elam, M. & Grassi, G. Adrenaline and hypertension : new evidence for a guilty verdict ? *J. Hypertens.* **18,** 675–677 (2000).

65. Berkin, K. E., Thomson, N. C., Inglis, G. C. & Ball, S. G. AIRWAY RESPONSES TO LOW CONCENTRATIONS OF ADRENALINE AND NORADRENALINE IN NORMAL SUBJECTS. *Q. J. Exp. Physiol.* **70,** 203–209 (1985).

66. Cincotto, F. H., Canevari, T. C., Campos, A. M., Landers, R. & Machado, S. a S. Simultaneous determination of epinephrine and dopamine by electrochemical reduction on the hybrid material SiO_2/graphene oxide decorated with Ag nanoparticles. *Analyst* **139,** 4634–40 (2014).

67. Figueiredo-Filho, L. C. S., Silva, T. a, Vicentini, F. C. & Fatibello-Filho, O. Simultaneous voltammetric determination of dopamine and epinephrine in human body fluid samples using a glassy carbon electrode modified with nickel oxide nanoparticles and carbon nanotubes within a dihexadecylphosphate film. *Analyst* **139,** 2842–9 (2014).

68. Kang, J., Yin, X.-B., Yang, X. & Wang, E. Electrochemiluminescence quenching as an indirect method for detection of dopamine and epinephrine with capillary electrophoresis. *Electrophoresis* **26,** 1732–6 (2005).

69. Warnoff, M. Simultaneous Determination of Norepinephrine, Dopamine, 5-Hydroxytryptamine and their Main Metabolites in Rat Brain using High-Perfirmance Liquid Chromatography with Electrochemical Detection. *J. Chromatogr. B Biomed. Sci. Appl.* **307,** 271–281 (1984).

70. Deftereos, N. T., Calokerinost, A. C. & Efstathiou, C. E. Flow Injection Chemiluminometric Determination of Epinephrine, Norepinephrine, Dopamine and L-Dopa. *Analyst* **118,** 627–632 (1993).

71. Thorré, K., Pravda, M., Sarre, S., Ebinger, G. & Michotte, Y. New antioxidant mixture for long term stability of serotonin, dopamine and their metabolites in automated microbore liquid chromatography with dual electrochemical detection. *J. Chromatogr. B Biomed. Sci. Appl.* **694,** 297–303 (1997).

72. Meririnne, E., Ariniemi, K. & Seppala, T. Oxalic acid stabilizes dopamine , serotonin , and their metabolites in automated liquid chromatography with electrochemical detection. *J. Chromatogr. B Biomed. Sci. Appl.* **753,** 413–419 (2001).

73. Pradhan, T. *et al.* Chemical sensing of neurotransmitters. *Chem. Soc. Rev.* **43,** 4684–713 (2014).

74. Porstmann, T. & Kiessig, S. T. Enzyme immunoassay techniques an overview. *J. Immunol. Methods* **150,** 5–21 (1992).

75. Jackson, T. M. & Ekins, R. P. Theoretical limitations on immunoassay sensitivity: Current practice and potential advantages of fluorescent Eu3+ chelates as non-radioisotopic tracers. *J. Immunol. Methods* **87,** 13–20 (1986).

76. Schweitzer, B. *et al.* Immunoassays with rolling circle DNA amplification: A versatile platform for ultrasensitive antigen detection. *Proc. Natl. Acad. Sci.* **97 ,** 10113–10119 (2000).

77. Yu, H. Comparative studies of magnetic particle-based solid phase fluorogenic and electrochemiluminescent immunoassay. *J. Immunol. Methods* **218,** 1–8 (1998).

78. Hirsch, L. *et al.* Metal Nanoshells. *Ann. Biomed. Eng.* **34,** 15–22 (2006).

79. Yasukawa, T., Yoshimoto, Y., Goto, T. & Mizutani, F. Highly-sensitive electrochemical immunosensing method based on dual amplification systems. *Biosens. Bioelectron.* **37,** 19–23 (2012).

80. Dijksma, M. & Bennekom, W. P. Van. Direct Electrochemical Immunosensors - Review A. 5–30

81. Lin, J., Wei, Z. & Mao, C. A label-free immunosensor based on modified mesoporous silica for simultaneous determination of tumor markers. *Biosens. Bioelectron.* **29,** 40–5 (2011).

82. Simon, D. *et al.* Two-site direct immunoassay specific for active renin. *Clin. Chem.* **38 ,** 1959–1962 (1992).

83. Kanda, V., Kariuki, J. K., Harrison, D. J. & McDermott, M. T. Label-Free Reading of Microarray-Based Immunoassays with Surface Plasmon Resonance Imaging. *Anal. Chem.* **76,** 7257–7262 (2004).

84. Warsinke, A., Benkert, A. & Scheller, F. W. Electrochemical immunoassays. *Fresenius. J. Anal. Chem.* **366,** 622–634 (2000).

85. Niwa, O., Xu, Y., Halsall, H. B. & Heineman, W. R. Small-Volume Voltammetric Detection of 4-Aminophenol with Interdigitated Array Electrodes and Its Application to Electrochemical Enzyme Immunoassay. **V,** 1559–1563 (1993).

86. Niu, S. Y., Zhang, S. S., Ma, L. B. & Jiao, K. Electrochemical and Spectroscopic Studies on the Interaction between DNA and the Product of Enzyme-catalyzed Reaction of OPD-H2O2 -HRP. *Bull. Korean Chem. Soc.* **25,** 829–832 (2004).

87. Sun, W., Jiao, K. & Zhang, S.-S. Comparison of Electrochemical and Spectro-Photometric Detection in Hrp-Based Elisa for Tobacco Mosaic Virus. *Anal. Lett.* **33,** 2653–2675 (2000).

88. Volpe, G., Compagnone, D., Draisci, R. & Palleschi, G. 3,3',5,5'-Tetramethylbenzidine as electrochemical substrate for horseradish peroxidase based enzyme immunoassays . A comparative study. *ANa* **123,** 1303–1307 (1998).

89. Sun, W., Jiao, K., Zhang, S., Zhang, C. & Zhang, Z. Electrochemical detection for horseradish peroxidase-based enzyme immunoassay using p -aminophenol as substrate and its application in detection of plant virus. **434,** 43–50 (2001).

90. Lyon, J. L. & Stevenson, K. J. Picomolar peroxide detection using a chemically activated redox mediator and square wave voltammetry. *Anal. Chem.* **78,** 8518–25 (2006).

91. Tang, H., Lunte, C. E., Halsall, H. B. & Heineman, W. R. p-Aminophenyl Phophate: An Improved Susbtrate For Electrochemical Enzyme ImmunoAssay. *Anal. Chim. Acta* **214,** 187–195 (1988).

92. Bauer, C. G. *et al.* Zeptomole-Detecting Biosensor for Alkaline Phosphatase in an Electrochemical Immunoassay for 2 , 4-Dichlorophenoxyacetic acid. *Anal. Chem.* **68,** 2453–2458 (1996).

93. Fanjul-Bolado, P., González-García, M. B. & Costa-García, A. Flow screen-printed amperometric detection of p-nitrophenol in alkaline phosphatase-based assays. *Anal. Bioanal. Chem.* **385,** 1202–8 (2006).

94. Niwa, O., Xu, Y., Halsall, H. B. & Heineman, W. R. Small-volume voltammetric detection of 4-aminophenol with interdigitated array electrodes and its application to electrochemical enzyme immunoassay. *Anal. Chem.* **65,** 1559–63 (1993).

95. Kim, S. K. *et al.* Fabrication of comb interdigitated electrodes array (IDA) for a microbead-based electrochemical assay system. *Biosens. Bioelectron.* **20,** 887–94 (2004).

96. Naseri, A. Cheap and easy modification of glassy carbon electrode for voltammetric determination of dopamine in the presence of ascorbic acid. *DARU* **19,** 270–276 (2011).

97. Chen, I.-J. & White, I. M. High-sensitivity electrochemical enzyme-linked assay on a microfluidic interdigitated microelectrode. *Biosens. Bioelectron.* **26,** 4375–81 (2011).

98. Sharma, S., Sharma, A., Cho, Y.-K. & Madou, M. Increased graphitization in electrospun single suspended carbon nanowires integrated with carbon-MEMS and carbon-NEMS platforms. *ACS Appl. Mater. Interfaces* **4,** 34–9 (2012).

99. Madou, G. T. T. and R. A. G. I. I. I. and P. P. T. and G. S. B. and M. K. and T. K. M. and T. K. B. and J. R. S. and A. S. and B. Y. P. and M. Carbon microelectromechanical systems as a substratum for cell growth. *Biomed. Mater.* **3,** 34116 (2008).

100. Lee, J. a *et al.* An electrochemical impedance biosensor with aptamer-modified pyrolyzed carbon electrode for label-free protein detection. *Sensors Actuators B Chem.* **129,** 372–379 (2008).

101. Zachek, M. K., Takmakov, P., Moody, B., Wightman, R. M. & McCarty, G. S. Simultaneous Decoupled Detection of Dopamine and Oxygen Using Pyrolyzed Carbon Microarrays and Fast-Scan Cyclic Voltammetry. *Anal. Chem.* **81,** 6258–6265 (2009).

102. Wang, C. & Madou, M. From MEMS to NEMS with carbon. *Biosens. Bioelectron.* **20,** 2181–2187 (2005).

103. Ranganathan, S., McCreery, R., Majji, S. M. & Madou, M. Photoresist-Derived Carbon for Microelectromechanical Systems and Electrochemical Applications. *J. Electrochem. Soc.* **147,** 277 (2000).

104. Kim, J., Song, X., Kinoshita, K., Madou, M. & White, R. Electrochemical Studies of Carbon Films from Pyrolyzed Photoresist. *J. Electrochem. Soc.* **145 ,** 2314–2319 (1998).

105. Wang, Y., Alsmeyer, D. C. & McCreery, R. L. Raman spectroscopy of carbon materials: structural basis of observed spectra. *Chem. Mater.* **2,** 557–563 (1990).

106. McCreery, R. L. Advanced carbon electrode materials for molecular electrochemistry. *Chem. Rev.* **108,** 2646–87 (2008).

107. Binsheng, L. & Peichang, L. Correction method for quantitative area determination of overlapping chromatographic peaks based on the exponentially modified Gaussian (EMG) model. *J. High Resolut. Chromatogr.* **10,** 449–454 (1987).

108. Zhao, J., Yang, L., Li, F., Yu, R. & Jin, C. Structural evolution in the graphitization process of activated carbon by high-pressure sintering. *Carbon N. Y.* **47,** 744–751 (2009).

109. Jenkins, G. & Kawamura, K. *Polymeric Carbons – Carbon Fibre, Glass and Char*. (Cambridge University Press, 1976).

110. Kinoshita, K. *Carbon Electrochemical and Pysico-chemical Properties*. (John Wiley & Sons, Inc, 1988).

111. IUPAC. in *Compend. Chem. Terminol.* 493 (1997).

112. Beriet, C. & Pletcher, D. A microelectrode study of the mechanism and kinetics of the ferro/ferricyanide couple in aqueous media: The influence of the electrolyte and its concentration. *J. Electroanal. Chem.* **361,** 93–101 (1993).

113. Kielland, J. Individual Activity Coefficients of Ions in Aqueous Solutions. *J. Am. Chem. Soc.* **59,** 1675–1678 (1937).

114. Brunetti, B., Ugo, P., Moretto, L. M. & Martin, C. R. Electrochemistry of phenothiazine and methylviologen biosensor electron-transfer mediators at nanoelectrode ensembles. *J. Electroanal. Chem.* **491,** 166–174 (2000).

115. Wang, J., Luo, D.-B. & Horiuchi, T. Anodic Stripping with Collection at Interdigitated Carbon Film Microelectrode Arrays. *Electroanalysis* **10,** 107–110 (1998).

116. Hutton, E. A., Ogorevc, B., Hočevar, S. B. & Smyth, M. R. Bismuth film microelectrode for direct voltammetric measurement of trace cobalt and nickel in some simulated and real body fluid samples. *Anal. Chim. Acta* **557,** 57–63 (2006).

117. Economou, A. Bismuth-film electrodes: recent developments and potentialities for electroanalysis. *TrAC Trends Anal. Chem.* **24,** 334–340 (2005).

118. Arduini, F., Calvo, J. Q., Palleschi, G., Moscone, D. & Amine, A. Bismuth-modified electrodes for lead detection. *TrAC Trends Anal. Chem.* **29,** 1295–1304 (2010).

119. Mardegan, A. *et al.* Speciation of Trace Levels of Chromium with Bismuth Modified Pyrolyzed Photoresist Carbon Electrodes. *Electroanalysis* n/a–n/a (2014). doi:10.1002/elan.201400392

120. Jorge, E. O., Rocha, M. M., Fonseca, I. T. E. & Neto, M. M. M. Studies on the stripping voltammetric determination and speciation of chromium at a rotating-disc bismuth film electrode. *Talanta* **81,** 556–564 (2010).

121. Pifferi, V. *et al.* Electrodeposited nano-titania films for photocatalytic Cr(VI) reduction. *Catal. Today* **209,** 8–12 (2013).

122. Chatzitheodorou, E., Economou, A. & Voulgaropoulos, A. Trace Determination of Chromium by Square-Wave Adsorptive Stripping Voltammetry on Bismuth Film Electrodes. *Electroanalysis* **16,** 1745–1754 (2004).

123. Qu, D. & Shi, H. Studies of activated carbons used in double-layer capacitors. *J. Power Sources* **74,** 99–107 (1998).

124. Qu, D. Studies of the activated carbons used in double-layer supercapacitors. *J. Power Sources* **109,** 403–411 (2002).

125. Frackowiak, E. Carbon materials for supercapacitor application. *Phys. Chem. Chem. Phys.* **9,** 1774–1785 (2007).

126. Gagnon, E. G. The Triangular Voltage Sweep Method for Determining Double-Layer Capacity of Porous Electrodes: IV . Porous Carbon in Potassium Hydroxide . *J. Electrochem. Soc.* **122 ,** 521–525 (1975).

127. Oren, Y. & Soffer, A. The electrical double layer of carbon and graphite electrodes: Part II. Fast and slow charging processes. *J. Electroanal. Chem. Interfacial Electrochem.* **186,** 63–77 (1985).

128. Stein, A., Wang, Z. & Fierke, M. A. Functionalization of Porous Carbon Materials with Designed Pore Architecture. *Adv. Mater.* **21,** 265–293 (2009).

129. Navarro, M. V, Seaton, N. A., Mastral, A. M. & Murillo, R. Analysis of the evolution of the pore size distribution and the pore network connectivity of a porous carbon during activation. *Carbon N. Y.* **44,** 2281–2288 (2006).

130. Liang, Y. *et al.* An advanced carbonaceous porous network for high-performance organic electrolyte supercapacitors. *J. Mater. Chem. A* **1,** 7000–7005 (2013).

131. Villar, I. *et al.* Carbon materials as electrodes for electrosorption of NaCl in aqueous solutions. *Adsorption* **17,** 467–471 (2011).

132. Sharma, S., Kamath, R. & Madou, M. Porous glassy carbon formed by rapid pyrolysis of phenol-formaldehyde resins and its performance as electrode material for electrochemical double layer capacitors. *J. Anal. Appl. Pyrolysis* **108,** 12–18 (2014).

133. Ehrburger, P., Martin, C. & Saint-Romain, J. L. Glass transition and enthalpy relaxation process in coal tar pitches. *Fuel* **70,** 783–788 (1991).

134. Schueller, O. J. A., Brittain, S. T., Marzolin, C. & Whitesides, G. M. Fabrication and Characterization of Glassy Carbon. **4756,** 1399–1406 (1997).

135. Engstrom, R. C. & Strasser, V. A. Characterization of electrochemically pretreated glassy carbon electrodes. *Anal. Chem.* **56,** 136–141 (1984).

136. Permann, L., Lätt, M., Leis, J. & Arulepp, M. Electrical double layer characteristics of nanoporous carbon derived from titanium carbide. *Electrochim. Acta* **51,** 1274–1281 (2006).

137. Maeda, S.-W. Y. and A. U. and M. T. and R. A process of glassy carbon etching without the micro masking effect for the fabrication of a mold with a high-quality surface. *J. Micromechanics Microengineering* **19,** 125010 (2009).